1-1-2013

Compressed Sensing And Joint Acquisition Techniques In Mri

Rouhollah Hamtaei
Wayne State University,

COMPRESSED SENSING AND JOINT ACQUISITION TECHNIQUES IN MRI

by

ROUHOLLAH (EHSAN) HAMTAEI

THESIS

Submitted to the Graduate School

Of Wayne State University,

Detroit, Michigan

In partial fulfillment of the requirements

For the degree of

MASTER OF SCIENCE

2013

MAJOR: BIOMEDICAL ENGINEERING

Approved by:

_____

Advisor Date

DEDICATION

I dedicate this work to my family.

ACKNOWLEDGMENTS

During my master's program and specifically while working on my thesis, I had the help and support of my family, friends and colleagues and I want to take this opportunity to thank them here. I would like to thank my parents for their constant support everyday in my life even from thousands of miles away. I am not sure if I could make it this far if it was not for their kindness, attention, care and support. I also want to thank my brothers for always being there for me and pushing me towards my goals so I wouldn't lose my faith.

I would like to thank my committee members, Dr. Yongqyan Ye and Dr. Zhifeng Kou for their help, support and advice they provided during my research. I'd like to especially thank Dr. Ye for being available anytime I had a question, patiently directing me towards an answer.

I would like to thank my advisor, Prof. E. Mark Haacke, firstly for giving me the chance to come abroad and study under his supervision. Dr. Haacke gave me the opportunity to work in his research group and learn not only about MRI but also about how to be a good researcher. His constant support and advice encouraged me every day to become better and work harder.

I also want to thank all the faculty, students and colleagues at Wayne State MR research facility and MR Innovations for their help and support during my study and research. I especially want to thank Rachel Matris-Laze and Lisa Brownshidle for their patience and help. I have to thank Charbel Habib and Jessy Mouannes-Srour for proof reading my thesis although they had really busy schedules.

Finally I would like to thank all my friends here and back home for their awesomeness and support. Thank you all!

TABLE OF CONTENTS

LIST OF FIGURES

CHAPTER 1: INTRODUCTION

Magnetic Resonance Imaging (MRI) is a non-invasive imaging modality. Compared with Computed Tomography (CT) and x-ray imaging, MRI does not utilize ionizing radiation. In addition there are multiple contrast mechanisms available through MRI. The MRI signal is sensitive to a variety of parameters including water content, oxygenation levels of the blood, blood flow, diffusion, temperature and concentration of metabolites, to name a few. Therefore MRI is a perfect medium for imaging soft tissue and specifically tissue in the human body.

The MRI technology has been improved rapidly both in hardware and software design and development since its invention more than 30 years ago. One of the most encountered challenges of MRI for being employed in clinical settings has been its relatively long scan time compared with CT imaging especially for high resolution three dimensional imaging. Most of the effort for improving the scan time in MRI has been with hardware improvements and developing faster imaging pulse sequences with efficient data acquisition strategies.

One approach for an effective acceleration scheme aims at collecting less data in favor of speed while retaining the quality of the images. This is possible because the MR signal is redundant in its nature so the underlying information may be extracted from fewer data measurements. One of the most successful efforts in this direction has been accomplished by parallel imaging techniques utilizing the spatial information provided by multiple receiver coils. Alternate approaches exist on the reconstruction side, and favor the use of central k-space to improve resolution and yet keep the acquisition time short [1-6].

Another relatively new concept is known as Compressed Sensing (CS) which exploits the compressibility of the MR images in order to reduce the number of measurements necessary for reconstructing an image. CS suggests that randomly collecting highly undersampled data points at the outer k-space can significantly ease the process of extrapolating the missing data in k-space. The nature of this theory is very well compatible with the physics of MR imaging.

In this thesis I explore the theory of compressed sensing and demonstrate its application and implementation in MR angiography. In addition I explore a new technique to perform MR dynamic imaging by employing a combination of keyhole imaging, view-sharing and CS sampling techniques which we refer to as *joint data acquisition and reconstruction*.

1.1 Thesis Outline

In Chapter 2, the basics of MR imaging and the physical theories will be reviewed and discussed. I introduce just the tools and concepts necessary for understanding the MR methods used including MR physics, signal generation, signal acquisition, spatial encoding, k-space coverage and image reconstruction.

In Chapter 3, I revisit the time constraints of MR imaging and introduce the parameters affecting the imaging speed. Then, I briefly introduce the general means to reduce the scan time.

In Chapter 4, I delve into the concept of compressed sensing and its application to MR angiography. I also discuss the limitations and the artifacts associated with the CS implementation.

In Chapter 5, I introduce the idea of joint acquisition and reconstruction, review the basics of keyhole imaging and view-sharing technique and show how they can be combined with the idea of CS random sampling. I show the application in multi-echo spin echo dynamic imaging with the purpose of rapid T2 parameter mapping.

Finally in Chapter 6, I provide a summary of this work along with some future directions.

CHAPTER 2: PRINCIPLES OF MAGNETIC RESONANCE IMAGING

2.1 History

The history of Nuclear Magnetic Resonance (NMR) started with the discovery of the nature of the proton. Stern and Gerlach back in the 1920s set the foundation for Rabi and coworkers to study the interaction of protons with a magnetic field. Later on in 1946, Bloch and Purcell were able to extend the previous concepts to a measurement of an effect of the precession of the spins around a magnetic field [7]. The behavior of an individual spin can be understood and described via quantum mechanics.. However, the macroscopic behavior of an isochromat (large number) of spins can be described with classical physics. A brief review of key concepts in MRI required in this thesis is provided below.

2.2 Polarization

Any *nuclei* with an odd number of protons and neutrons possess a property called *spin*. This is a quantum mechanical phenomenon which can simply be visualized by a rotational motion of the spin about its own axes. Since the proton of the atomic nuclei is charged, this rotational motion will create a *magnetic moment*.

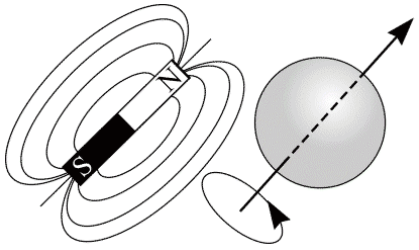

Figure 2.1, A single nuclei creates a magnetic moment (like a bar magnet) due to its rotational motion about its own axes.

In an environment with no strong magnetic field present, this magnetic moment is randomly oriented. However when protons are positioned in an external magnetic field, the spins will align in one of the two *parallel* or *anti-parallel* positions. The interaction of the dominant nucleus in MRI, the proton in hydrogen, with an external magnetic field, $\overrightarrow{B_0}$, results in the precession of the proton spin about the field direction (Figure 2.2). This precessional angular frequency which is also known as the *Larmor frequency* is given by:

$$\omega_0 = \gamma B_0 \qquad (2\text{-}1)$$

where γ is a constant called the gyromagnetic ratio. In water, the hydrogen proton has a γ value of approximately 2.68×10^8 rad/s/Tesla or 42.58 MHz/T.

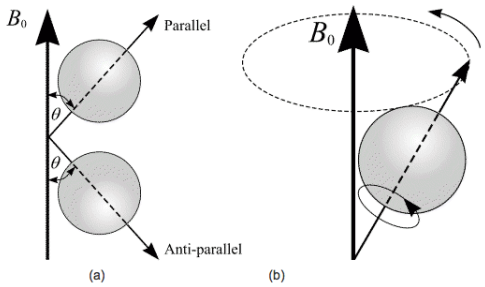

Figure 2.2, (a) The alignment of the spins in parallel or anti-parallel orientations when positioned in a strong magnetic field (B0). (b) The precession of the proton spins about the external magnetic field (B0). Image is taken from (http://www.mikepuddephat.com/Page/1603/Principles-of-magnetic-resonance-imaging)

2.3 rf excitation, resonance and relaxation

Now considering the spins aligned along the $\vec{B}_0$ in the z direction, if a *radiofrequency (rf)* magnetic field ($\vec{B}_1$) is applied, the spins will be tipped away from the external field direction. In order for the B1 field (also known as the transmit field) to tip the magnetization away, it must: 1- have components in the transverse plane, 2- its frequency must match the Larmor frequency

of the nuclei of interest. This frequency usually lies in the rf range in conventional high field MRI machines. The second condition is also known as being on *resonance*, where the B1 field is maximally synchronized to tip the spins away from the $\overrightarrow{B_0}$ direction.

The magnetization produced as a result of applying the rf pulse is often broken into two key components: the longitudinal component ($\vec{M}_z$) along the main magnetic field direction ($\overrightarrow{B_0}$) and the transverse component ($\vec{M}_\perp or\ \vec{M}_{xy}$).

The extent of tipping is determined by the length of time the rf pulse is on and the amplitude of the pulse. The angle through which the magnetization is rotated is referred to as the *Flip Angle* (FA). The rf field is stopped after the magnetization is tipped by the desired amount.

The behavior of the tipped magnetization will depend on the intrinsic energy exchange as a result of the interaction between the protons themselves as well as with surrounding micro environment. These effects are known as “spin-pin” and “spin-lattice” interactions respectively, which affect the magnetization evolution over time. They are also known as *relaxation effects*. The differential equation of magnetization is described by the *Bloch equation*:

$$\frac{d\vec{M}}{dt} = \gamma\vec{M} \times \vec{B}_{ext} + \frac{1}{T1}(M_0 - M_z)\hat{z} - \frac{1}{T2}\vec{M}_\perp \quad (2\text{-}2)$$

where M_0, M_z and $\vec{M}_\perp$ are the *equilibrium*, longitudinal and transverse components of the magnetization respectively and γ, T1 and T2 are constants which are specific to the type of tissue. T1 and T2 are also known as the intrinsic relaxation factors of the tissue or material of interest.

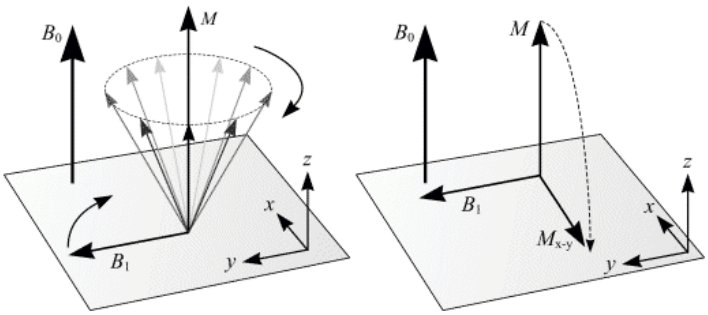

Figure 2.3, The effect of a synchronized rf B1 field on the bulk magnetization (M) which has been polarized in the external magnetic field B0. M is tipped away from its equilibrium orientation to the transverse plane (in this case a 90 degree flip angle). Image taken from http://www.mikepuddephat.com/Page/1603/Principles-of-magnetic-resonance-imaging)

2.4 Spatial encoding and gradients

The signal from the sample inside the MRI machine has to be spatially encoded in order to create an image. This can be done by applying what is known as *gradient fields* or *gradients.* Gradients are additional longitudinal magnetic fields which vary linearly along space and therefore change the resulting magnetic field of each point in space. By doing so each point in space ($\vec{r}$) will have a unique precessional frequency associated with it (equation (2-3)). This difference can be used in order to encode the spatial information in the MR signal.

$$B(\vec{r}) = B_0 + G\vec{r}$$
$$\omega(\vec{r}) = \gamma B_0 + \gamma G\vec{r} \qquad (2\text{-}3)$$

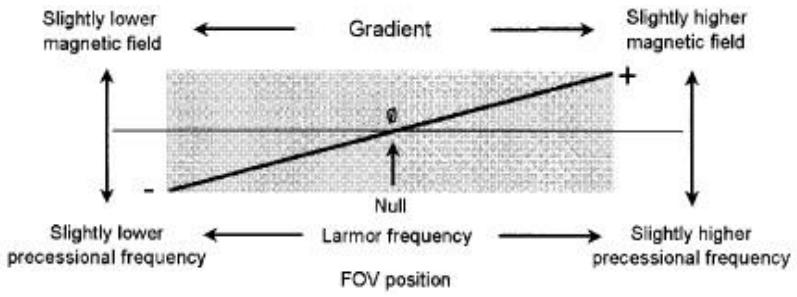

Figure 2.4, A schematic of a gradient field and how it varies along space. The resulting longitudinal magnetic field in each point in space will have a unique and slightly different strength.

The gradient fields are shown with G_x, G_y and G_z, which combined can encode a three dimensional space. The gradient along x direction is applied during the sampling process and is referred to as *frequency encoding gradient*. The gradients along other two directions are turned on repeatedly only for a specific interval and therefore their effect on the MR signal is represented as additional accumulated phase.

2.5 Signal detection

Once the magnetization has a transverse component, its precession about B_0 direction can be detected with a receiver coil. According to the Faraday induction law, an *electromagnetic force (emf)* will be induced in a coil by a change in magnetic flux environment. The signal must go through demodulation in order to remove rapid signal oscillations caused by the B_0 field. Assuming that there is no relaxation effects, the demodulated signal in the time-domain can be written as below [7]:

$$S(t) = \int d^3\,\vec{r}\rho(\vec{r})e^{-i\varphi(\vec{r},t)} \qquad (2\text{-}4)$$

Where $\rho(\vec{r})$ is the effective *spin density* at spatial coordinates $\vec{r}$ which can be introduced as:

$$\rho(\vec{r}) \equiv \omega_0 \Lambda \mathrm{B}_{\perp} M_0(\vec{r}) \quad (2\text{-}5)$$

where ω_0 is the Larmor frequency, $\mathrm{B}_{\perp}$ is the component of receive coil B_1 field that lies in the transverse plane, Λ is introduced as a constant which includes the gain factors from the electronic detection system and $M_0(\vec{r})$ is simply the initial transverse magnetization or equilibrium magnetization.

The accumulated phase term in equation (2-4) is a result of applied gradients for spatial encoding and can be written in radians:

$$\varphi(\vec{r}, t) = \gamma \int_0^t \vec{r} \cdot \vec{G}(t')dt' \quad (2\text{-}6)$$

The use of a gradient ($\vec{G}$) to establish a relation between the position of spins along some direction ($\vec{r}$) and their associated phase ($\boldsymbol{\varphi}(\vec{r}, t)$) is referred to as the spatial encoding (or frequency/ phase encoding).

Equation (2-6) shows the contribution of phase to the detected signal in an MRI experiment. Once the bulk magnetization is tipped to the transverse plane by applying an rf pulse, the T2 relaxation effect can be described as *dephasing* of the spins which leads to an exponential decay of the bulk transverse magnetization magnitude.

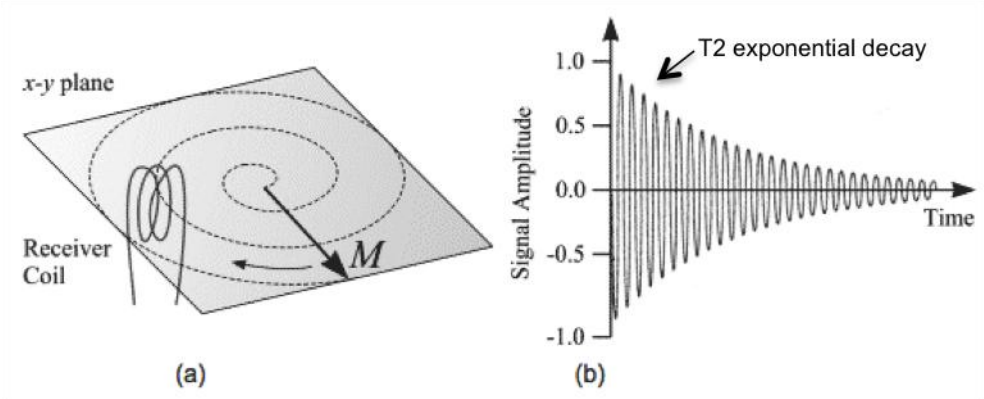

Figure 2.5, (a) the magnetization after a 90 degree rf excitation, precessing in the transverse plane (aka FID experiment). The receiver coil can measure the induced signal from the magnetization. (b) The signal vs time recorded by the receiver coil. The decay envelope of the signal is due to T2 (T2*) relaxation effect. Image taken from http://www.mikepuddephat.com/Page/1603/Principles-of-magnetic-resonance-imaging)

2.6 k-space

In the early days of the development of MRI, it was recognized that the time-domain signal could be manipulated by following trajectories, driven by the gradients, that evolve in a 2D or 3D space [8]. This simple but critical realization is the cornerstone of MR imaging which led to the paper by Nobel Prize winners Paul Lauterbur [9] and Peter Mansfield [10].

The role of the spatial encoding gradients is to map the MR time signal to a different space which is known as *k-space* and is defined as:

$$\vec{k}(t) = \frac{\gamma}{2\pi}\int_0^t \vec{G}(t')dt' \qquad (2\text{-}7)$$

k-space has units of inverse distance (usually 1/cm – a spatial frequency). With this definition the MR signal mentioned in equation (2-4) can be re-written as:

$$S(\vec{k}) = \int d^3\, r\rho(\vec{r})e^{-i2\pi\vec{k}.\vec{r}} \qquad (2\text{-}8)$$

Using the inverse Fourier transform property we can show that the effective spin density can be calculated as:

$$\rho(\vec{r}) = \int dk\, s(\vec{k}) e^{+i2\pi \vec{k}.\vec{r}} \quad (2\text{-}9)$$

This general formulation can be applied towards 1D, 2D or 3D imaging as conforms, noting that the time-domain and k-space share the same dimensionality. For example a 2D experiment would be possible in the presence of a set of two orthogonal gradients and the signal may be written as a 2D Fourier transform called *2D imaging equation* [7]:

$$S(k_x, k_y) = \iint dxdy\ \rho(x,y) e^{-i2\pi(k_x x + k_y y)} \quad (2\text{-}10)$$

The two implicitly time-dependent components of $\vec{k}(t)$ are related to the respective integrals over the gradient components and are known as *frequency encoding* and *phase encoding directions* respectively:

$$k_x(t) = \frac{\gamma}{2\pi}\int_0^t \overrightarrow{G_x}(t')dt', \qquad k_y(t) = \frac{\gamma}{2\pi}\int_0^t \overrightarrow{G_y}(t')dt' \quad (2\text{-}11)$$

The k-space is usually shown as a matrix with the same dimensions of the image. The frequency encoding direction is shown with straight lines which indicate its continuous sampling process. Points are often shown on each line and represent individual samples of the MR signal. Figure 2.6 shows a common schematic of a two dimensional k-space.

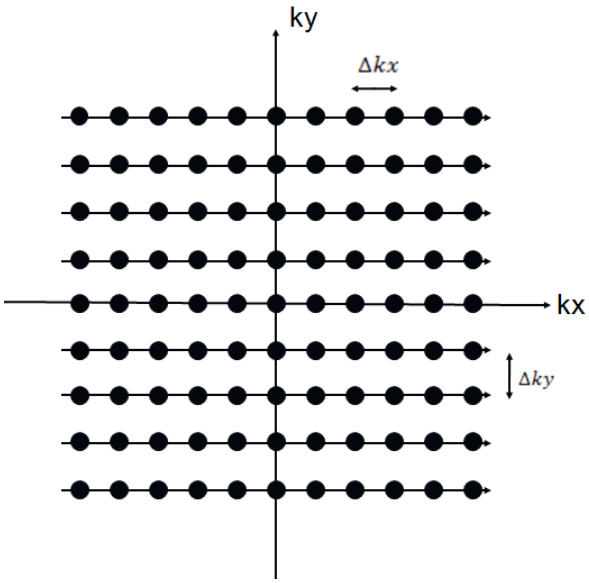

Figure 2.6, A schematic of a two dimensional k-space. Kx is the frequency encoding direction, ky is the phase encoding direction. Δkx and Δky are the sampling intervals or encoding steps.

The *center of k-space* holds the low spatial frequency information and as we get further from the center of k-space it will become higher spatial frequency information. This simply means that most of the image contrast information is stored at the center of k-space while the *outer k-space* adds the detail information of the image. The center of k-space is of utmost importance in MR imaging and reconstruction.

The k-space concept can be extended for 3D imaging with via employing the additional gradient in the z direction also known as *partition encoding* gradient G_z. This gradient will control sampling through the third direction in k-space and encodes the spatial information through the third dimension. Now we have a set of 2D k-spaces which combined will create the entire 3D dataset. The 2D planes in k-space are separated from each other by a fixed distance (Δkz).

2.7 Sampling

The k-space *trajectory* is the path traced out by $\vec{k}(t)$ which is driven by alternately turning on the gradients in different directions. Although k-space trajectories may traverse a continuous path in k-space, the signal may only be sampled in a discrete fashion. *Sampling* is the process of converting a continuous signal into a countable sequence of the same quality.

The MR signal is sampled with measurements at finite time steps Δt during the continuous application of the *read encoding* gradient G_x. The associated intervals in k_x (or readout) direction can be written as:

$$\Delta k_x = \frac{\gamma}{2\pi} G_x \Delta t \qquad (2\text{-}12)$$

where G_x is the frequency-encoding gradient and Δt is the sampling time interval. The sampling intervals in the other k-space directions known as *phase encoding* and *partition encoding steps* ($\Delta k_y \; and \; \Delta k_z$), can also be defined in the same fashion:

$$\Delta k_y = \frac{\gamma}{2\pi} \Delta G_y \tau_y \qquad \Delta k_z = \frac{\gamma}{2\pi} \Delta G_z \tau_z \qquad (2\text{-}13)$$

where τ_y and τ_z are the duration of application of the gradients.

For proper image reconstruction from k-space, some sampling requirements must be met. In other words, we need to collect sufficient number of signal samples to cover the k-space. This requirement is describes in the *Nyquist-Shannon sampling theorem*.

2.7.1 Nyquist-Shannon sampling theorem

Nyquist-Shannon sampling theorem (more commonly referred to as Nyquist theorem), describes a fundamental principle in the field of signal processing and information theory. This theorem states that any band-limited signal can be reconstructed perfectly from a finite number

of samples taken uniformly at an interval not exceeding the reciprocal of twice the signal bandwidth. More specifically assuming that the signal $\mathrm{g(t)}$ is band-limited to $\mathrm{f_{max}}$, the Nyquist sampling theorem requires that:

$$\Delta \mathrm{t} \leq \frac{1}{2\mathrm{f_{max}}} \qquad \text{or} \qquad \mathrm{f_s} = \frac{1}{\Delta \mathrm{t}} \geq 2\mathrm{f_{max}} \qquad (2\text{-}14)$$

In other words, the largest sampling interval permissible for perfectly reconstructing the signal is $\Delta \mathrm{t} \leq \frac{1}{2\mathrm{f_{max}}}$, also known as the *Nyquist interval*. Correspondingly, the *Nyquist frequency* is $\mathrm{f_s} = 2\mathrm{f_{max}}$ which is the minimum sampling rate required for exact recovery of the signal [11].

If $g(n\Delta t)$ are the sampled values taken from the signal $g(t)$ with intervals of Δt satisfying the Nyquist criterion, then the signal $g(t)$ can be reconstructed using the following interpolation formula:

$$g(t) = \sum_{-\infty}^{\infty} g(n\Delta t) sinc[\pi f_s(t - n\Delta t)] \qquad (2\text{-}15)$$

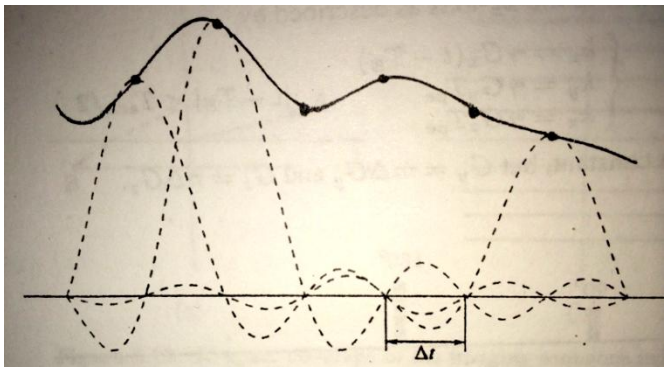

Figure 2.7, Illustration showing recovery of a continuous signal from its samples by a summation of weighted sinc functions. Image taken from [11].

2.7.2 k-space sampling requirements

Satisfying the sampling requirements of k-space can be seen as solving a multidimensional problem. In practice, however, k-space sampling is usually resolved in each

direction individually in order to reduce the problem dimensionality to a 1-D sampling problem. Once the sampling criterion is met, it guarantees perfect recovery of the underlying continuous k-space signal. Here we discuss the adoption of this conventional treatment to determine the sampling requirement of the popular 2D rectilinear (*Cartesian*) imaging scheme. The same treatment can be extended to higher dimensions.

Assume that the object being imaged is bounded in two directions with W_x and W_y as shown in Figure 2.8. According to the Nyquist sampling theorem the sampling intervals (or encoding steps) in each direction should follow:

$$\Delta k_x \leq \frac{1}{W_x} \qquad and \qquad \Delta k_y \leq \frac{1}{W_y} \tag{2-16}$$

Substituting equation (2-12) and (2-13) into equation (2-16), we can derive the final requirements for MR k-space sampling based on the imaging experiment:

$$\Delta t \leq \frac{2\pi}{\gamma |G_x| W_x} \qquad and \qquad \Delta G_y \leq \frac{2\pi}{\gamma \tau_y W_y} \tag{2-17}$$

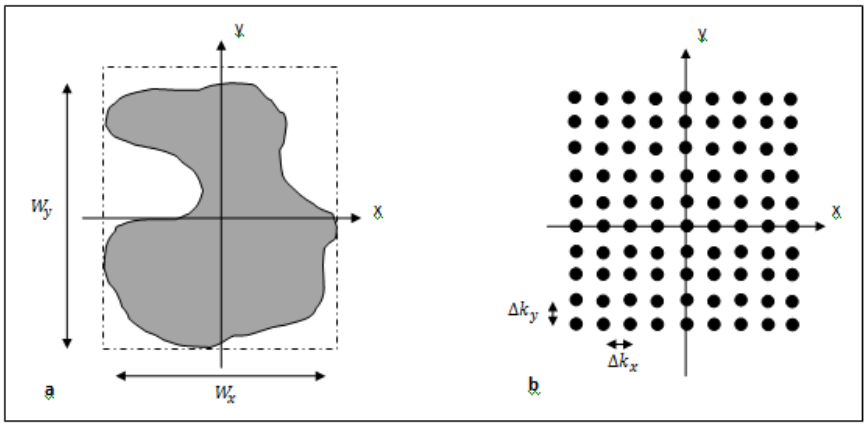

Figure 2.8, Rectilinear (or Cartesian) imaging scheme. (a) Object bounded by rectangle of widths $\boldsymbol{W_x}$ and $\boldsymbol{W_y}$. (b) Corresponding k-space samples. Reproduced from [11].

2.7.3 Field of View (FOV)

Field of view (FOV) is defined as the spatial encoding area of the image which can be multidimensional. Since the object being imaged has a limited size, the inverse Fourier transform of a finitely sampled signal from that object yields an infinite set of exact copies of its physical spin density (which is our image), separated from each other by FOV. One can show using the Fourier series properties [7] that the uniform spacing between data points in k-space (Δk), is equal to $1/FOV$.

$$\frac{1}{\Delta k} = FOV \qquad (2\text{-}18)$$

If the FOV is designed to be smaller than the object size, multiple copies of the resulting imaging experiment will be folded over each other. This phenomenon is known as *aliasing*.

2.8 Aliasing

According to the Nyquist sampling theorem, the continuous k-space signal can be recovered perfectly from its finite samples if the sampling criterion is met. If these conditions are violated, perfect reconstruction will not be possible .The resulting errors in the reconstructed image are known as *aliasing* artifacts. The extent and the shape of aliasing are dependent on how the samples are taken from the continuous signal and how much the conditions are violated.

We know that the spatial information of the image is encoded in the MRI signal via frequency and phase encoding by varying the processional frequency of spins along the object using gradients. On the other hand, the Nyquist criterion requires the sampling frequency to be greater than twice the signal bandwidth ($|f_{max}| < f_s/2$). If this condition is violated, any signal

with a frequency component outside this bandwidth will fold over. This artifact is well known as *aliasing*.

Usually when aliasing happens, it's not possible to remove it from the reconstructed images. However there are methods for avoiding the aliasing artifact using an essential feature of MRI receiver coils by applying a band-limiting hardware filter (*anti-alias filter*) on the signal prior to sampling. However this method cannot prevent aliasing in phase encoding directions and is only applicable to the frequency encoding direction. Different practical anti-aliasing methods in other encoding directions are discussed in [12].

We can redefine the Nyquist sampling criterion for MR signal acquisition as follows: the MR signal must be sampled densely enough that the inverse of the sampling step in k-space (Δk), is larger than the object size (W). In other words, if the FOV in any direction is chosen to be smaller than the object size, the information from any point in the object outside the FOV will wrap back into the reconstructed image.

$$L > W \qquad or \qquad \Delta k < \frac{1}{L} \tag{2-19}$$

An illustrative example of this phenomenon can be seen in Figure 2.9:

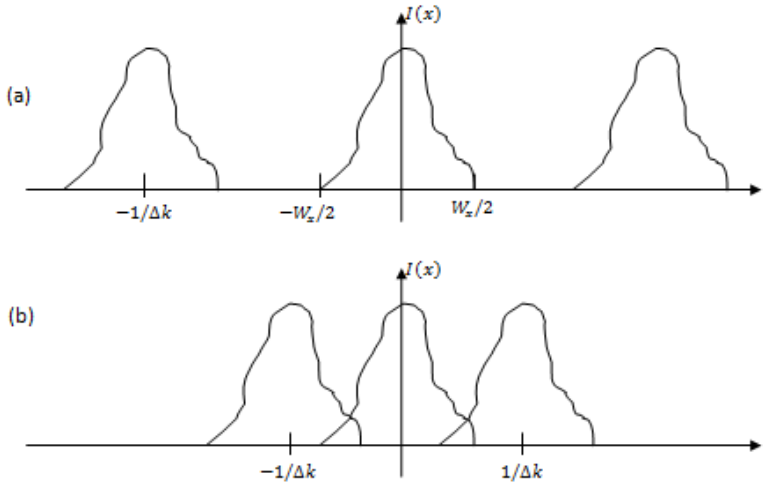

Figure 2.9, Illustration showing the k-space undersampling effect in the reconstructed object, known as aliasing. Nyquist criterion is met in (a) and violated in (b). Reproduced from [11].

2.9 Spatial resolution and Gibbs ringing

By definition, the *spatial resolution* of any imaging system is the smallest separation δx of two point sources necessary for them to remain resolvable in the resultant image [11]. The spatial uniform steps in the image-domain, called *pixels* or *voxels*, determine the visual quality of the image. Mathematically the relationship between the object and the resulting image in a perfect imaging system can be described as follows:

$$I(\vec{r}) = O(\vec{r}) * h(\vec{r}) \qquad (2\text{-}20)$$

where $O(\vec{r})$ represents the object at location $\vec{r}$, $I(\vec{r})$ is the image corresponding to the object at location $\vec{r}$, $*$ represents the convolution operator and $h(\vec{r})$ is the point *spread function (PSF)*. The image from equation (2-20), can be an exact representation of the object only if the PSF is a δ funtion. The more the PSF deviates from the δ function, the image will be *blurred*.

Here we show how the PSF of Fourier reconstructions, which is the case in MR imaging, can be calculated. Since the collected k-space signal is discretized, applying a discrete inverse Fourier transform in order to create the image will also map out to a discrete set of reconstructed spin densities. The number of k-space samples however is always finitely defined. On the other hand it is not possible to infinitely collect the MR signal in k-space. This is equivalent to *truncating* the true k-space which can also be described as filtering the signal ($S(k)$) by a *rect* function. The filter is given by:

$$H_w(k) \equiv rect(\frac{k+\frac{1}{2}\Delta k}{W}) \quad (2\text{-}21)$$

$$s_w(k) = s(k)H_w(k) \quad (2\text{-}23)$$

where W is given by:

$$W = N\Delta k \quad (2\text{-}25)$$

where N is the number of encodings (or samples).

According to the Fourier transform properties, the filtering process in k-space is equivalent to convolution in the image domain:

$$\hat{\rho}(\vec{r}) = \mathcal{F}^{-1}[s(k)H_w(k)]$$
$$= \rho(x) * h_w(x) \quad (2\text{-}26)$$

where $h_w(x)$ is defined as the PSF of Fourier reconstruction which is the inverse Fourier transform of $H_w(k)$:

$$h_w(x) = Wsinc(\pi Wx)e^{i\pi p\Delta k\vec{r}} \quad (2\text{-}27)$$

The effect of the phase term is often ignored because its effect is insignificant compared with that of the amplitude term. The effective width of the PSF function or the width of the rect function ($W = N\Delta k$) determines the extent of blurring in the resulting image. This blurring will lead to what we know as a *lower* resolution. The key point here is that the extent of k-space coverage in k-space ($N\Delta k$) has a direct relationship with the image spatial resolution.

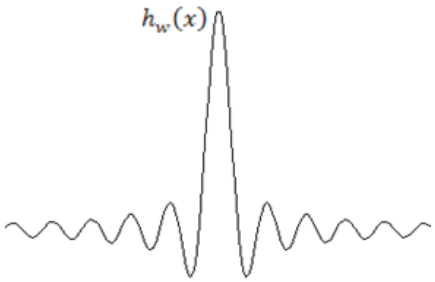

Figure 2.10, A plot of the amplitude term of the Fourier reconstruction PSF.

A lower spatial resolution will cause an artifact known as *partial volume effect* which refers to the interference of the signal from two points in the object if their physical distance is smaller than the spatial resolution of the image. In this case the intensity of a single voxel in the image may represent a combination of the resulting signals from multiple points in the physical object.

- Gibbs ringing

By definition, *Gibbs ringing* accompanies finite Fourier series representation of functions with step discontinuities. Gibbs ringing arises as an oscillating overshoot and undershoot in the immediate neighborhood of any step discontinuity in the image. This is a result of convolving the sideway lobes of the Fourier PSF with the object. The overshot and undershoot does not disappear by increasing the truncation window (or increasing the number of Fourier samples).

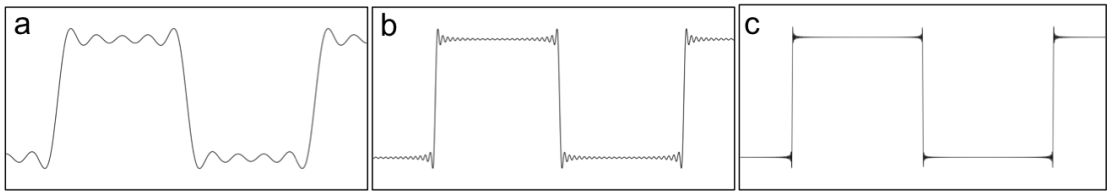

Figure 2.11, The effect of increasing the number of harmonics in approximating a square wave function. (a) 5 harmonics, (b) 25 harmonics and (c) 125 harmonics. It can be seen that the peak-to-peak difference of the overshoot and undershoot does not change. But they move closer to the discontinuity by increasing the number of harmonics. Image taken from Wikipedia.

It can be shown mathematically [7] that for example by doubling the truncation window ($N \rightarrow 2N$), the peak-to-peak difference in the ringing is invariant. However the peaks of the overshoot and undershoot move half the distance closer to the discontinuity than before. This property leads to less apparent Gibbs ringing artifact in high-resolution MR images.

Improving the resolution by increasing the size of the truncation window will reduce the appearance of Gibbs ringing artifact. The Gibbs ringing artifacts should be avoided especially if they mimic certain disease states.

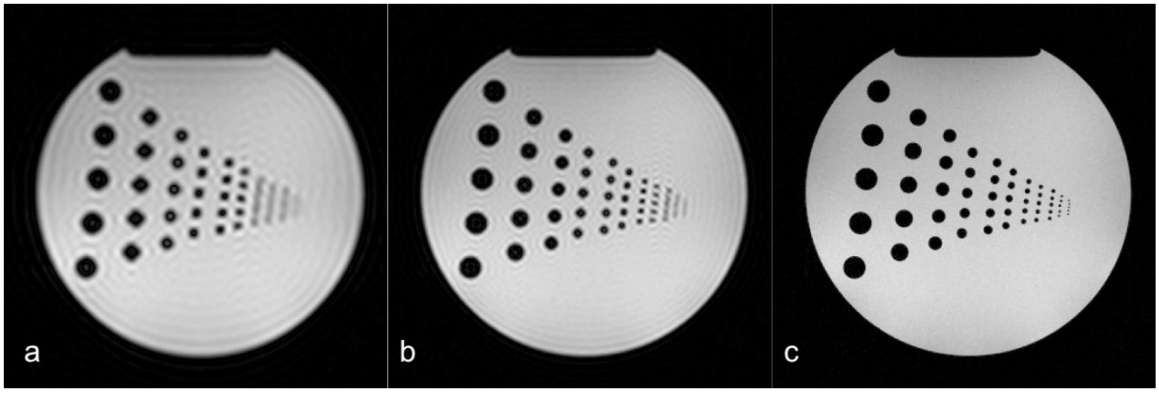

Figure 2.12, The phantom images from filtering a 320x320 matrix size acquisition with a fixed FOV. The reconstruction is from reducing the full window to (a) 64x64 window, (b) 100x100 window and (c) full window. The improved resolution, reduced blurring and reduced Gibbs ringing can be seen by increasing the window size.

CHAPTER 3: TIME SAVING STRATEGIES

The total scan time (T_T) for a given sequence is driven by a number of parameters. In order to reduce the scan time we need to discuss each of these parameters to see what leads to a short or long scan time. The repetition time (T_R), the number of phase encoding steps (N_y), the number of partition encoding (or slice encoding) steps (N_z) and the number of acquisitions for the sake of averaging (N_{acq}), all contribute to the total scan time (T_T) in a conventional MR imaging experiment giving:

$$T_T = \mathrm{N_{acq} N_z N_y T_R} \quad (3\text{-}1)$$

Making T_R shorter will directly reduce the total scan time. The contrast in the image is affected by tissue parameters such as relaxation effects and imaging parameters such as T_R. Of course as $T_R$changes, the image contrast will change as well, and if the change is for the worse, shortening $T_R$for reducing the scan time may not be useful. One should note shortening TR will reduce the overall image signal-to-noise ratio (SNR) as well.

In order to increase the SNR, it is common to acquire the image more than once and average them. However if one can maintain sufficient SNR, another method to reduce the scan time is to reduce the number of acquisitions and ideally keep the $\mathrm{N_{acq}}$ only one. The reduced SNR can be compensated for using better rf coil designs or a set of multiple rf coils (e.g. phased array coils).

3.1 Unsampling and Undersampling

The idea of this approach is to decrease the number of phase encoding and/ or partition encodings (N_y and N_z). The advantage of this approach is that the image contrast remains

unchanged. This can be done in two different ways described below. Figure 3.1 summarizes the time saving strategies via reducing the number of phase and partition encodings.

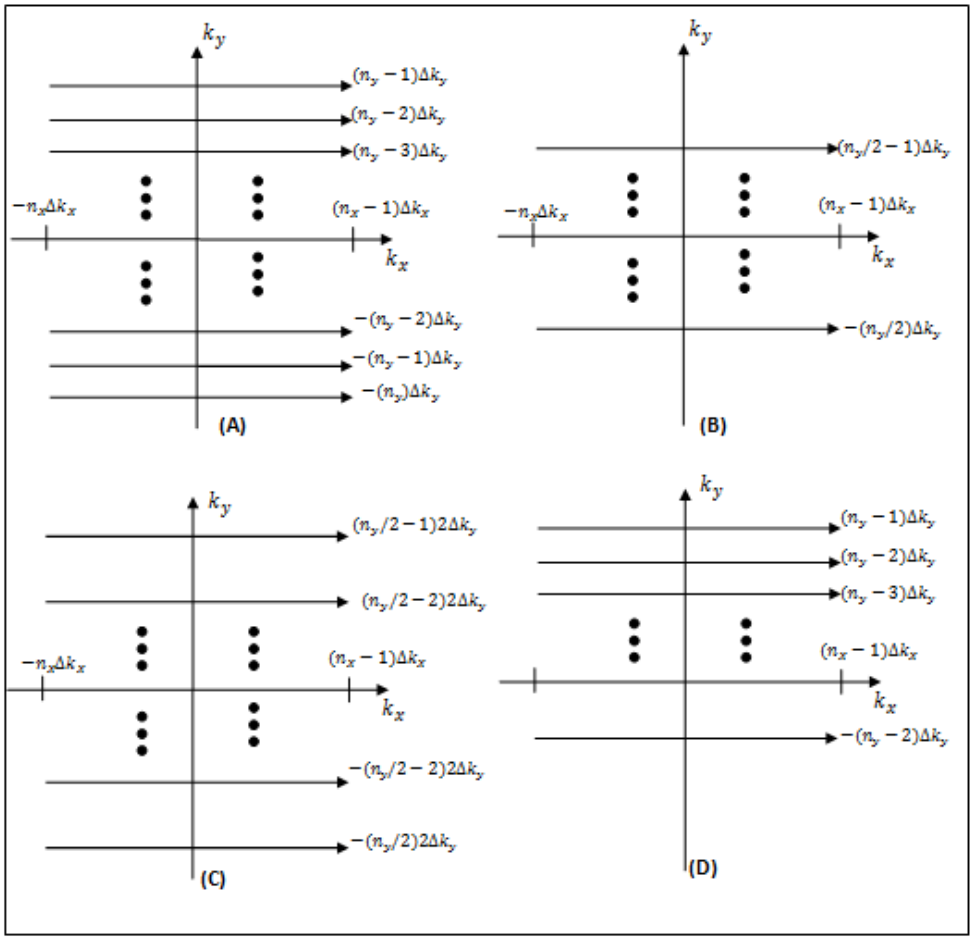

Figure 3.1, Time saving strategies shown in schematics of k-space sampling scheme. (A) shows a fully sampled k-space with all the phase encoding lines collected. (B) shows a truncated k-space with only half of the phase encoding lines collected. This will lead to an image with lower spatial resolution and possible blurring and Gibbs ringing in the phase encoding direction. (C) shows an undersampled k-space with only every other phase encoding line collected. This effectively increases the phase encoding step (Δky) which might lead to aliasing artifacts. (D) shows a k-space which is only partially collected. This acquisition is known as partial Fourier imaging.

3.1.1 Reducing the number of k-space encodings with a fixed FOV

A fixed FOV is equivalent to keeping the encoding steps (Δk) unchanged. With this assumption, for $N_y \rightarrow \lambda N_y$ (or $N_z \rightarrow \lambda N_z$) with $\lambda < 1$, the acquisition time will be shortened by a factor of λ. This is equivalent to even more truncation of the k-space signal (Figure 3-1.B).

However, we know that the spatial resolution will also get worse by a factor of λ (i.e. $\Delta y \rightarrow \Delta y/\lambda$) because:

$$\Delta y = \frac{FOV_y}{Ny} \quad (3\text{-}2)$$

This degraded spatial resolution will lead to blurring, partial volume effects and Gibbs ringing artifacts. Moreover, this approach will increase the SNR by a factor of $\frac{1}{\sqrt{\lambda}}$. Throughout this thesis we may refer to this method as the low-resolution method.

3.1.1.1 Constrained Reconstruction

In order to compensate for the loss of high spatial frequency information in centrally acquired k-space, there have been a number of data extrapolation methods proposed often referred to as *constrained reconstruction [6]*. Constrained methods are reconstruction algorithms developed in order to recover high spatial frequency information.

The general idea of constrained reconstruction methods is to employ *a priori* information in order to compensate for the lack of high spatial frequency information in k-space. Conventional MR image reconstruction assumes zero for the missing high spatial frequency information in truncated k-space. The word "constrain" means to put *a priori* information such as bounds or a parametric model upon the reconstruction. In principle any *a priori* information about the object being imaged can be used as a constraint to improve the accuracy of the image. Although, it should be noted that these constraints should be employed carefully in order to prevent biasing the resulting images.

Depending on the kind of constraints being used they can be generally divided into three categories: *phase-constrained* methods, *nonparametric* methods and *parametric* methods.

Discussing the details of each of these methods is beyond the scope of this thesis and can be reviewed in reference [6]. However here we briefly mention the concepts.

The phase-constrained methods force the final reconstruction to have a certain predetermined phase. These partial Fourier methods are suitable for cases where the k-space is only partially sampled [13], [14].

Nonparametric methods permit the use of conventional Fourier series for reconstruction and generally provide models for *extrapolating* the unsampled high spatial frequency information in k-space. How accurately the missing data in k-space is recovered is dependent on the designed constraint. Some of the famous constraints are known as *finite spatial support*, *maximum entropy*, *linear predictability* and image smoothness [6]. The nonparametric methods have the advantage of being relatively straightforward and computationally efficient.

Parametric models on the other hand represent the image function in terms of a set of parameterized basis functions. In other words, parametric methods, provide a model for the image itself and try to accommodate that model to the existing artifacted image. In this sense parametric models can ideally create images of infinite resolution without the need of extrapolating the missing k-space information. This feature is well known as the concept of *super-resolution* reconstruction [1, 5]. Although the idea of parametric models has been used widely in different areas of signal processing, its application to imaging has been limited due to the complexity of the basis function and inversion process.

Generally in parametric methods, an optimal model should be chosen and designed for the particular imaging application. These models should satisfy a set of requirements in order to

ensure robustness, accuracy and computational efficiency. As an example, one of the models proposed by Haacke and Liang [1], treats the image as a series of rectangular cross sections. This model can resolve sharp edges of the image fairly accurately; however higher order features may not be successfully resolved.

The principals of parametric method reconstructions include three steps: 1- Choosing an appropriate model, 2- Fitting the model to the available data and 3- Creating the image directly from the fitted model itself or from the extrapolated data like in nonparametric methods. *Autoregressive moving average (ARMA)* [15, 16], *localized polynomial approximation (LPA)* (as a complement to ARMA) [1, 17] and *generalized series (GS)* [18] are among the successful parametric methods.

3.1.2 Reducing the number of k-space encodings with a fixed resolution

If reduced spatial resolution and its associated artifacts cannot be tolerated due to the clinical value of the image, the previous method for saving time may not be useful. Another method which can maintain the spatial resolution and still reduce the scan time would be to reduce the number of encoding lines without changing the k_{max}. In this method, we would effectively increase the sampling intervals (Δk) or encoding steps. Throughout this thesis we refer to this method as *undersampling* of k-space. However we know that increasing the sampling intervals (i.e. Δk to $\Delta k/\lambda$) will lead to cutting down the FOV to λFOV in the same direction. Therefore, unless the object size is larger than the new FOV (λFOV), lowering the sampling rate will lead to aliasing. Potentially, this approach can reduce the scan time by a factor of λ just like the previous method. In addition, this approach will decrease the SNR to $\sqrt{\lambda}SNR$.

3.1.2.1 Parallel Imaging

Just like in the case of unsampling and constrained reconstruction, there have been methods proposed for interpolating the missing k-space signal in undersampled situations. One of the very successful and commonly used methods is known as *parallel imaging*. Parallel imaging can be considered as a subcategory of the constrained reconstruction methods. Here in order to compensate for the missing k-space signal and overcome the resulting aliasing artifacts, an array of independent receiver coils are used instead of a single homogenous receiver coil. The spatial sensitivity map of the employed receiver coils then are used as *a priori* information in order to combine the undersampled signal from each receiver coil into an un-aliased image within the desired FOV. It is important to note that parallel imaging is not an imaging sequence method, but only a reconstruction method.

The number of receiver coils determines the extent of undersampling permissible for successfully recovering the aliased image. Many different parallel imaging methods have been introduced through the past years. Discussing the details of each method is not at the scope of this thesis [19], [20], [21].

There are other methods which can be used for recovering the missing k-space signal in undersampled situations. Another relatively new method is known as *Compressed Sensing (CS)* which is the subject of Chapter 4.

3.1.3 Partial Fourier

Another strategy to reduce the scan time exploits the *complex conjugate* property of the Fourier transform of real objects to reduce the number of phase encoding steps (N_y) required to reconstruct the image. This property can be well described with:

$$if\ \mathcal{F}[\rho(r)] = \mathrm{S}(k), \quad then\ \ \mathcal{F}[\rho^*(r)] = \mathrm{S}^*(-k) \qquad (3\text{-}3)$$

In some applications, in order to reduce the scan time, k-space is covered asymmetrically in the phase encoding direction. Usually the negative half of k-space is left empty and the positive half is filled. The time-saving factor is determined by the degree of asymmetry. The negative half of k-space can be either left empty (zero filled), or can be filled according to the conjugate symmetry of k-space. Ideally, the reconstructed image should be identical to the one where full k-space information was acquired.

However, in practice, the object motion and magnetic field inhomogeneities often violate the realness constraint and introduce a non-zero phase term to the image function. Consequently image artifacts would appear if this phase is not treated properly. In order to overcome this problem, usually a few additional encoding lines are collected across the center of k-space (Figure 3.1-D).

Most existing partial Fourier methods use this approach along with a two-step reconstruction procedure. The first estimates a phase function by reconstructing a low-resolution image based on the central k-space information. And the second combines the calculated phase with the measured data to get the final reconstructed image.

CHAPTER 4: COMPRESSED SENSING (CS)

With the tremendous interest in high-speed imaging, researchers continue to develop new image acquisition and reconstruction techniques. Most methods that attempt to reduce the scan time either acquire data faster or limit the number of phase or partition encodings. The former suffers from a loss of SNR, while the latter suffers from a loss of spatial resolution and image artifacts (most noticeably Gibbs ringing and aliasing) as well. There has been extensive research in developing methods to overcome these problems. In most methods, *a priori* information is utilized to compensate for the lack of sufficient measured data. This group of methods is also known as constrained reconstruction. The goal in any constrained reconstruction is to achieve the best way to incorporate the *a priori* information into the reconstruction process. Improper use of the *a priori* information may lead to reconstructions with biased or artifacted results. A comprehensive review of all the methods in this area is not at the scope of this thesis.

"*Compressed Sensing*" or "*Compressive Sampling*" or "*CS*" is a relatively new approach which shows, contrary to the Nyquist sampling theorem that good quality images can be recovered from far fewer measurements that is usually considered necessary [22]. In this chapter we introduce the theory of CS and how it can be applied to MR imaging.

4.1 Introduction

Sparsity and *compressibility* as two important ingredients of CS, have played a fundamental role in many fields of science and more specifically in information technology [23, 24]. As a general rule of thumb, sparsity leads to more efficient compression algorithms in both signal and

image processing techniques. In addition, sparsity leads to dimensionality reduction and efficient modeling [22, 25].

One of the novelties of CS can be extracted from the statement: "*sparsity has bearings on the data acquisition process itself, and leads to efficient data acquisition protocols" [22].* In other words, CS suggests acquiring the analog signal as economically as possible taking advantage of its sparse nature [22, 25]. From an MR perspective this means that we can modify the data acquisition scheme in order to reduce the imaging time. This notion is based on the fact that any image (including medical images) with some structure can be efficiently compressed without much perceptual loss. "*JPEG*" compression format is a very common and modern example in the field of image processing which exploits the fact that many images have a sparse form of representation in a fixed basis (in this case a wavelet basis), meaning only a small number of these coefficients are necessary for reconstructing the signal. However in the case of JPEG, usually the image is fully acquired in the first place and then compressed by removing all the insignificant coefficients of its sparse representation. This process of massive data acquisition followed by compression can be looked at as a waste of sampling (sensing) resources (i.e., camera sensors). CS on the other hand, suggests acquiring the signal in an already compressed format so that there will be no need to throw away any excessive data.

Therefore we are interested in *undersampled* situations rather than fully sampled, which implies that the number of measurements may be much smaller than the dimensionality of the signal. For any compressed sensing algorithm to work properly, two components must be considered carefully: *recoverability* and *stability*. The former ensures that the chosen acquisition

scheme or measurement matrices along with the recovery algorithm guarantees recovery of the missing measurements. It also addresses the sufficient number of measurements necessary for exact recovery of the image. The latter, stability, ensures the robustness of the algorithm in case of noisy or corrupted measurements.

4.2 Intuitive 1D example

In order to understand the concept of CS and its relationship with undersampling, here we discuss a concrete example with a one-dimensional signal of interest (x) [26]. In this example, x is simply a 1x128 vector with only five non-zero coefficients, which makes it an extremely sparse signal (Figure 4.1). This signal is the equivalent of the actual MR image in the case of CS MRI with one important difference that the MR image might not be sparse in its original domain.

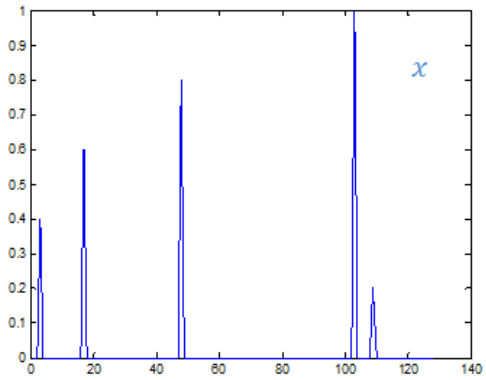

Figure 4.1, A plot of the one dimensional sparse signal x.

To make a similar situation with MR imaging, we consider the problem of reconstructing the vector x, from a subset of its frequency (Fourier) measurements (equivalent to k-space in

MRI). Sensing an object by measuring selected frequency coefficients is the principle underlying MRI. Accordingly, here we compute the centered Fourier transform (FFT) of the vector x.

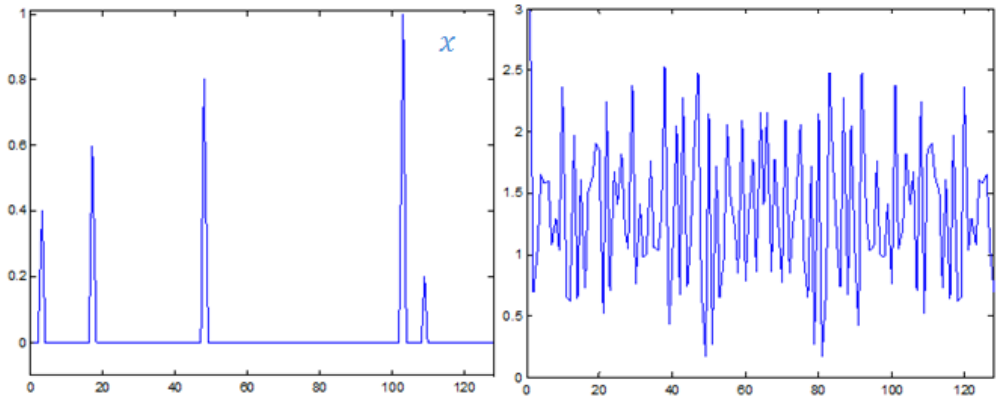

Figure 4.2, The sparse signal x and its corresponding Fourier transform (K). Only the absolute value of the Fourier transform is shown here.

To investigate the effects of undersampling on the reconstructed signal, we keep only a subset of Fourier coefficients and put the rest to zero. This procedure is also known as *zero-filling*.

$$K_u = \mathcal{F}_u(x) \qquad (4\text{-}1)$$

where $\mathcal{F}_u$ is the Fourier operator which is only evaluated at a subset of frequency domain samples. Here we demonstrate the effects of undersampling considering two cases: *equispaced (uniform)* undersampling and *random* undersampling.

4.2.1 Equispaced (uniform) undersampling:

As an example, from the total of 128 frequency samples, we choose only 32 equispaced (uniform) samples and put every other sample to zero (zero-filling). This implies an undersampling degree of four meaning we only have a quarter (1/4) of the total number of measurements as before. The undersampled zero-filled Fourier signal can be reconstructed

using an inverse Fourier transform. In order to compensate for the energy loss of the reconstructed signal due to less measurements, we simply multiply the magnitude of all the available samples by a factor of four [1].

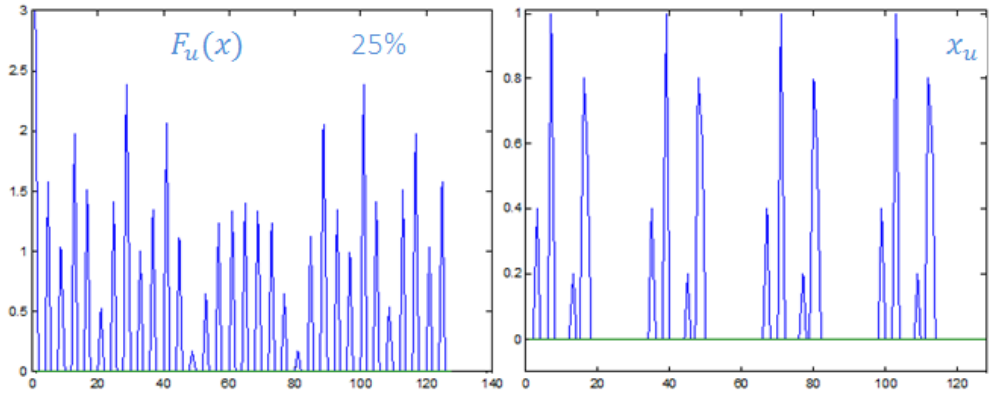

Figure 4.3, 25% undersampled Fourier samples of signal x. The reconstructed signal (x_u) with coherent aliasing artifact apparent.

As can be seen in Figure 4.3, the reconstructed signal (x_u), suffers from *coherent aliasing*. Now we have multiple copies of the sparse vector (x) and there is essentially no way to distinguish between them. This indicates that in the case of equispaced (uniform) undersampling, we cannot recover the original signal x from x_u due to the coherent aliasing artifacts. As the degree of undersampling increases the aliasing artifacts become even more severe.

[1] This strategy for energy loss compensation may not be suitable for all cases. For example different object sizes may require a different compensation strategy. However, with no *a priori* information from the object this is a fairly good approximation.

4.2.2 Random Undersampling

One of the unique aspects of CS theory is to use a *random undersampling* scheme instead of equispaced (uniform) undersampling. In this case the randomly undersampled Fourier signal can be shown as:

$$K_r = \mathcal{F}_r(x) \qquad (4\text{-}2)$$

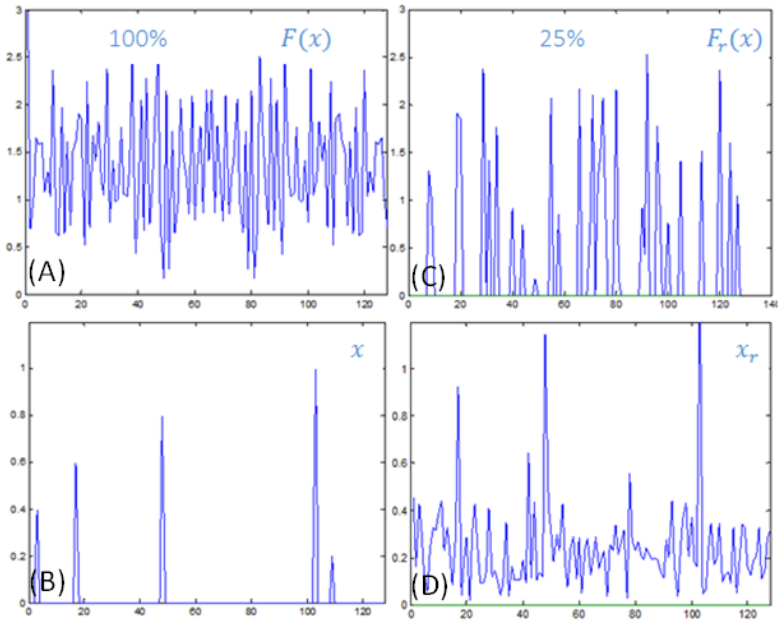

Figure 4.4, (A) the fully sampled Fourier series of (B) the sparse signal x. (C) 25% randomly undersampled Fourier series (K_r). (D) the reconstructed signal (x_r) from the randomly undersampled Fourier series shows incoherent aliasing artifacts which appear like noise.

Figure 4.4 shows random undersampling of the Fourier signal leads to *incoherent aliasing*. Incoherent aliasing interference with a sparse signal appears like systematic noise but we know that it is not caused by additive white noise which occurs in real systems.

The uniqueness of CS reconstruction is, coefficients of the sparse signal with high enough amplitude can still be recognized above the level of this noise-like artifact. Once the large coefficients of the signal are appropriately estimated, the missing Fourier samples coming from

these objects can be estimated and filled in. Repeating this process can dramatically reduce the noise-like artifacts. Therefore de-noising of the randomly undersampled signal is one of the key steps in the CS algorithms.

4.2.3 Denoising

There are different *minimization/regularization* approaches for de-noising signals, each suitable for different applications. One of the most common methods for ill-posed problems is known as the Tychonov penalty approach (also known as Tychonov regularization). Regularization, in math and probability in many fields dealing with inverse problems, refers to the process of introducing additional information in order to solve an ill-posed problem [27]. For instance, let's assume the following problem where A and b are known but the problem is not well-posed either due to non-existence or non-uniqueness of x:

$$\mathrm{Ax} = \mathrm{b} \qquad (4\text{-}3)$$

The standard approach is known as *ordinary least squares* and seeks to minimize the residual, In other words this method estimates the unknown parameters with a linear regression model:

$$\operatorname{argmin} \ \|Ax - b\|_2^2 \qquad (4\text{-}4)$$

where $\| \ \|_2$ is the *Euclidean norm* also known as the ℓ_2 norm, by definition:

$$\|x\|_2 = \sqrt{\sum_i x_i^2} \qquad (4\text{-}5)$$

In case of an underdetermined system (e.g if $(A^T A)^{-1}$ does not exist), the least square solution model alone is no better than the original problem. In order to give preference to a particular solution with desirable properties, the regularization term is introduced and included in the model:

$$\|Ax - y\|_2^2 + \|\Gamma x\|_2^2 \quad (4\text{-}6)$$

where Γ is the *Tychonov matrix* which can be chosen suitably based on the desired solution that one may seek. In many cases, Γ is chosen as the identity matrix $\Gamma = I$, or a constant, giving preference to the solutions with smaller norms [28].

To see how the Tychonov penalty method can be applied to a de-noising problem, let's look at the example sparse signal $\rho(x)$, which we introduced earlier. However this time we add some random noise with Gaussian distribution to it with a standard deviation of $\sigma = 0.05$ (5% of the signal intensity peak).

$$y = x + noise \quad (4\text{-}7)$$

According to the Tychonov penalty model, one approach to de-noise the signal y, would be to solve the following:

$$argmin \qquad \|\hat{x} - y\|_2^2 + \lambda\|\hat{x}\|_2^2 \quad (4\text{-}8)$$

where λ is the regularization scale and $\hat{\rho}(x)$ is the desired solution. This optimization trades the norm of the solution with data consistency. Fortunately, this is a linear problem and very easy to solve. A closed from solution by putting the first derivative of it equal to zero:

$$\hat{x} = \frac{1}{1+\lambda} y \quad (4\text{-}9)$$

Apparently this solution tends to scale down the whole noisy signal in hope of reducing the noise. However one would predict that in addition to the noise, the sparse signal will also get scaled down and the signal to noise ratio (SNR) will remain the same. Simulations using different values for $\lambda = [0.01, 0.05, 0.1, 0.2]$ also agrees with that prediction:

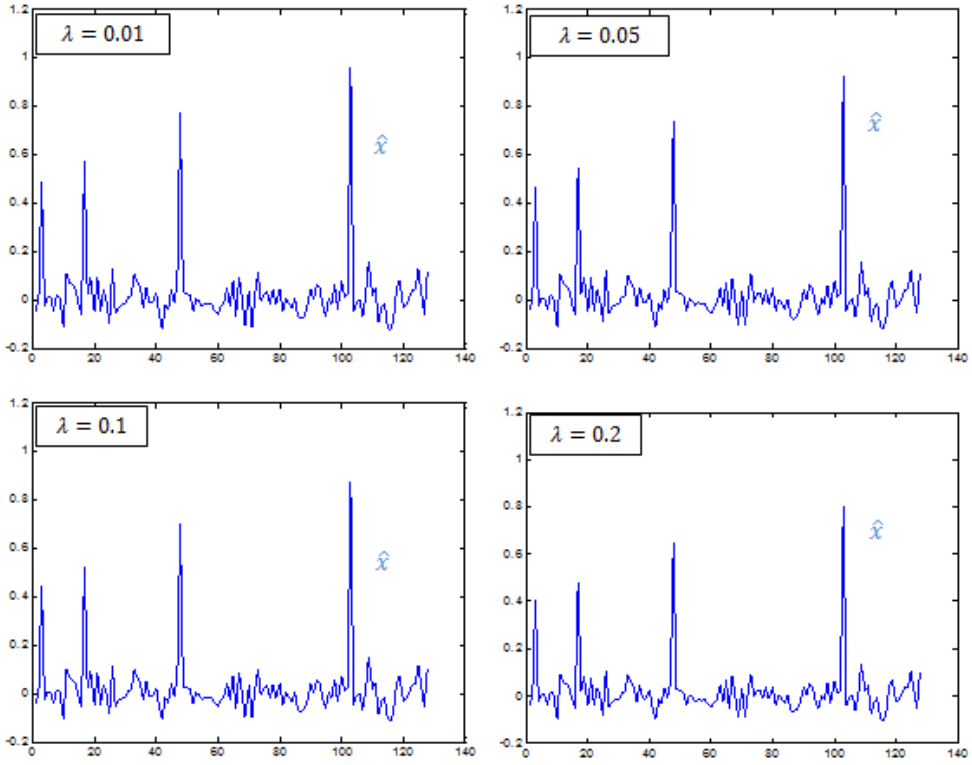

Figure 4.5, simulations of the recovered signal ($\hat{x}$) from the noisy signal (y) via applying the Tychonov regularization with different lambda factors: 0.01, 0.05, 0.1, 0.2.

As can be seen in Figure 4.5, the recovered signal is not any sparser than the original noisy signal y, which indicates this solution may not be suitable to recover the sparse coefficients of the signal. Qualitatively speaking, the regularization term in this solution, minimizes the energy of the whole signal and cannot distinguish between noise and valuable information while the other part tries to keep the data consistency.

4.2.4 The ℓ_1 norm and sparsity

An alternate approach to the regularization constraint is to replace the ℓ_2 norm with the ℓ_1 norm defined as:

$$\| x\|_1 = \sum |x_i| \qquad (4\text{-}10)$$

It has been shown that the ℓ_1 norm regularization can be an effective technique for solving underdetermined system of linear equations [29]. There has also been an increased interest in the statistical community to impose a ℓ_1 norm constraint on regression models (or least square fits).

$$argmin \qquad \frac{1}{2}\|\hat{x} - y\|_2^2 + \lambda\|\hat{x}\|_1 \qquad (4\text{-}11)$$

The presence of the ℓ_1 term encourages small components of $\hat{x}$ to become exactly zero, thus promoting sparse solutions. Since members of $\hat{x}$ ($\hat{x}_i$'s) are independent from each other, one can solve this problem, again in a closed form, for each element separately by solving:

$$argmin \qquad \frac{1}{2}|\widehat{x_1} - y_i|_2^2 + \lambda|\widehat{x_1}|_1 \qquad (4\text{-}12)$$

The solution is followed along its derivation:

$$\begin{cases} \text{for } \widehat{x_1} > 0 & argmin \quad \frac{1}{2}|\widehat{x_1} - y_i|_2^2 + \lambda\widehat{x_1} \\ \text{for } \widehat{x_1} < 0 & argmin \quad \frac{1}{2}|\widehat{x_1} - y_i|_2^2 - \lambda\widehat{x_1} \\ \text{for } \widehat{x_1} = 0 & \text{argmin} \quad \frac{1}{2}|\widehat{x_1} - y_i|_2^2 \end{cases}$$

$$\Rightarrow \begin{cases} \text{for } \widehat{x_1} > 0 & \widehat{x_1} = y + \lambda \\ \text{for } \widehat{x_1} < 0 & \widehat{x_1} = y - \lambda \\ \text{for } \widehat{x_1} = 0 & \widehat{x_1} = 0 \end{cases}$$

$$\Rightarrow \hat{x} = \begin{cases} y + \lambda & if \quad y < -\lambda \\ 0 & if \quad |y| < \lambda \\ y - \lambda & if \quad y > \lambda \end{cases} \qquad (4\text{-}13)$$

This solution leads to an effect also known as *soft-thresholding* (or *shrinkage*) which has become a very popular tool in computer vision and machine learning. Applying this solution to our example noisy signal y with different values for $\lambda = [0.01, 0.05, 0.1, 0.2]$, provides the following results:

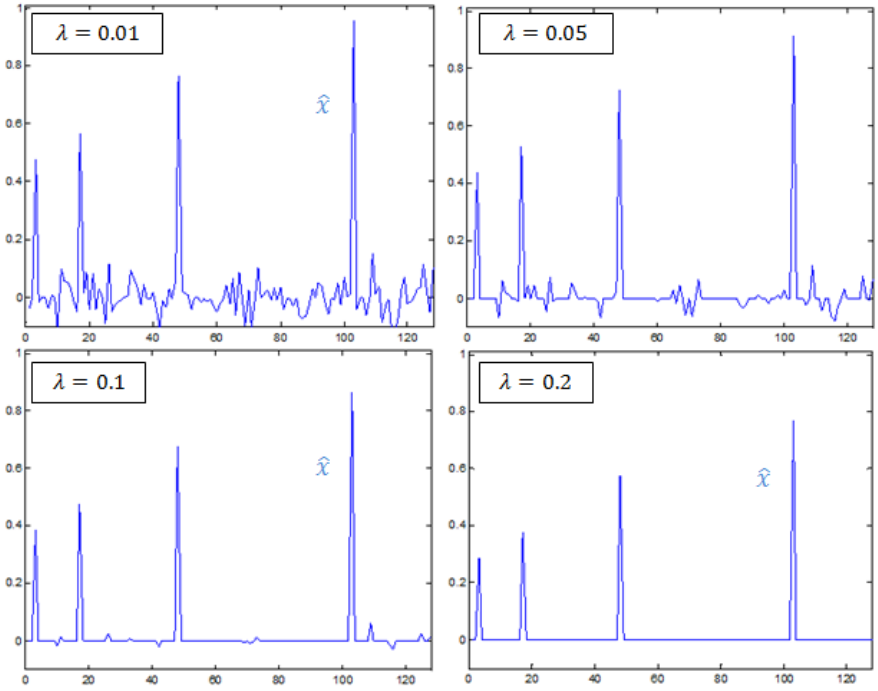

Figure 4.6, simulations of the recovered signal $\hat{x}$ from the noisy signal y with applying the ℓ_1 norm regularization with different lambda factors: 0.01, 0.05, 0.1, 0.2.

It can be seen that employing the $\ell_1 norm$ regularization, dramatically enhances the results compared to the Tychonov $\ell_2 norm$ regularization. The $\ell_1 norm$ regularization provides sparse results and most of the significant coefficients of the signal are recovered from the noisy signal. Figure 4.7 shows the performance of this approach comparing the original signal x and the recovered signal $\hat{x}$. In this case, the smallest signal component was lost during the thresholding process.

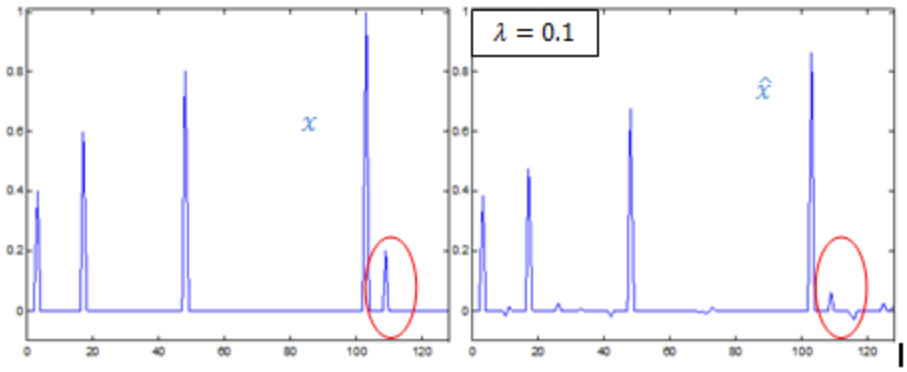

Figure 4.7, comparing the original signal (x) with the recovered solution ($\hat{x}$) from the noisy signal (y) using the ℓ_1 norm regularization approach. The performance of the recovery is superior compared with the Tychonov approach.

This loss of information would have been prevented if we could determine the interference of the noise and the signal and try to recover the small components buried under the noise. However in this case, the added white noise is completely independent of the original signal characteristics (e.g. is not due to undersampling) and such determination is not possible.

4.2.5 Recovery of the sparse signal from the randomly undersampled signal

Inspired by the de-noising problem and how we took an approach to recover the signal, we can revisit our randomly undersampled sparse signal which showed noise-like artifacts due to incoherent aliasing, and apply the $\ell_1 norm$ penalized minimization approach in hope of recovering the original signal. Substituting the problem parameters into equation (4-11), we want to solve:

$$argmin \qquad \frac{1}{2}\|F_r\hat{x} - y\|_2^2 + \lambda\|\hat{x}\|_1 \qquad (4\text{-}14)$$

where F_r is the Fourier operator which is only evaluated at a subset of random frequency domain samples, $\hat{x}$ is the estimated signal (reconstructed image) and y is the Fourier samples that we have acquired (collected k-space). Unlike the previous de-nosing problem, in this case the variables are coupled through a Fourier operator which indicates the lack of any possible closed form solution. There have been numerous attempts to solve such minimization problem [30-32] one of which is an iterative approach known as *HOMOTOPY* [33]. The word HOMOTOPY refers to the fact that in each iteration of a given solution, the objective function for the minimization problem (equation (4-14)) undergoes a HOMOTOPY from the ℓ_2 constraint to the ℓ_1 objective. This kind of algorithm is also known as Projection Over Convex Set (POCS) [26].

We apply this type of approach as follows iteratively by initially assuming $\widehat{K} = F\hat{x}$ and setting $\widehat{K}_0 = y$:

1- Computing the inverse Fourier transform to get an estimate of the signal $\widehat{x'}_i = F^{-1}\widehat{K}_i$.

2- Apply the soft-thresholding function at the signal domain ($Soft - thresh(\widehat{x'}_i, \lambda)$).

3- Compute the Fourier transform of the thresholded signal, $\widehat{K'}_i = F\widehat{x'}_i$.

4- Enforce data consistency in the frequency domain. This step simply puts the new frequency samples recovered from the previous step and adds to the already collected samples:

$$\widehat{K}_{i+1}[j] = \begin{cases} \widehat{K'}_i[j] & if\ y[j] = 0 \\ y[j] & otherwise \end{cases} \qquad (4\text{-}15)$$

5- Repeat until $\|\hat{x}_{i+1} - \hat{x}_i\| < \epsilon$.

One should note that since we are dealing with complex signals, the soft-thresholding function should be modified so it can handle complex values:

$$Soft-thresh(x,\lambda)=\begin{cases}0 & if\ |x|<\lambda\\ \frac{(|x|-\lambda)}{|x|} & if\ |x|>\lambda\end{cases} \quad (4\text{-}16)$$

We ran this iterative algorithm on the same randomly undersampled data (x_r) for different regularization factors, $\lambda=[0.01, 0.05, 0.1]$ and Figure 4.8 shows the results. In each case of λ, the number of iterations needed to reach a convergence was different. The choice of lambda (the regularization factor) has a tremendous effect on the features of the recovered signal ($\hat{x}$). The larger the λ, the more the solution will tend to be close to zero ($\hat{x}=0$) and as $\lambda\to 0$, $\hat{x}$ converges to the ultimate sparse solution [31]. In this example, $\lambda=0.01$ seems to have the most accurate and sparse results compared to the original signal x. In Figure 4.8, you can see how even the smallest components of the signal can be recovered using a very small choice of λ, and how the algorithm can lose the same components in greater choices of λ. One should note that the number of iterations for smaller choices of λ can be much more than larger ones. This can be considered as a tradeoff between the computation cost and accuracy of the algorithm.

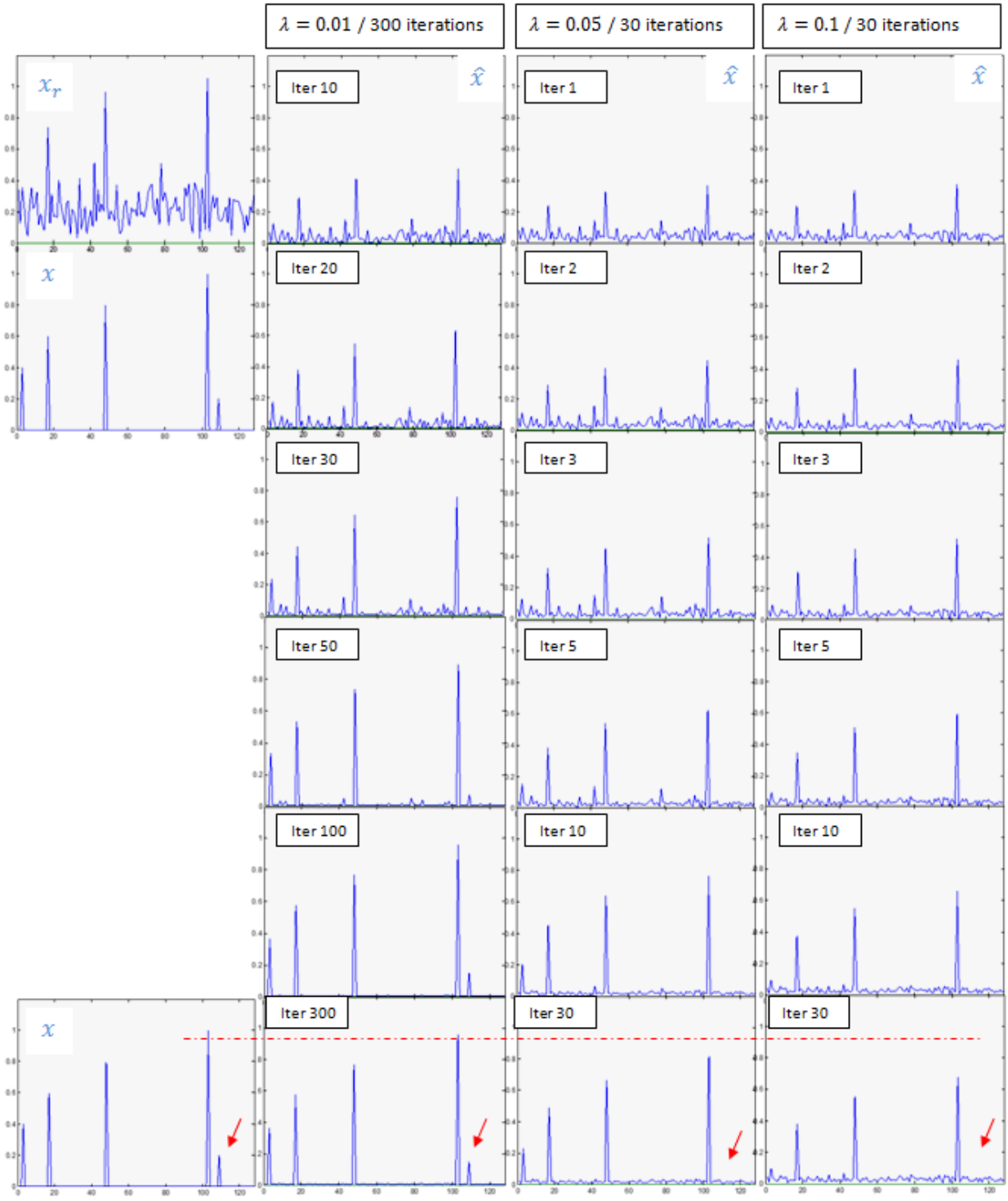

Figure 4.8, The iterative process of recovering the undersampled signal (x_r) with 25% random undersampling via different lambda factors.

We wish to push the undersampling as small as possible and study how well this iterative algorithm performs. In the next example, we consider starting with only 12.5% of the total Fourier domain information. Figure 4.9 shows the undersampling scheme and its corresponding artifacted reconstructed signal x_r. At this level of undersampling, the straight forward zero-filled reconstructed signal x_r, is almost purely artifacts and cannot be compared to the original signal x.

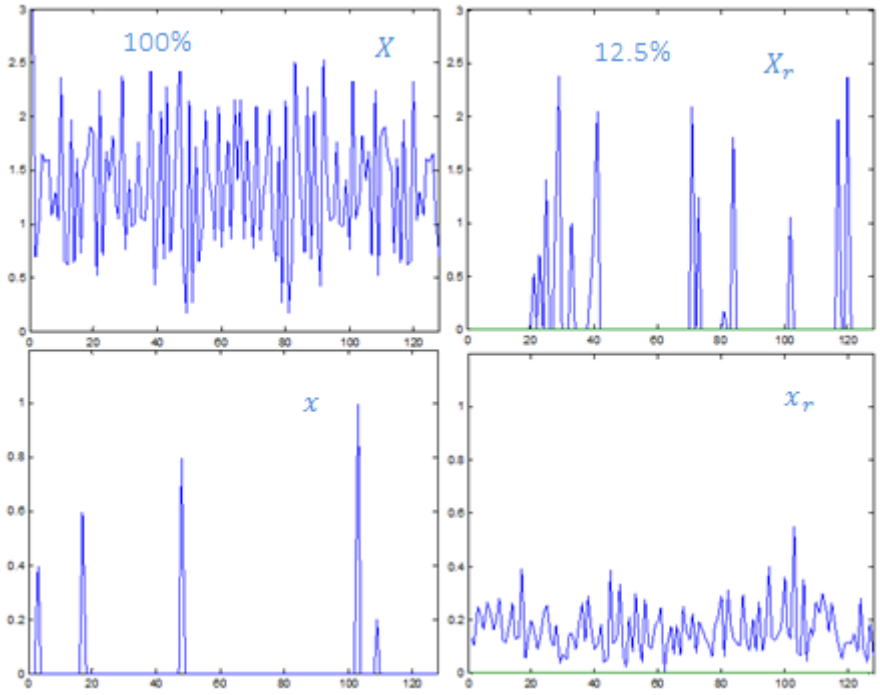

Figure 4.9, the 12.5% random undersampling of the Fourier samples (X_r) and its corresponding artifacted reconstructed signal x_r. It has severe incoherent aliasing artifacts and the sparse signal is almost completely lost.

Using the same $\ell_1 norm$ iterative POCS approach as above, it can be seen that the results are not as accurate (Figure 4.10) and the small components of the original signal may get lost during the recovery process.

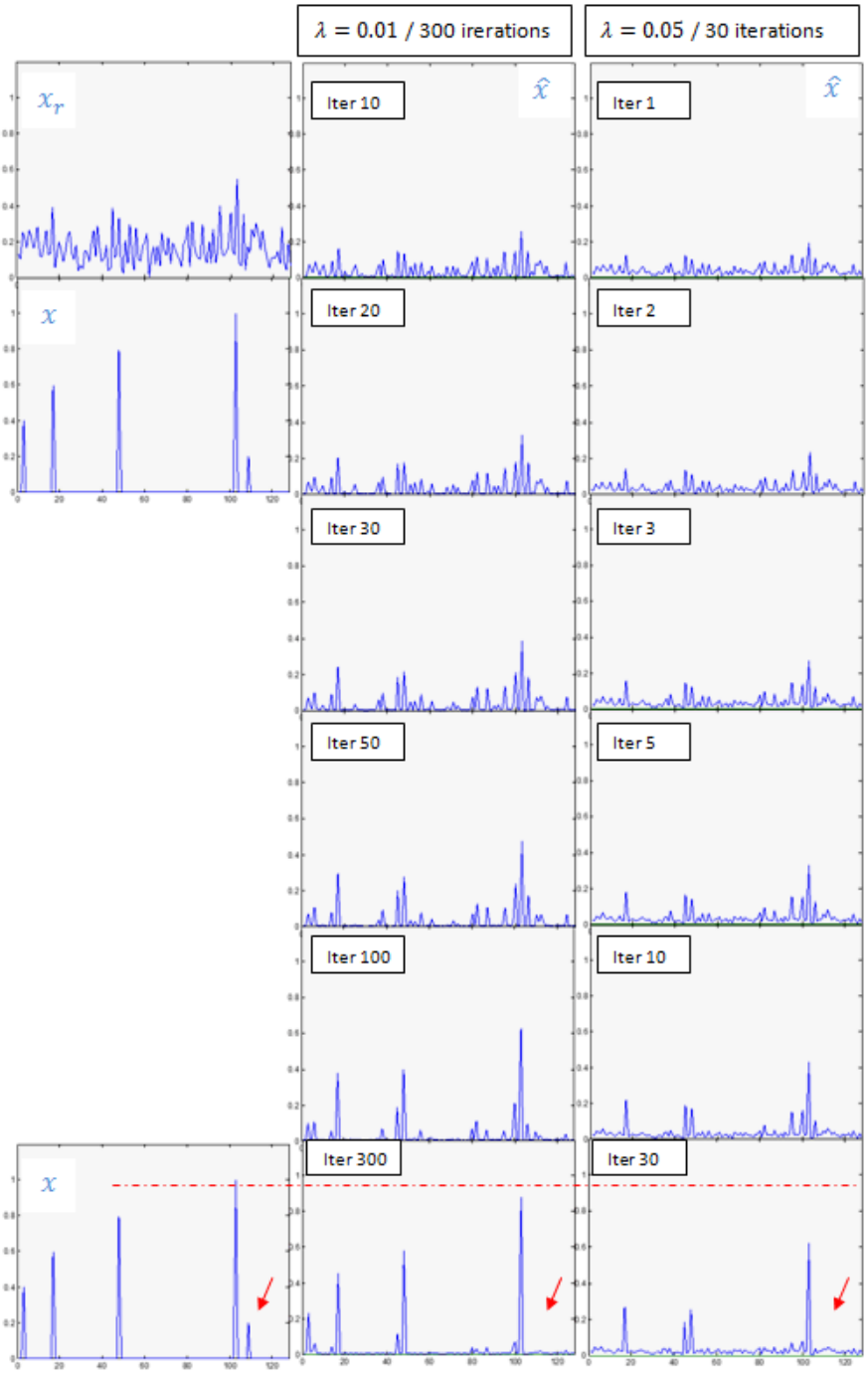

Figure 4.10, The iterative process of recovering the 12.5% undersampled signal (x_r) via the ℓ_1 norm regularization approach using two different lambda factors. The algorithm did not perform as well as in the case of 25% undersampling (Figure 4.8)

4.3 Sparsity of magnetic resonance images and sparsifying transforms

Generally medical images and more particularly MR images, do not have a sparse representation nature. Although there can be some exceptions to this as in MR angiography for example, the sparsity feature of different MR images will vary according to their contrast behavior.

Therefore, in order for CS to work for MR images, one should seek a *sparsifying transform*. A sparsifying transform is defined as an operator which maps an image vector (natural images or MR images) into a sparse vector space [34]. Due to the interest in sparse signal and image representation in the past few years, research has resulted in a diverse library of sparsifying transforms for different types of images [35]. Here we mention only two of them.

4.3.1 Finite difference

For instance, *finite difference* can be used to represent *piecewise constant* images in a sparse domain. In a piecewise constant image, the boundaries and edges are the most important features and away from the boundaries the voxel values do not differ too much. Mathematically, finite difference is a numerical method for calculating an approximate of the derivative of the function $f(x)$:

$$f'(x) \cong \frac{f(x+a)-f(x)}{a} \quad (4\text{-}29)$$

In a more general format a finite difference is a mathematical expression of the form:

$$f(x+a) - f(x+b) \quad (4\text{-}30)$$

Finite difference transform, computes the differences between neighboring voxels and creates a sparse map of boundary information. This map is sometimes called a gradient map of the image

as well. For general MR images, finite difference may not be a good sparsifying transform since they usually are not piecewise constant.

Phantoms are usually good examples of a piecewise constant objects and finite difference can be a perfect tool for sparsifying such images. Figure 4.11 shows a phantom MR image and its corresponding finite difference map which looks perfectly sparse showing only the enhanced edges.

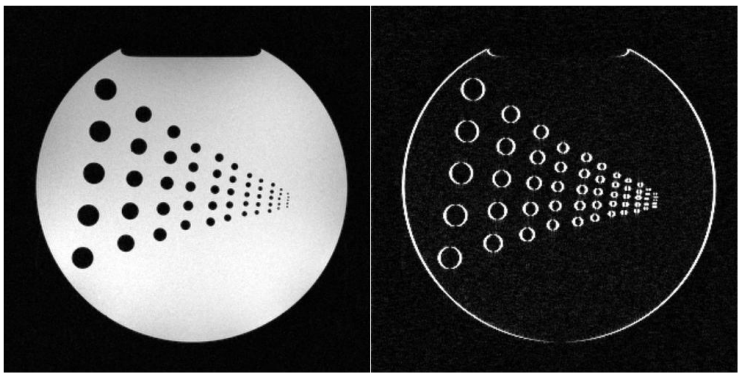

Figure 4.11, A phantom image (on right) which is a perfect example of a piecewise constant image. The corresponding sparsifying transform (finite difference) which has the ultimate sparse features showing only the boundary information.

4.3.2 Wavelet

Studies on image compression methods in computer science have shown that for natural images, discrete cosine (DCT) and Wavelet transforms are two suitable sparsifying tools [36]. DCT and Wavelet are the central tools in the JPEG, MPEG and JPEG-2000, image and video compression standards which are being used billions of times everyday to represent images and videos in our digital lives. JPEG-2000 specifically used the Wavelet transform in order to compress digital images with the goal of reducing their size without noticeable perceptual loss.

Over the past few years, Wavelet theory has been proven to find multiple applications in different fields of signal processing and continues to grow rapidly. However, most of the literature are highly mathematically oriented and need a major time investment in order to understand. Here we try to provide a brief overview of the Wavelet theory from an intuitive standpoint.

4.3.2.1 Wavelets and Wavelet transform

The "*Wavelet* transform" is a multi-scale representation of the digital signals. The words "*Wavelets"* however refers to a group of functions which should satisfy certain requirements. The name Wavelets refers to the fact that these functions should integrate to zero over their entire length (i.e. waving above and below the x-axes) (Figure 4.12).

Although there are similarities between Fourier transform and Wavelet transform, there are advantages in the Wavelet transform which makes them superior for analyzing non-stationary phenomena. The Fourier transform is best suited for analyzing stationary periodic signals. It provides a single spectrum for the whole signal. Therefore Fourier transform is not suitable for analyzing signals such as a musical melody as a succession of notes, each with its own specific frequency spectrum[2].

Wavelet transforms decompose a signal into multiple frequency bands by projecting the signal onto different elements of a set of basis functions (Wavelets). These frequency bands are also known as "*scales"*. Projecting the signal into different scales is equivalent to band-pass filtering the signal. Wavelets are all similar to each other and only differ from each other by

[2] Short time Fourier transform can be used for such signals. However it is out of the scope of this thesis to discuss.

dilation and /or *translation* (Figure 4.13). There are many different families of Wavelets each designed and suitable for particular applications. One of the famous Wavelet families with orthogonal members are grouped together and known as Daubechies [37].

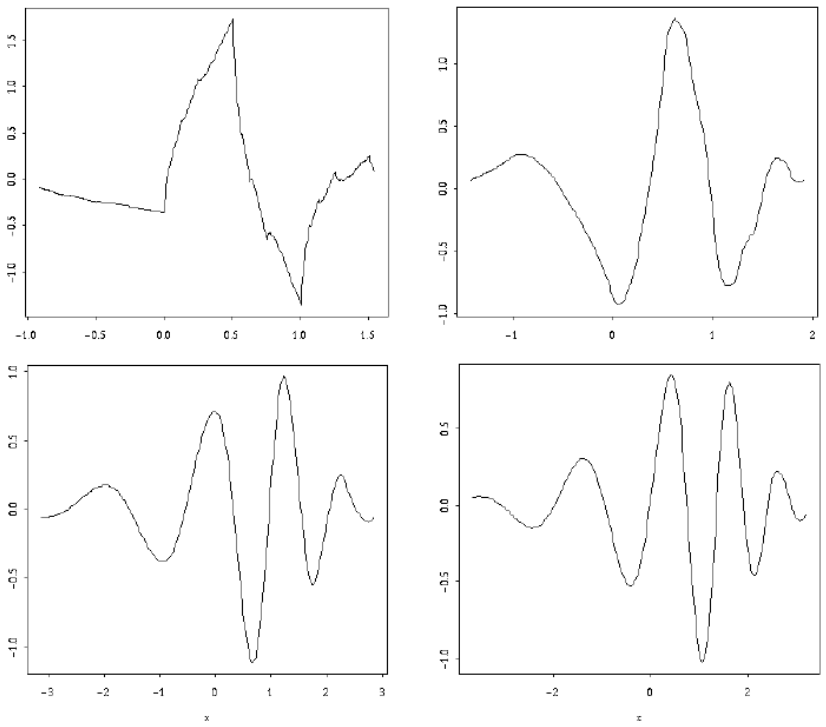

Figure 4.12, Wavelets from the Daubechies family [38].

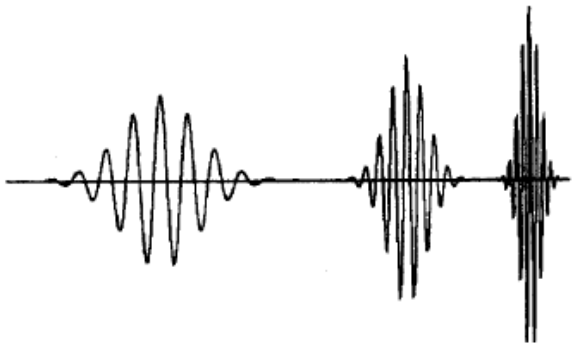

Figure 4.13, The wavelet basis functions are self-similar: scaled in time to maintain the same number of oscillations and scaled in amplitude to maintain energy (dilation and translation) [39].

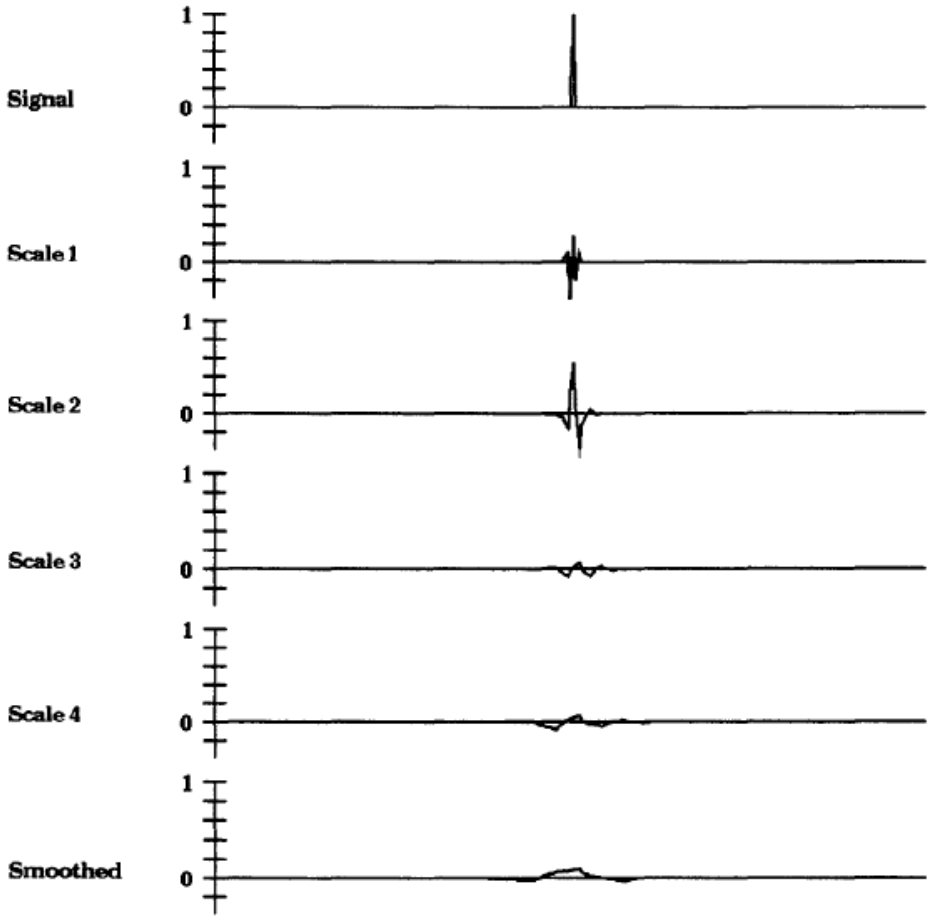

Figure 4.14, Wavelet transform of an impulse function using the four coefficient Daubechies wavelets, *W4 [39].*

4.3.2.2 Multi-resolution analysis

A multi-resolution analysis is simply a Wavelet transform which can be used to represent an image in multiple scales. The wavelet transform decomposes a signal into a smoothed version of the original signal and a set of detail information at different scales [39]. The detailed information for images will be that which distinguishes edges. Once we remove this information from the image, we are left with a new image which is slightly blurred. The *coarse-scale* wavelet coefficients represent the blurry low resolution image while the *fine-scale* coefficients represent

the detail information of the sharp edges. This process can be repeated recursively to multiple levels. For images, each wavelet coefficient, contains both spatial and frequency information. Given the decomposition, the original image can be reconstructed using its corresponding scaled versions.

The behavior of each element of a decomposed image can be analyzed across different scales. Noise has a very distinct behavior across the scales, and thus can be easily distinguished from the signal and manipulated as needed. This is actually a very novel method for de-noising image signals which is achieved by removing the noise from the signal across Wavelet scales and then reconstructing the noise-free image [40]. This important feature can be used in our specific application of compressed sensing when we attempt to de-noise the signal in hope of removing incoherent aliasing artifacts from the undersampled signal.

One should note that Sparsity is not limited only to the spatial domain. Dynamic images are extremely sparse in the temporal dimension and Wavelet theory can be utilized in that dimension as well.

Figure 4.15 illustrates how a 2D Wavelet transform decomposition works. In order to understand this process, we simplified the equivalent of each block. The details of this process are beyond the scope of this thesis.

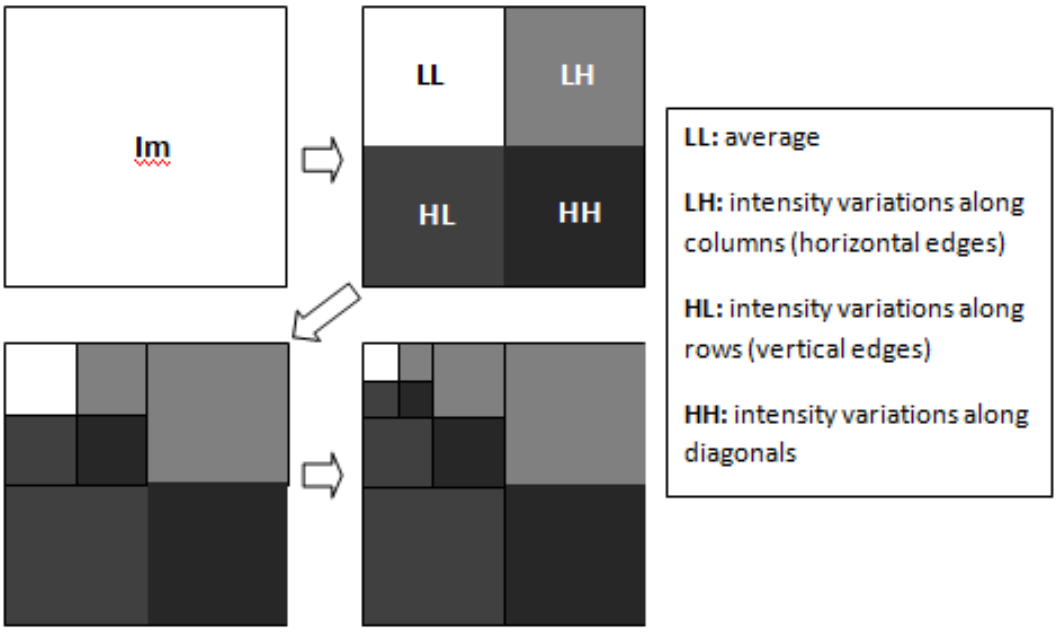

Figure 4.15, Illustrating 2D Wavelet decomposition. Each block decomposes further and further by applying three Wavelet filters on the original image. The nature of these filters are simply mentioned above, however details are not at the scope of this paper.

Figure 4.16, shows a 2D image example and how the Wavelet transform decomposes it into different scales. Also it can be seen how Wavelet coefficients are sparse which makes it a naturally suitable sparsifying transform for compression or de-noising algorithms.

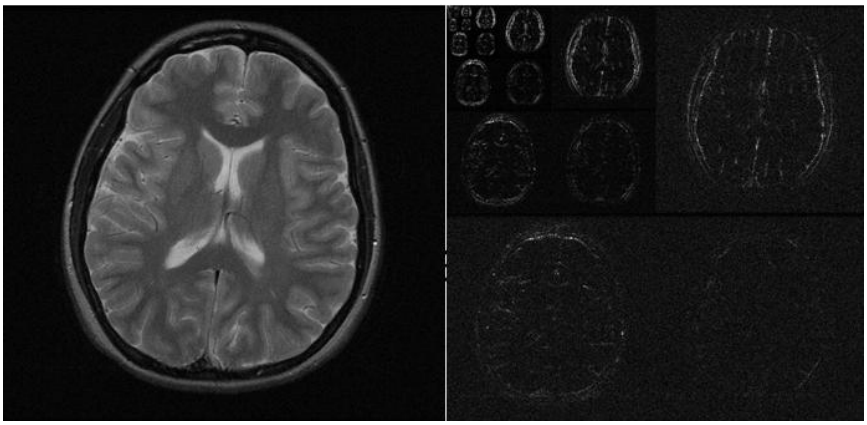

Figure 4.16, A 2D MR image example (on left) and its corresponding Wavelet transform. It can be seen how the Wavelet transform decomposes the image into different scales. Image reproduced from [26].

4.4 Undersampling of images in k-space

In this section, we evaluate the role of undersampling in k-space as it applies to MR imaging. We will use high resolution phantom images to produce a set of k-space that can then be undersampled as desired to test the CS reconstruction. We will consider a number of different approaches to modify k-space that also leads to reduced imaging time.

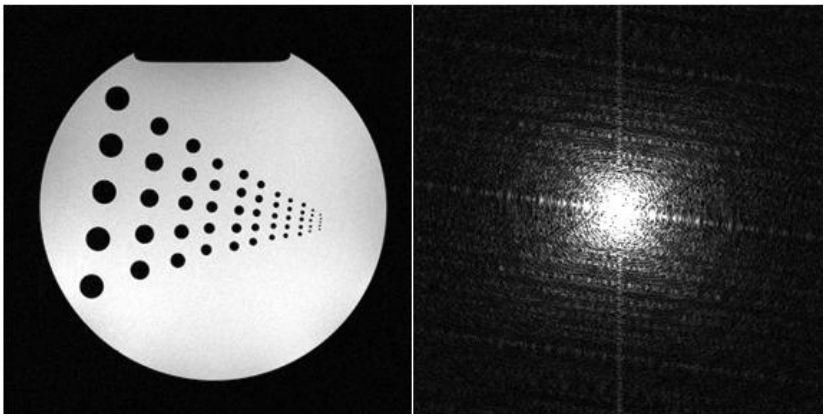

Figure 4.17,Example of the relationship between the magnitude image and its associated k-space. The general rule of thumb indicates that the k-space data is more spread out along the direction parallel to the shorter elements of the image. In this case the circular shape the image results in the ball-shape of the k-space.

One approach to undersample the k-space is to acquire a reduced number of phase encoding lines by skipping every other line. In other words as an example we want to collect only half of the number of phase encoding lines required by the Nyquist criterion (50% undersampling).

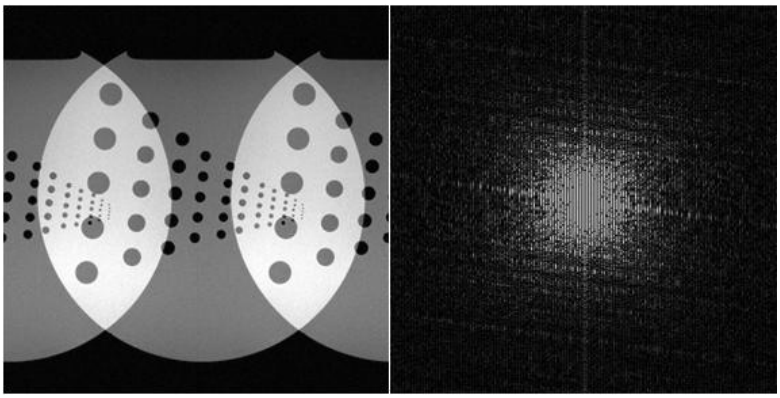

Figure 4.18, 50% undersampled k-space by missing every other phase encoding line and its associated reconstructed image with coherent aliasing artifact.

As can be seen in Figure 4.18, the reconstructed image manifests coherent aliasing which is usually impossible to resolve. If we push the undersampling even further to 25% the extent of aliasing elevates to the point which makes it hard even for our eyes to recognize the original object Figure 4.19.

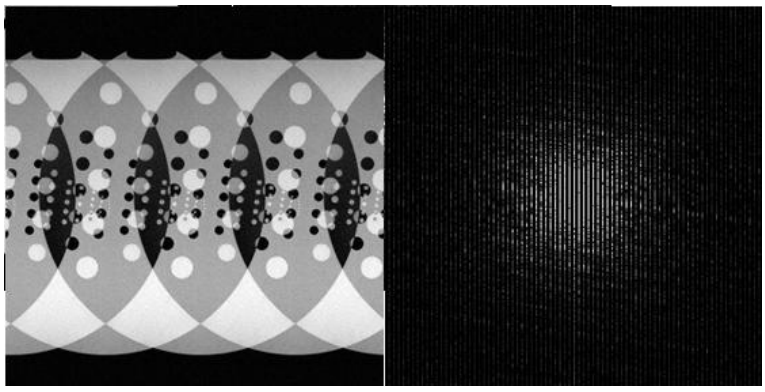

Figure 4.19, 25% undersampled k-space by missing one fourth the total phase encoding lines required by the Nyquist criterion and its associated reconstructed image with severe aliasing artifact.

A modern way for removing this aliasing due to undersampling comes from parallel imaging techniques. However, that is not the focus of this thesis. On the other hand, we observed that incoherent undersampling (random undersampling) will result in incoherent aliasing which usually manifests itself in the image with a noise-like behavior. This is why CS is

only viable using random undersampling [25, 34]. This can be demonstrated using the same phantom image example with the same number of samples as in the coherent undersampling example.

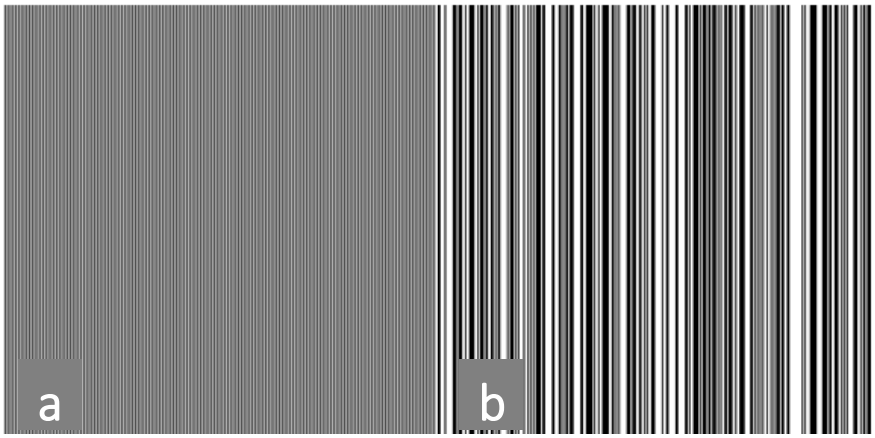

Figure 4.20, Comparing the (a) equispaced and (b) random k-space sampling scheme both for 50% undersampling. The equispaced scheme may not be shown well in the print due to low resolution.

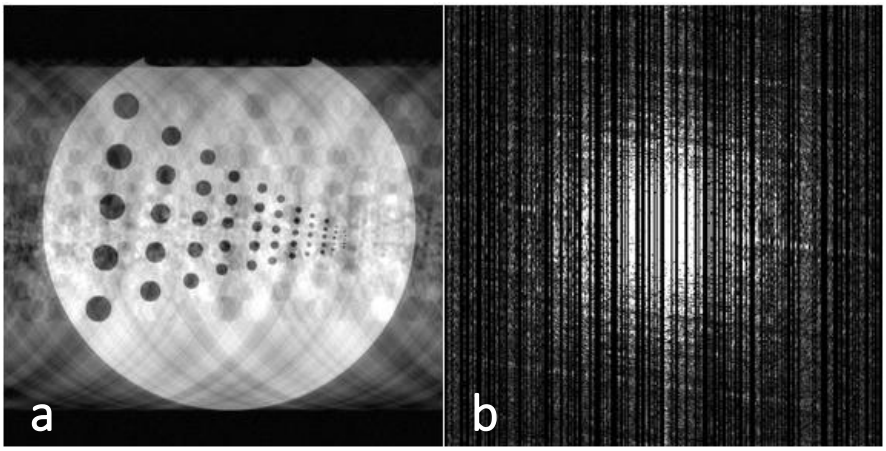

Figure 4.21, 50% randomly undersampled (b) k-space and (a) its corresponding reconstructed image. The random sampling scheme results in in-coherent aliasing artifacts in the reconstructed image which are easier to remove.

Although we demonstrated earlier with the 1D example that random undersampling can provide relatively recoverable images, keeping the center of k-space can dramatically improve the reconstruction. We can define a probability density function (PDF) with higher values (closer to 1) at the center of k-space and set our sampling function to follow this PDF for choosing k-

space samples. This sampling scheme will lead to an undersampled k-space which is sampled more densely at the center rather than its periphery (high-spatial frequency information or *outer k-space*) (Figure 4.22).

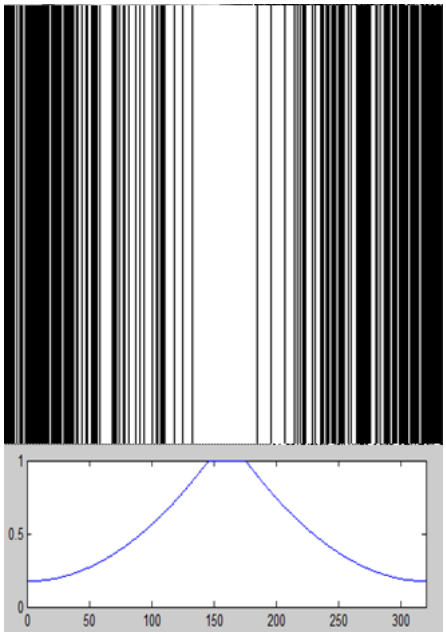

Figure 4.22, Variable density sampling scheme (with only 50% of the full samples) which takes more samples at the center of k-space rather than the outer k-space. This is feasible by setting the sampling function to follow a probability density function (PDF) which has higher values around the center of k-space.

By applying the variable density sampling scheme to k-space there is a noticeable improvement in the reconstructed image in Figure 4.23.

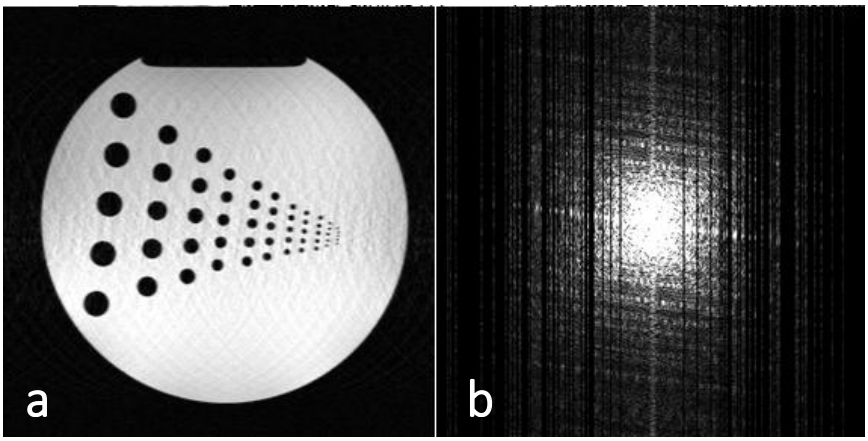

Figure 4.23, 50% undersampled k-space with variable density scheme in Figure 4.22, and its corresponding reconstructed image with noticeably less artifacts.

4.4.1 3D k-space undersampling

The results of the previous 1D example suggest that the CS sampling concept can be extended to higher dimensions where phase encoding is used to collect the data. A reduction of acquisition time by a fact of "p" for an n-dimensional sequence will reduce the scan times by a factor of $p^{(n-1)}$. Therefore, we anticipate that this approach could be a powerful means to speed up 3D, 4D and higher dimensionality imaging methods.

Figure 4.24 shows the 2D undersampling scheme covering both phase encoding and partition encoding directions and how it applies to the same phantom image in a 3D imaging experiment:

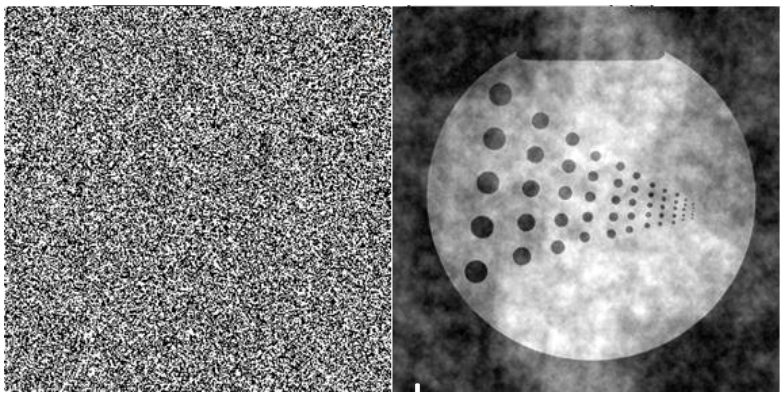

Figure 4.24, 50% randomly undersampled k-space and its corresponding reconstructed image with incoherent aliasing artifacts. Comparing to the Figure 4.21 we can see how undersampling in both directions increases the incoherency of the aliasing artifacts.

Variable density technique can also be applied in the same way as in 2D imaging by defining a two dimensional PDF.

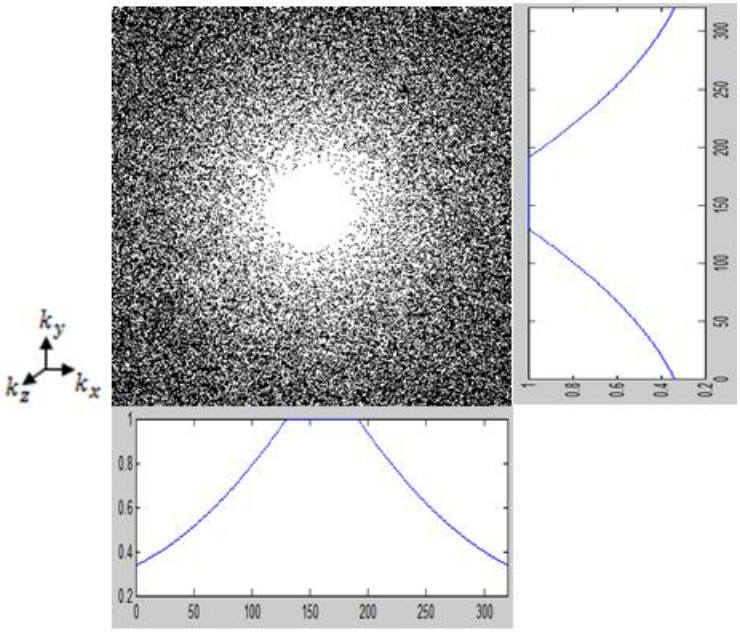

Figure 4.25, $k_y - k_z$ plane in a 3D k-space with 50% random undersampling and variable density in both directions.

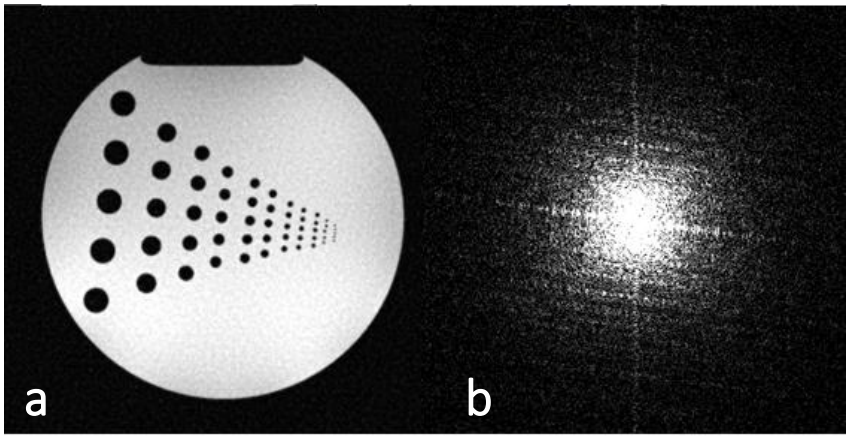

Figure 4.26, 50% 2D random variable density undersampled (b) k-space and (a) its corresponding reconstructed image. The resulting aliasing artifacts are almost invisible due to incoherency in both ky and kz directions.

Figure 4.27 shows a comparison between different sampling schemes we introduced so far and their corresponding reconstructed images all with the same 50% undersampling. The extent and nature of aliasing artifacts can be better understood if we subtract the undersampled images from the original fully sampled image. The variable density sampling with more samples at the center of k-space appears to improve the reconstructed image and reduce the coherency of the aliasing artifacts dramatically.

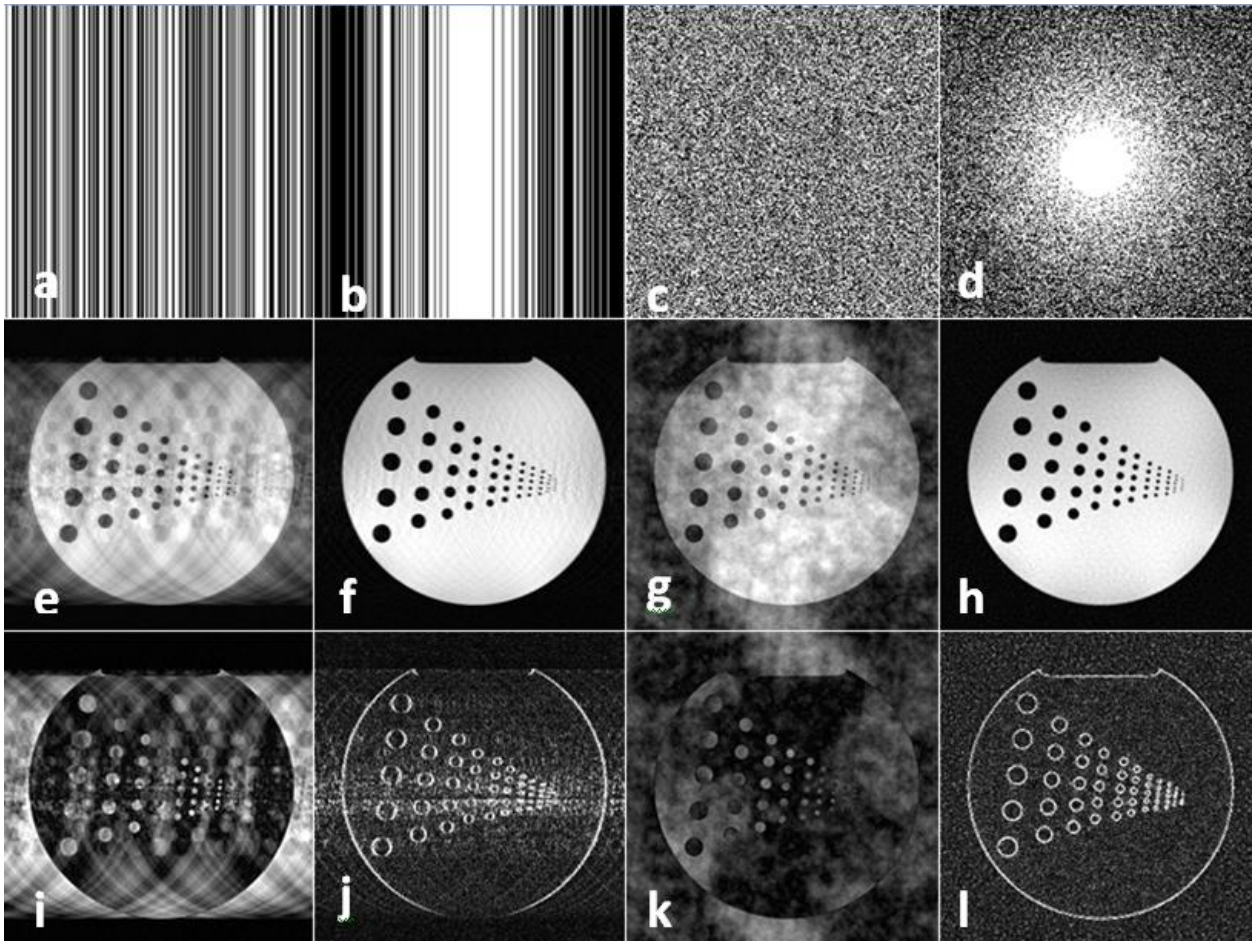

Figure 4.27, Comparison of different undersampling schemes all with the same 50% undersampling factor. (a) one directional random scheme, (b) one directional random variable density scheme, (c) two directional random scheme, (d) two directional random variable density scheme. (e-h) corresponding undersampled reconstructed image, (i-l) corresponding difference image which shows the artifacts created solely due to undersampling of k-space.

The two dimensional random variable density undersampling shows the best reconstruction and creates aliasing artifacts which are very similar to Gaussian noise in their appearance. This is the cornerstone of CS reconstruction since the noise-like behavior of incoherent sampling artifacts and the sparsity of the image change the underdetermined undersampled image reconstruction problem (which is ill-posed) into a simple de-noising problem (which is usually well-posed). In the end, the goal is to reconstruct the equivalent image that would have resulted from the fully sampled k-space.

4.5 Application: Compressed Sensing MR Angiography

In this section we apply the same undersampling and reconstruction concepts introduced in the above 3D example and apply them to MR angiography (MRA) imaging. For the purpose of simulations, we acquired a very high resolution 3D gradient echo MRA on a volunteer's head at a 3T Siemens scanner. The imaging parameters for this sequence were set to collect the image with an isotropic resolution of 0.5x0.5x0.5 mm^3, a matrix size of 448x336x192, TE=7.25 ms, TR=30 ms, FA= 20° and BW=80 Hz/pixel. We collected the data sagittaly so the read encoding direction would be cranial/caudal (Figure 4.28). This will result in the most incoherency of the artifacts in the transverse images, which are clinically most familiar. The entire coding and visualization of the images prepared for this part are done in the MATLAB software (The MathWorks Inc.).

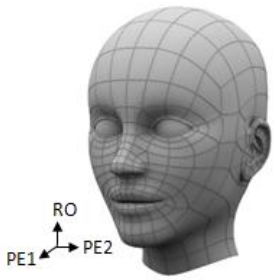

Figure 4.28, Image acquisition orientation for compressed sensing MRA.

4.5.1 Methods

For all simulations we reconstructed the images to a 512x512x192 matrix size by zero filling the image domain. This is done for two reasons: simplicity of simulations and coding, and the fact that the wavelet toolbox which is used [41] for simulations is only compatible with square matrices. All the results will be presented as transverse images since it's clinically more

familiar. We chose only 30 transverse slices for the purpose of this simulation. Figure 4.29, shows some sample images of this MRA dataset.

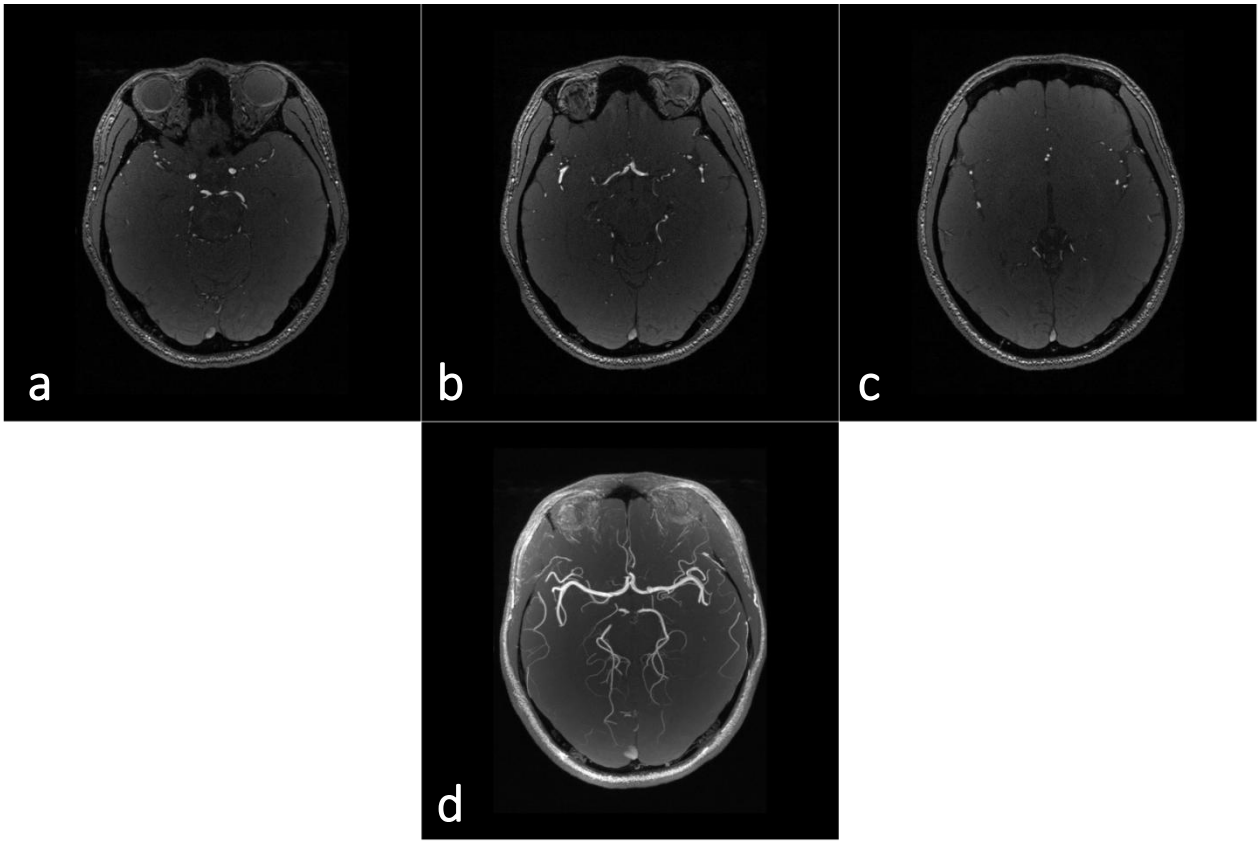

Figure 4.29, MRA example images reconstructed in 512x512 transverse matrix size. (a-c) show three images from lower, middle and higher sections of the brain respectively, providing anatomical information with a high contrast for the vessels. (d) shows a Maximum Intensity Projection (MIP) over 30 slices (including the ones shown here). The MIP image shows the vascular system across the brain with a good contrast between the background tissue and blood vessels.

4.5.2 Undersampling

Throughout this section we are going to demonstrate undersampling factors of 20%, 30% and 50% in the ky-kz domain which can potentially speed up the 3D acquisition scheme by 5, 3.3 and 2 times respectively. For all the undersampling factors we kept roughly only 6% of the central k-space fully sampled. The periphery of the k-space is randomly sampled with a variable density following a second degree PDF. In order to maximize the incoherency of a given number

of samples, the random sampling schemes were created using a Monte Carlo algorithm in MATLAB [34]. In order to compare different factors, undersampled k-spaces were *zero-filled* and the images were reconstructed by applying a 3D inverse Fast Fourier Transform (FFT). The undersampling artifacts can be compared by reviewing the individual slices as well as the MIPs. Figure 4.31 demonstrates how vascular information can be buried under the aliasing artifacts due to undersampling.

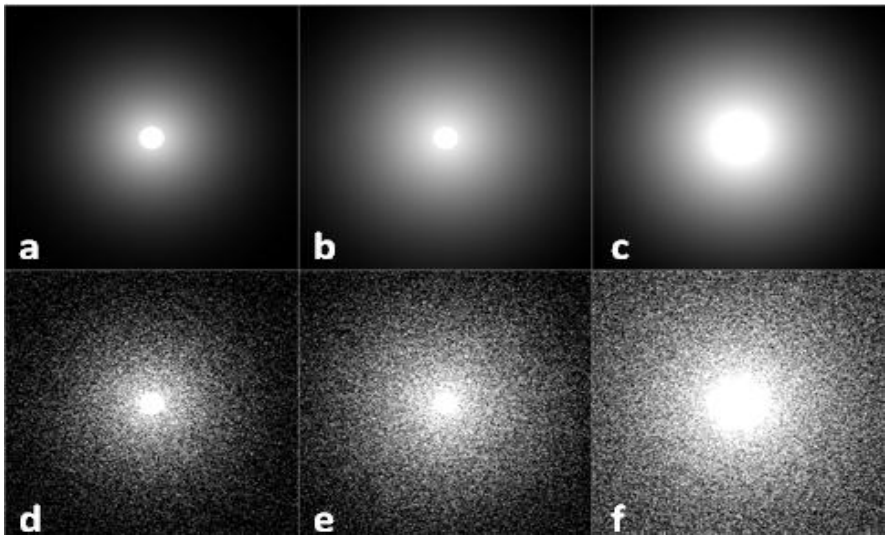

Figure 4.30, Comparison of different undersampling factors. (a-c) showing the probability density function for variable density sampling with 20%, 30% and 50% undersampling factor respectively. (d-f) sampling scheme for undersampling factors of 20%, 30% and 50% respectively.

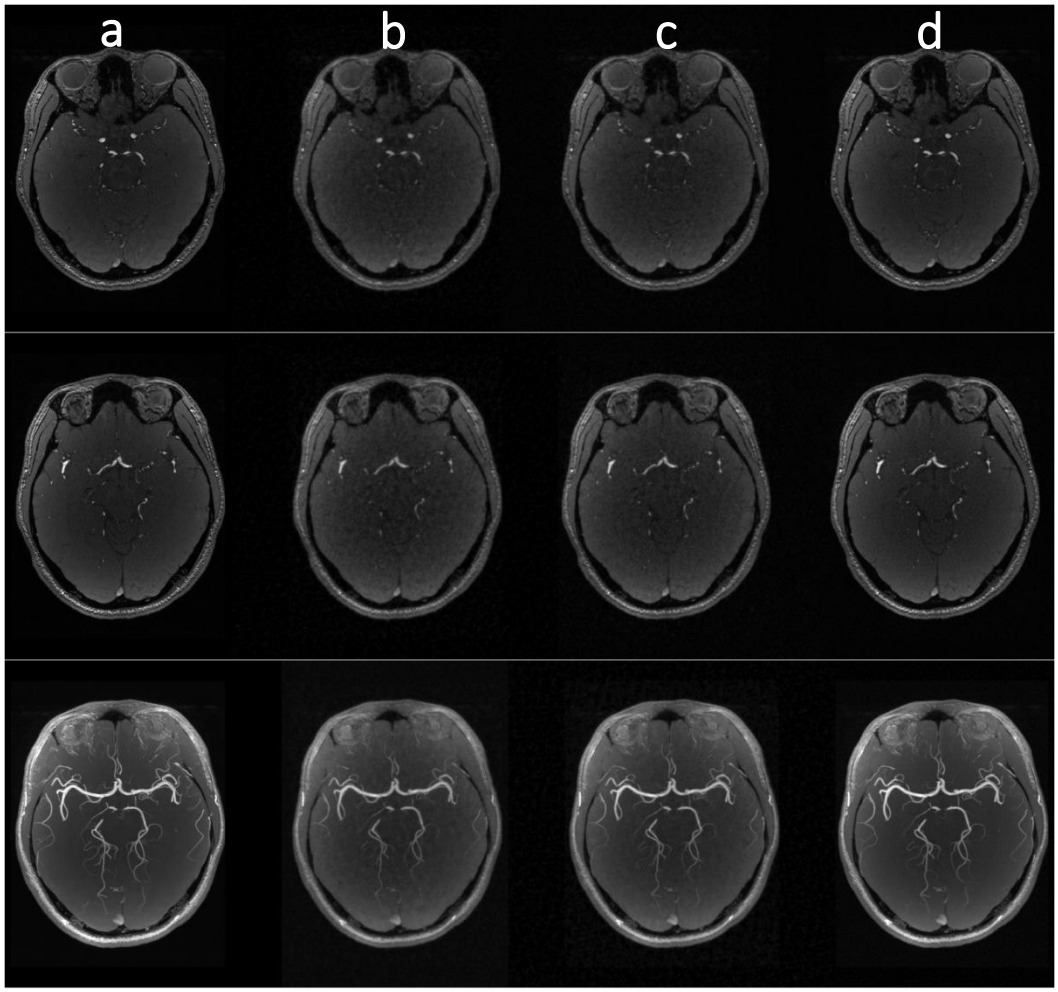

Figure 4.31, Comparison of different undersampling schemes and their resulting zero-filled reconstructed images. The upper two rows show single slice examples from lower and middle sections of the brain. The third row compares the MIPs. (a-d) columns respectively correspond to 100% (fully sampled), 20%, 30% and 50% undersampling.

4.5.3 Sparsifying Transform

Generally, the zero-filled reconstructed images are not fully sparse in the image domain, therefore we use the Wavelet transform we introduced earlier to sparsify these images. Each slice of the 3D volume of interest should be sparsified and processed individually. Once they are sparsified, we can apply any algorithm to separate the noise-like artifacts from the actual signal

(object). This includes any solution to the regularization problem we reviewed in Chapter 4.2, such as Conjugate gradient methods, POCs, etc. We use the simple solution of iterative soft-thresholding we discussed earlier. We chose the thresholding factor for each image automatically by calculating the largest 5% Wavelet coefficients. This may induce total energy inconsistencies between different slices of the volume and needs to be compensated for. To do so, we will normalize all the images based on their average signal intensity before putting them all in a single volume for further processing.

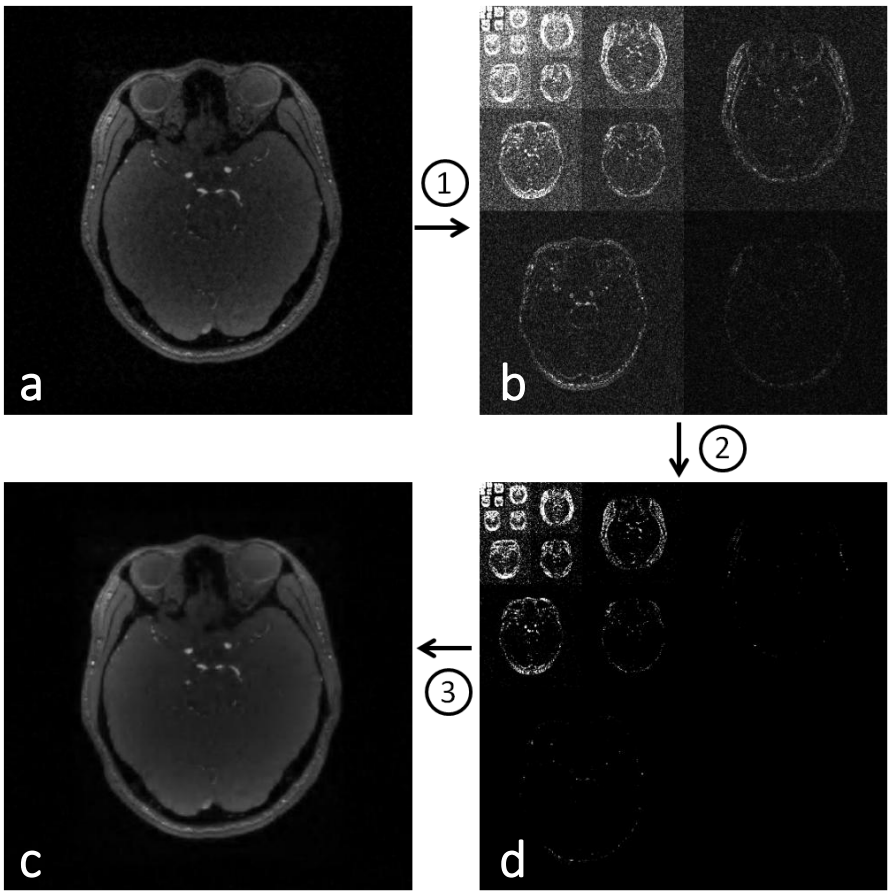

Figure 4.32, The sparsifying and thresholding iteration loop. (a) the undersampled, zero-filled image with incoherent aliasing and blurring, (b) Wavelet transform sparsifies the image domain, making it easier to separate noise-like artifacts from the actual object. (d) the soft-thresholded Wavelet coefficients showing considerably less noise-like artifacts. (c) The inverse Wavelet transform creates a cleaner, patchier, sparser image. The Fourier transform of this image will be used to fill in the missing k-space information.

4.5.4 Generating new k-space information

After one round of removing the artifacts in the sparse domain (wavelets), the Fourier transform (k-space) of the newly generated image (Figure 4.32-C), can provide us with some estimate of the missing information (encoding lines) in the original undersampled k-space. Iteratively recovering more of the signal buried under the noise-like artifacts, this procedure can provide us with better and more accurate estimations of the missing k-space information. The number of iterations can be controlled with a breaking criterion according to the data consistency expression being evaluated at each iteration. The evolution of an undersampled k-space (zero-filled) towards an estimated recovery of the missing k-space information can be seen in Figure 4.30.

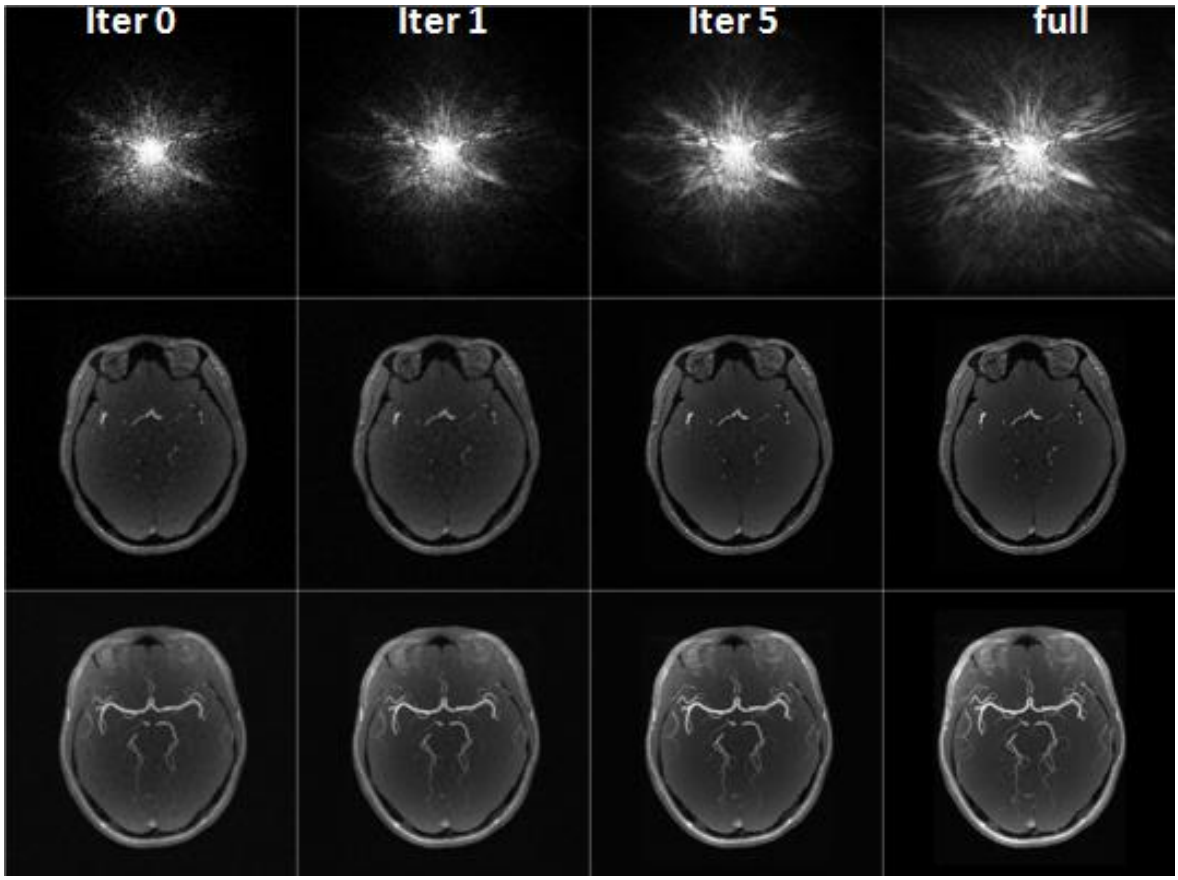

Figure 4.33, The progress in estimating new k-space information through the CS reconstruction iterations for a 20% undersampling scheme. First row shows the k-space, second row shows a single slice and the third row shows a MIP though iteration 0 (zero-filled), iteration1, iteration 5 (last iteration) and the fully sampled.

4.5.5 Results

The aforementioned algorithm is described in the form of a flowchart in Figure 4.33. Also the reconstructed images in each iteration are shown for two example slices as well as MIP images compared to the zero-filled and fully sampled reconstructions (Figure 4.35 and Figure 4.36).

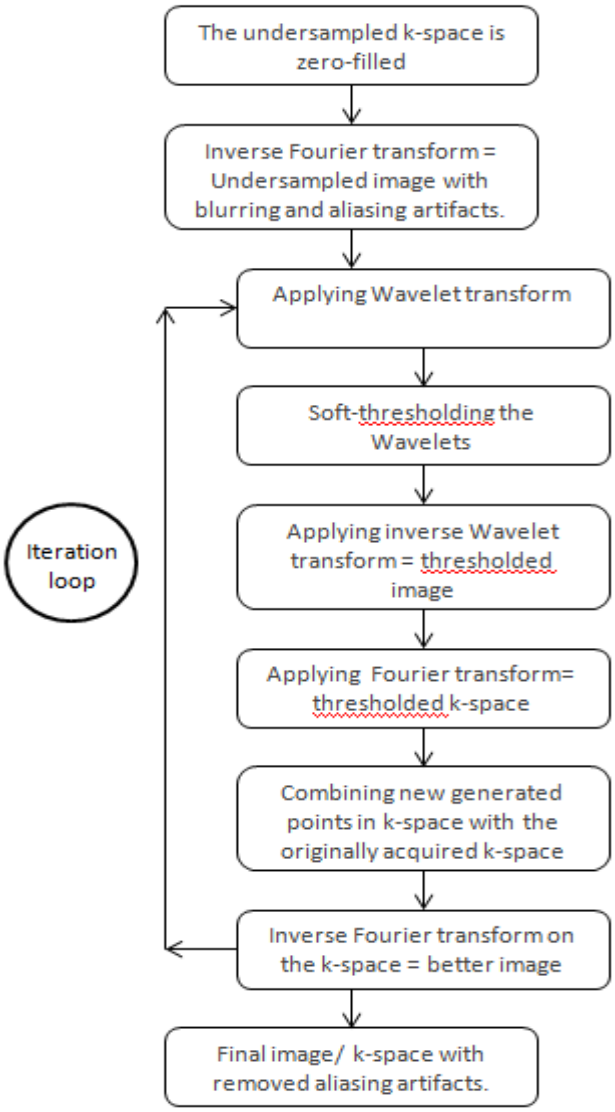

Figure 4.34, The flowchart showing the iteration loop of CS reconstruction. The soft-thresholding loop can be substituted with any other algorithm as a solution for the regularization problem.

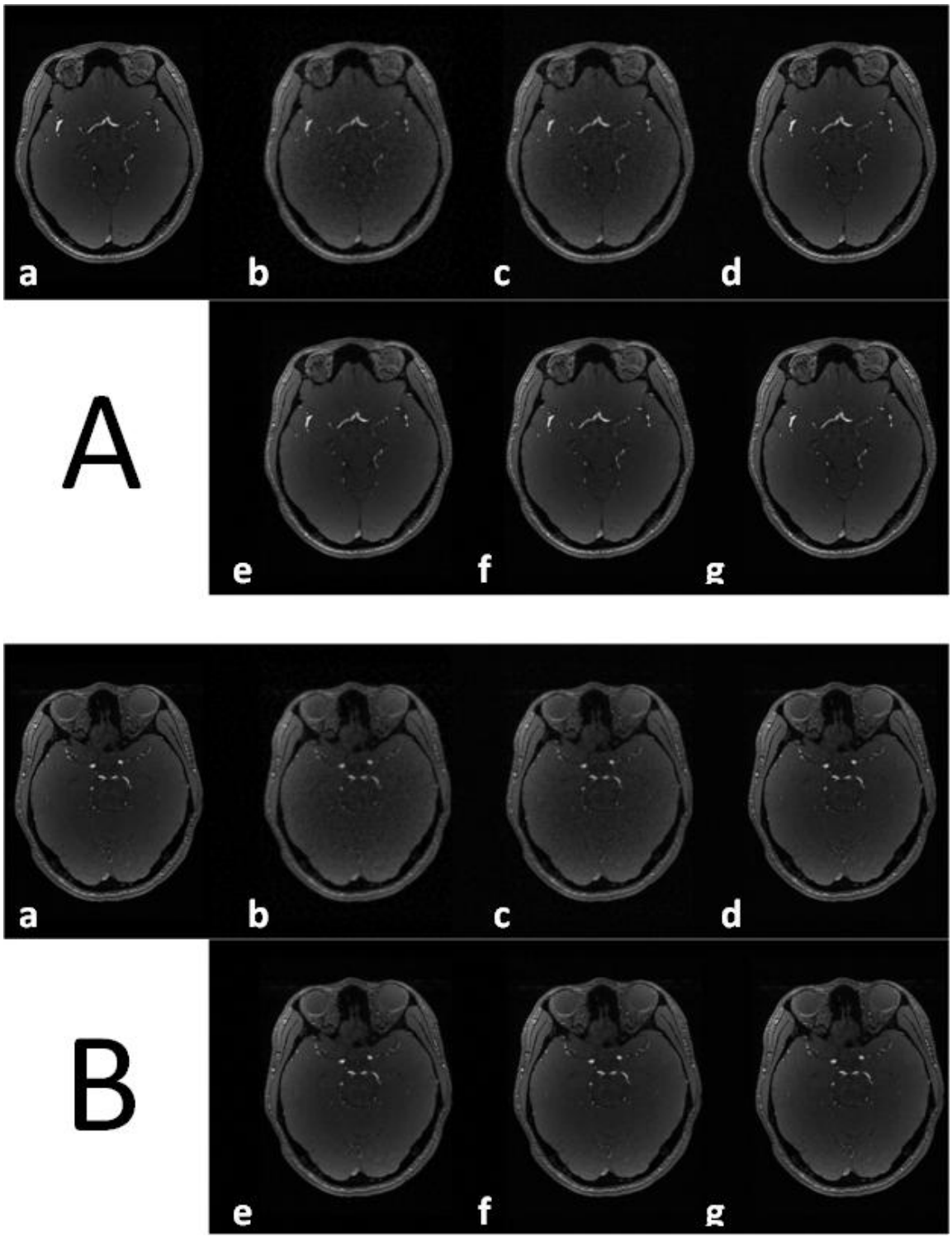

Figure 4.35, (A & B) showing two example slices, through iterations of the CS reconstruction for a 20% undersampling scheme. (a) The original fully sampled image, (b) zero-filled, (c-g) iteration 1~5 respectively.

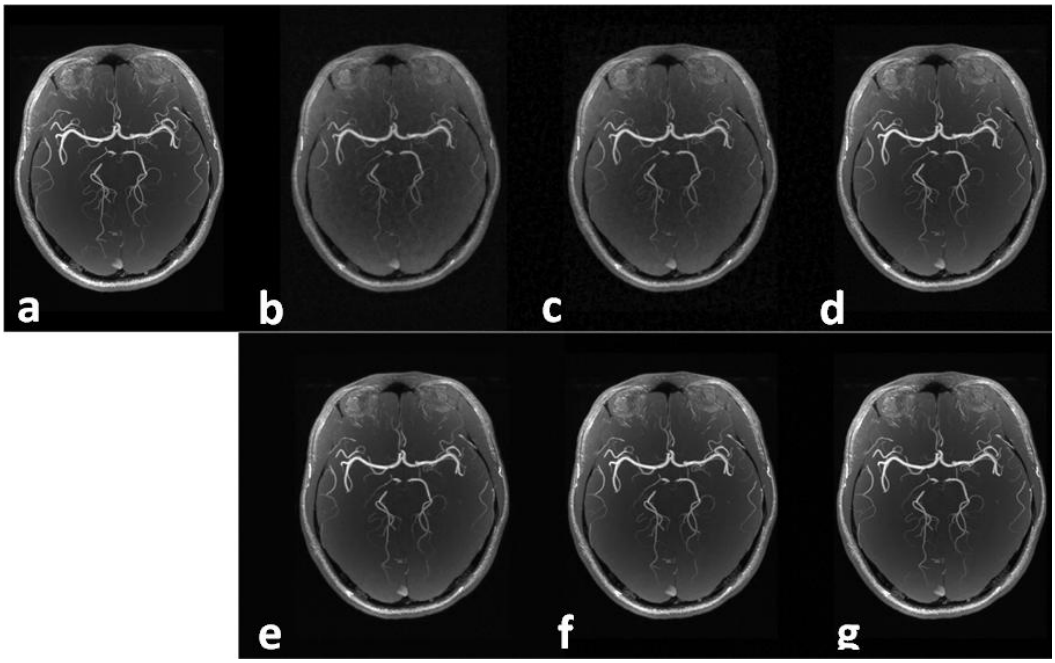

Figure 4.36, MIP images comparison through iterations of the CS reconstruction for a 20% undersampling scheme. (a) The original fully sampled image, (b) zero-filled, (c-g) iteration 1~5 respectively.

Figure 4.37 shows the comparison of the final CS reconstructed images from 20, 30 and 50% undersampling schemes and their corresponding fully sampled images.

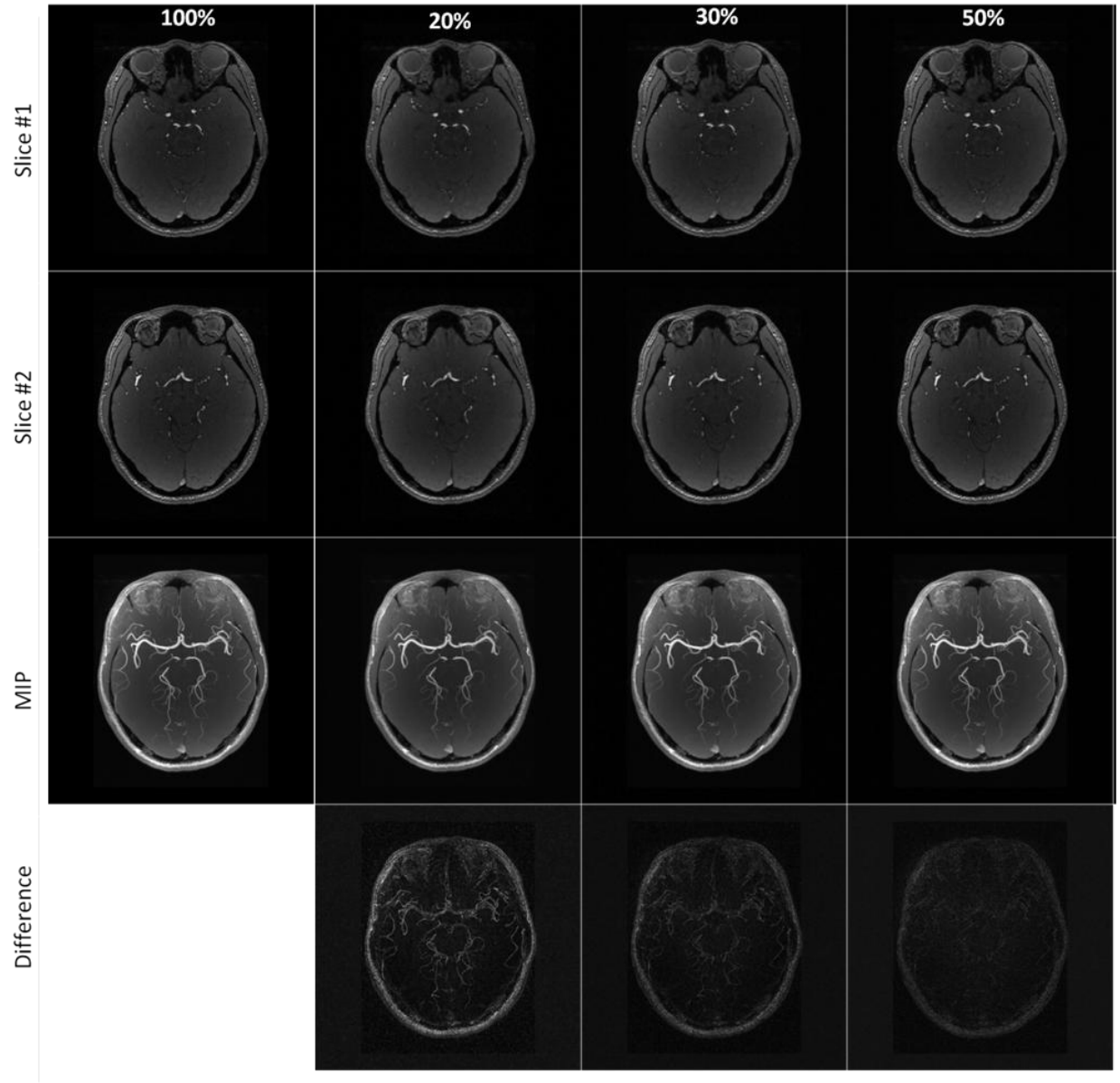

Figure 4.37, comparison of CS reconstructed images from undersampling schemes of 20, 30, 50% and the fully sampled image. From up to down: the first two rows are two examples slices and the third row is the MIP comparison. The fourth row shows the difference image of the CS reconstruction and the fully sampled MIP images.

- Vessel recovery performance

The CS reconstruction performance in recovering the vessels can be evaluated by comparing a common cross section profile of a vessel in CS reconstructed images with the same profile of the fully sampled images. Here we drew a profile crossing two adjacent vessels with different sizes (one big and the other medium) and compared signal intensity of the same profile for fully sampled data with the 20, 30 and 50% undersampled CS reconstructed MIP images (Figure 4.38). As can be seen in the profiles, the widths and amplitudes remain constant except for the 20% profile which shows a slight loss of amplitude and width. The loss of amplitudes can be understood in terms of the reduced coverage of k-space and the inability of the CS reconstruction to recover this lost information. Since the size of the vessel is deterministic in choosing the compensation factor, perfect recovery of the lost energy in k-space is not feasible unless an *a priori* information is available regarding the object. The reduced width can be understood as a narrowing of the vessel caused by the soft-thresholding step of the CS reconstruction. This is one of the pitfalls of the soft-thresholding algorithm we implemented for CS reconstruction and can be more problematic in the presence of excessive white noise.

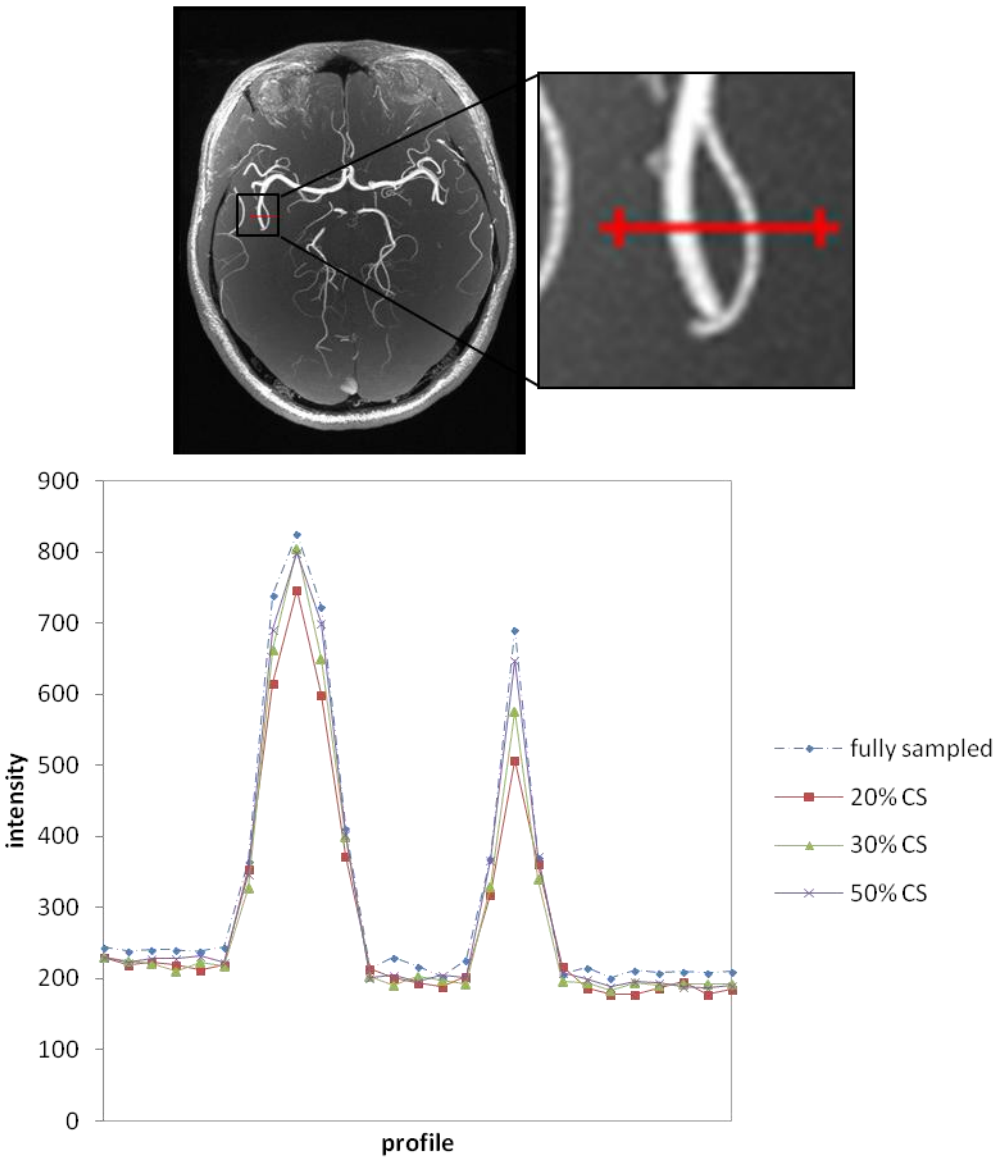

Figure 4.38, Cross section profile of two vessels compared between fully sampled MIP image, and 20, 30 and 50% undersampled CS reconstructed MIP image.

4.6 Discussion

4.6.1 Computation cost

Almost every algorithm which has been developed for solving the CS reconstruction regularization problem has an iterative nature. The aforementioned problem is usually underdetermined and ill-posed. Overall, these methods are computationally more complex than solving linear reconstruction methods. The method used in this thesis, although very basic and simple, still takes approximately three minutes in MATLAB to reconstruct a 512x512x30 angiogram with 5 fold acceleration factor. More sophisticated methods may take as much as 5 times longer than the basic algorithm.

Beside the possibilities of code optimization in favor of accelerating these reconstruction times, other feasible methods such as implementing the code to run on a Graphical Processing Unit (GPU) can improve the processing time significantly [42].

4.6.2 Comparison with low resolution imaging

Reducing the number of encoding lines in any way will lead to a faster scan time. A simple solution would be to reduce the resolution of the image by reducing the k-space matrix size or in other words truncating the k-space signal. This way we don't need to worry about the Nyquist sampling criterion since we are not changing the sampling rate by reducing the matrix size. However, by truncating the Fourier series we lose high spatial frequency information which leads to an increased Gibbs Ringing artifact and blurring. We refer to this way of undersampling for saving time as the low-resolution approach. Here we compare the reconstructed images from the extreme case of only 20% variable random undersampling scheme with the ones from the

20% low-resolution approach. The idea is to keep the scan time the same by fixing the total number of encodings in both approaches. Figure 4.39 shows the zero-filled reconstruction of the MRA example for both approaches.

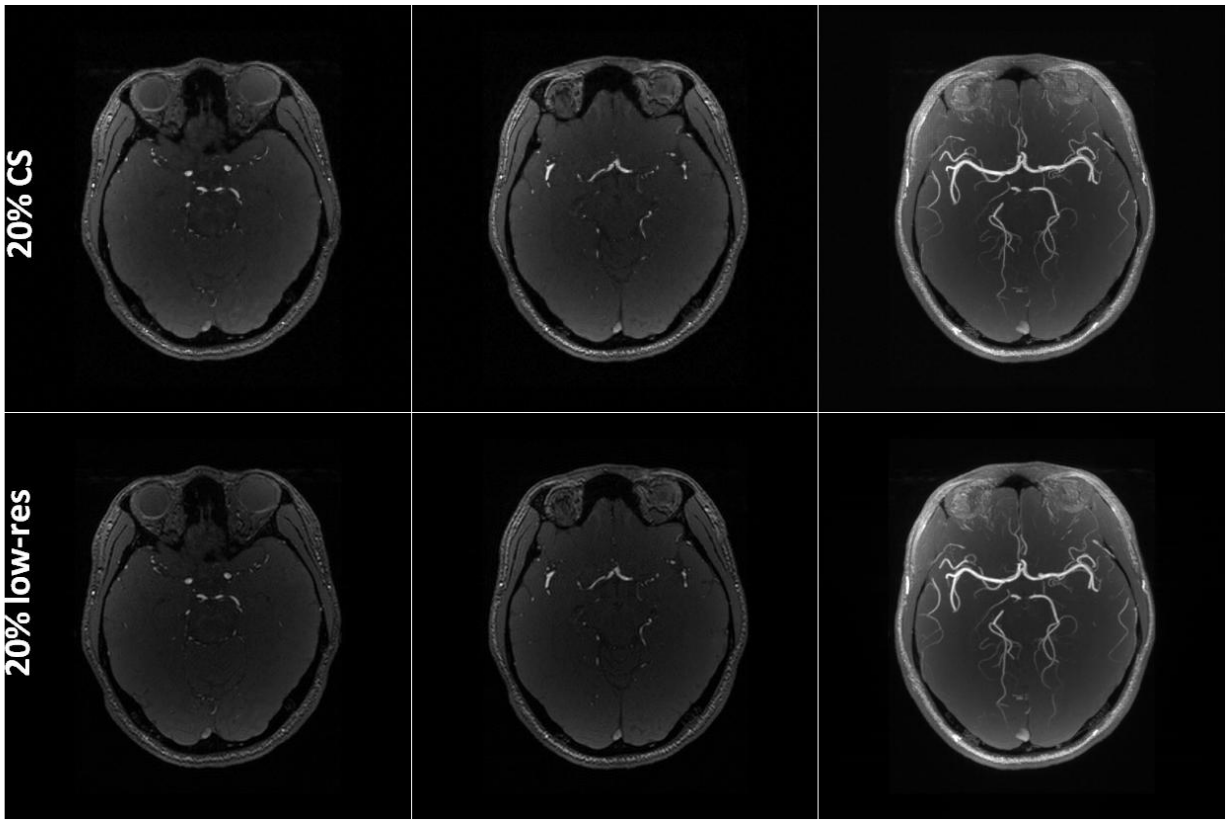

Figure 4.39, comparison of 20% variable density random sampling with CS reconstruction (top row) and 20% low-resolution sampling scheme with zero-filling reconstruction (bottom row). Comparison is made for two individual slices (on left) and the MIPs (on right). The results from the two methods are almost identical with some Gibbs Ringing present on the low-resolution single slice images. The original matrix size of these images is quite big (512x512), the 20% low-resolution scheme is still a relatively big matrix as well (~229x229). Which is why the low-res images are still pretty good images even with zero-filling.

The original matrix size of these images is quite large (512x512), therefore the 20% low-resolution scheme is still a relatively big matrix (~229x229), which is why the low-resolution images are acceptable even with zero-filling. To show the potential differences of these two

sampling schemes, we truncate the original k-space to a 256x256 matrix size. Then we apply a 20% variable density undersampling along with a 20% low-resolution sampling (~115x115) to the new matrix, and compare the corresponding reconstructed images (Figure 4.40). Note that the low-resolution matrix is zero filled and reconstructed while the variable density random sampled matrix is reconstructed via CS reconstruction.

As expected the Gibbs ringing is now more prominent in the low-resolution image. On the other hand the 20% CS reconstruction does not show Gibbs Ringing of any kind and the vessel definition is sharper than the low-resolution images. Nevertheless, there are still small vessels that are not visible with the random sampling scheme, primarily because of the loss of energy in these structures due to the missing k-space information. Even the CS reconstruction fails to recover all the missing high spatial frequency k-space information.

To be fair, if a more sophisticated regularization algorithm[34] were used in order to reconstruct the 20% variable density undersampled acquisition, we might have been able to recover the k-space with more precision. Also designing the variable random sampling scheme optimally can be crucial in increasing the chances for exact recovery. On the other hand using a data extrapolation method [6] to recover the missing outer k-space information in the low-resolution matrix can potentially enhance the results. However the comparison made here is only to show the advantages of CS over low-resolution imaging.

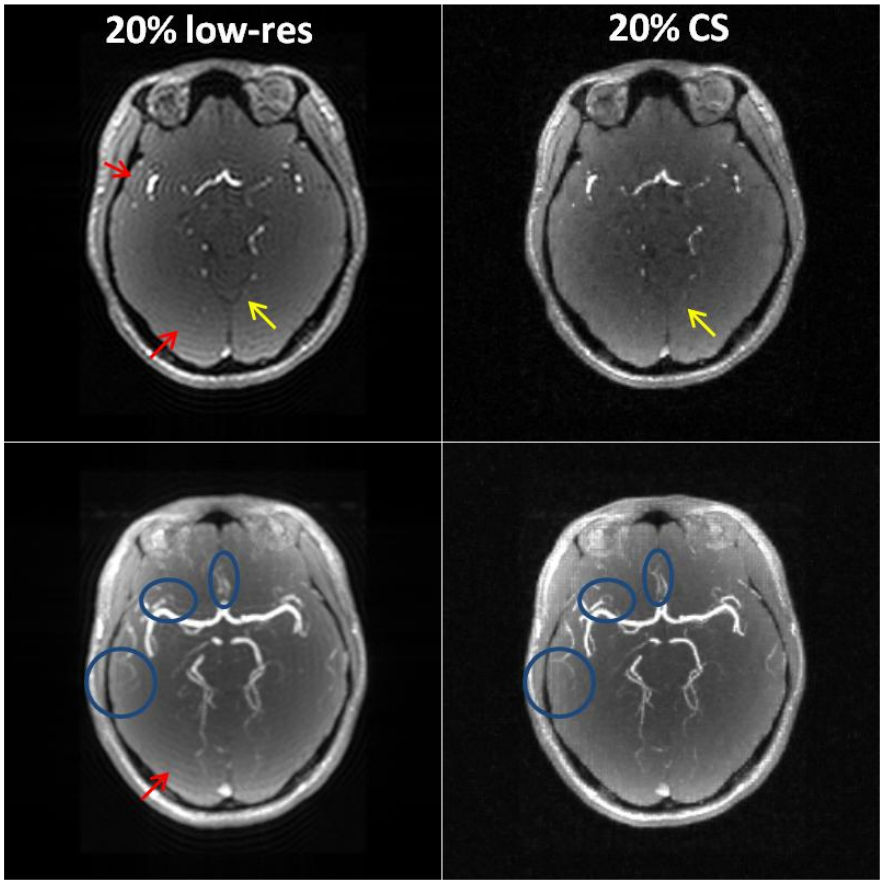

Figure 4.40, , comparison of the artifacts in: 20% low-resolution sampling scheme with zero-filling reconstruction and 20% variable density random sampling with CS reconstruction. The red arrows show the Gibbs Ringing artifact in the low-resolution scheme. The yellow arrow shows the structural detail missing in the CS method. The blue circles show the better vessel definition in the CS method compared with the low-resolution scheme.

The difference images shown in Figure 4.41, indicate that both approaches lose a considerable amount of image information due to undersampling compared with the fully sampled images. The difference in the low-resolution results is more prominent compared with the CS approach due to the intrinsic higher SNR of the low-resolution reconstruction. The remnant difference of the already recovered structures (such as the middle cerebral arteries) in the CS approach is partly due to an incomplete compensation for the energy loss of the signal

due to undersampling. This will create an offset in the signal amplitude of the reconstructed images.

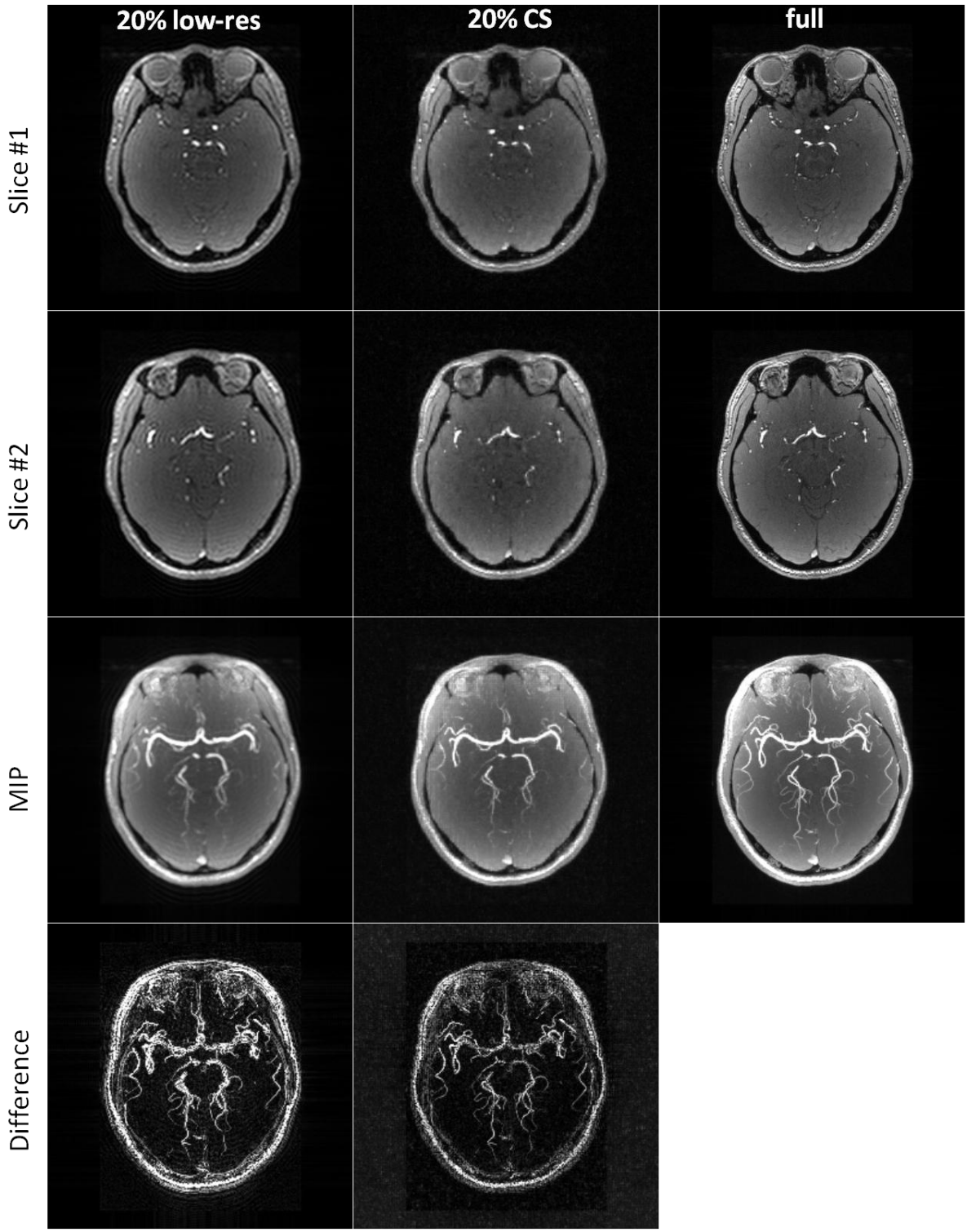

Figure 4.41, comparison of, 20% low-resolution sampling scheme with zero-filling reconstruction, 20% variable density random sampling with CS reconstruction and fully sampled images. The bottom row shows the difference image of the MIPs, comparing the low-resolution approach to the CS reconstruction.

4.6.3 CS artifacts

The CS reconstruction tends to shrink the magnitude of the reconstructed sparse coefficients. This shrinkage can sometimes lead to disappearance of an originally small image coefficient. The image contrast plays an important role in the ability to vastly undersample the k-space and still be able to recover the image using CS reconstruction. The higher the image contrast, the sparser the image coefficients and easier to recover. Therefore, with an increased undersampling factor, the most common artifacts in CS reconstruction are not the usual loss of resolution or increase in aliasing interference, rather loss of low-contrast features in the image. This is why CS in predominantly viable in applications where high resolution high contrast features are required and present, and reducing the scan time is very important.

4.7 Conclusion

In this chapter we demonstrated the theory of CS and how it can be applied to MRI with the goal of faster imaging. We compared reconstructions with different undersampling schemes and proved the strength of random undersampling compared with uniform undersampling. The algorithm introduced here for CS reconstruction is a simple and basic one and there is room for improving the results using a more sophisticated regularization. This however might increase the reconstruction time which is not desirable in clinical applications.

Other data extrapolation methods use *a priori* information provided via defining a model either for the object being imaged or the signal behavior in k-space in order to estimate the missing k-space information [6]. These models are usually very basic and primitive in their definition, compromising the complexity of the actual object (or signal). This will lead to false or

biased estimations of the missing k-space points in cases where the model is not able to describe the object (or signal) perfectly. Whereas in CS the equivalent of the *a priori* information is simply a transform of the initial estimated image (e.g. wavelet transform) and there is no need for defining a model. This removes any possible biased data recovery due to the absence of a comprehensive model.

In conclusion, CS is a viable fast MR imaging technique which can be implemented easily in conventional MRI sequences. The reconstruction algorithm introduced here, needs to be improved to ensure the recovered image provides better quality and more accurate clinical information compared with a simple low-resolution acquisition of the same scan time. In this regard, a simulated clinical marker such as a narrowed artery would be useful in determining the performance of CS in resolving the stenosis and more importantly avoiding false positives.

CHAPTER 5: JOINT ACQUISITION

5.1 Introduction:

High resolution anatomical imaging for quantitative parameter mapping (such as T1 and T2) is of interest in a wide range of clinical applications such as oncology and neurology. The major concern in MR parameter mapping techniques is usually the long scan time due to the need for multiple data points and high resolution, making these acquisitions clinically impractical. Sacrificing the number of data points in order to save time can lead to less accurate estimations of the parameters of interest and may impose limitations especially when analyzing multi-compartmental signal behavior [43, 44].

Data undersampling is an attractive strategy to reduce the scan time in such situations. However depending on the chosen undersampling scheme, the resulting artifacts (such as aliasing, Gibbs ringing and blurring) may limit the utility of the reconstructed images unless they are removed or the missing data is appropriately estimated. Reasonable estimates of the missing data can be accomplished by parallel imaging for instance, a widely used undersampling strategy for scan acceleration. Parallel imaging utilizes the spatial sensitivity profiles of a multichannel receiver coil array to interpolate the missing data in k-space. However, intrinsic SNR penalties associated with parallel imaging and its inherent noise amplifications and high spatial frequency aliasing artifacts may limit their use in quantitative parameter mapping imaging even at low accelerating factors [45]. Among other undersampling methods, It has been shown that compressed sensing (CS) can also be applied in MR parameter mapping to accelerate the scan time [46]. In CS, the k-space data is randomly undersampled which leads to incoherent aliasing

artifacts. These artifacts appear like noise in a sparse representation of the image and can be reduced in the process of recovering the underlying image coefficients. However the considerably long reconstruction time required in CS, can be a limiting factor for clinical applications.

Keyhole imaging and view sharing are two other techniques which have been shown to be useful in reducing the scan time and increasing the temporal resolution [47-55]. Here we introduce a new approach which is a combination of the idea of random undersampling in CS, *keyhole imaging* and *view sharing* for quantitative MR parameter mapping acceleration. We use multi-echo spin echo (MSE) T2 mapping as a means to test this new concept.

5.2 Theory:

The idea of keyhole imaging and view sharing techniques are essentially similar in their intrinsic objective of sharing the k-space information between different images in a multi data point acquisition. The central k-space information determines the overall low spatial frequency contrast of the image while the outer k-space defines the details of the image (high spatial frequency component).

5.2.1 Keyhole imaging:

Keyhole imaging was introduced in 1993 by Vaals and Jones in two papers independently [56, 57] with the same goal of increasing the temporal resolution in high spatial resolution dynamic MR imaging. In dynamic imaging, the tissue of interest is imaged in a consecutive sequence of images (frames or updates) along time in order to resolve a dynamic change in the signal. One immediate application of the Keyhole imaging is in time-resolved contrast enhanced

MR angiography (CE-MRA), where high temporal resolution is desired for resolving the evolution of the contrast agent in the tissue of interest [47]. The important assumption in Keyhole imaging is that low spatial frequency information (central k-space) is sufficient for studying dynamic signal changes. Later on It was shown that the method could be applied in numerous other applications [53] such as MR mammography, interventional MR imaging [50], functional imaging and temperature monitoring of therapeutic hyperthermia.

The method of Keyhole imaging is based on collecting a reference image with the desired high spatial resolution via collecting a large k-space matrix. The update images (frames) on the other hand will be collected only for the central part of the k-space with a low spatial resolution. The outer k-space (high spatial frequency) information of the reference image is then used in reconstruction steps to improve the spatial resolution of the subsequent frames. In other words, the missing outer k-space information in the update images (frames) are filled with the corresponding data from the reference image k-space matrix creating a fully sampled *composite k-space* (Figure 5.1). This way, the reconstructed frames will effectively have the same high spatial resolution of the reference image, but can be acquired in much less scan time. The assumption is that the dynamic signal information will be preserved since they have low-spatial frequency nature and the central k-space is collected for all of the frames. If the signal changes are predominantly high spatial frequency in their nature, the Keyhole method may not be able to recover that information since their corresponding k-space data is not updated in each frame. Therefore the central part of k-space would have to be increased, reducing the utility impact of the keyhole method.

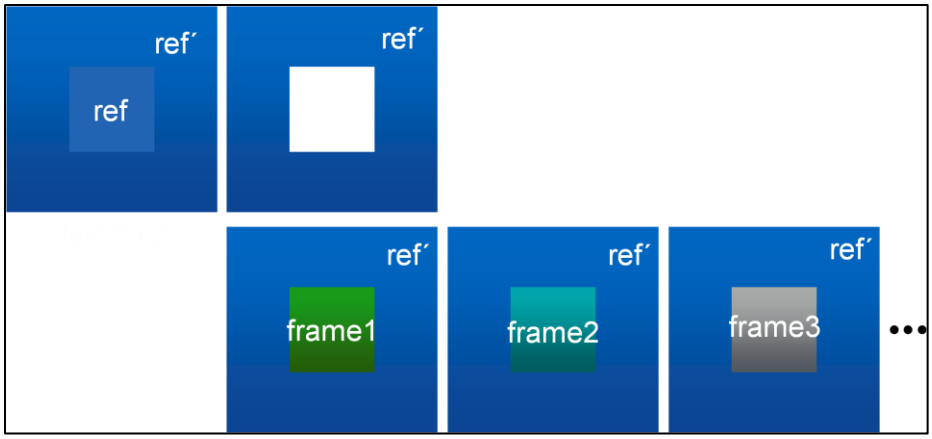

Figure 5.1, Schematic of keyhole imaging; the reference image is collected with full resolution in large k-space matrix size. The consecutive frames are only collected for the central block of k-space for high temporal resolution. The outer k-space information for all the frames is borrowed from the reference image (ref') In order to increase their effective spatial resolution.

One of the pitfalls in the Keyhole technique is the potential inconsistency between the reference outer k-space data and the updated central k-space data. This might happen because of motion between different frames and local field variations due to susceptibility effects or changes in contrast. All these can lead to not only Gibbs ringing artifacts but also simply incorrect or inappropriate information being added to the outer k-space data [53].

5.2.2 View sharing technique

View sharing is similar to keyhole imaging in sharing the assumption that k-space information is redundant in dynamic imaging and therefore can be shared between different frames. The difference however is that in view-sharing the k-space in divided into multiple blocks and the central k-space is collected more frequently than the higher order k-space blocks. Therefore the temporal resolution of the acquisition can be increased. In the reconstruction steps, the missing k-space segments in each frame are filled with those from the closest neighboring frames. The acquisition schemes, the size and number of k-space blocks, the data

combination and data reconstruction can be modified according to the desired application. As an example, consider a 3D k-space divided into four blocks and labeled as shown in Figure 5.2.

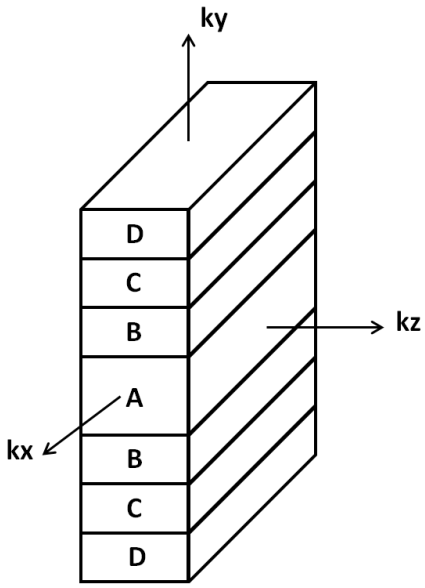

Figure 5.2, The schematic showing k-space divide into 4 blocks labeled A, B, C and D, going outward in k-space. Here the division of k-space is done along the ky (phase encoding) direction. The kz (slice encoding) direction can be divided into blocks as well.

One possible acquisition scheme would be to collect k-space blocks consecutively with the following order: A, B, A, C, A, D, and then repeat this order as demonstrated in Figure 5.3. In addition, before the beginning of this cycle, a fully sampled k-space can be acquired (as a reference dataset) to help reconstruct the first few frames. Each frame then can be reconstructed by combining k-space blocks from the neighboring time points. In other words, for each frame the missing k-space blocks can be estimated by substituting the closest match block or by interpolating between the closest neighboring blocks either linearly or exponentially [47].

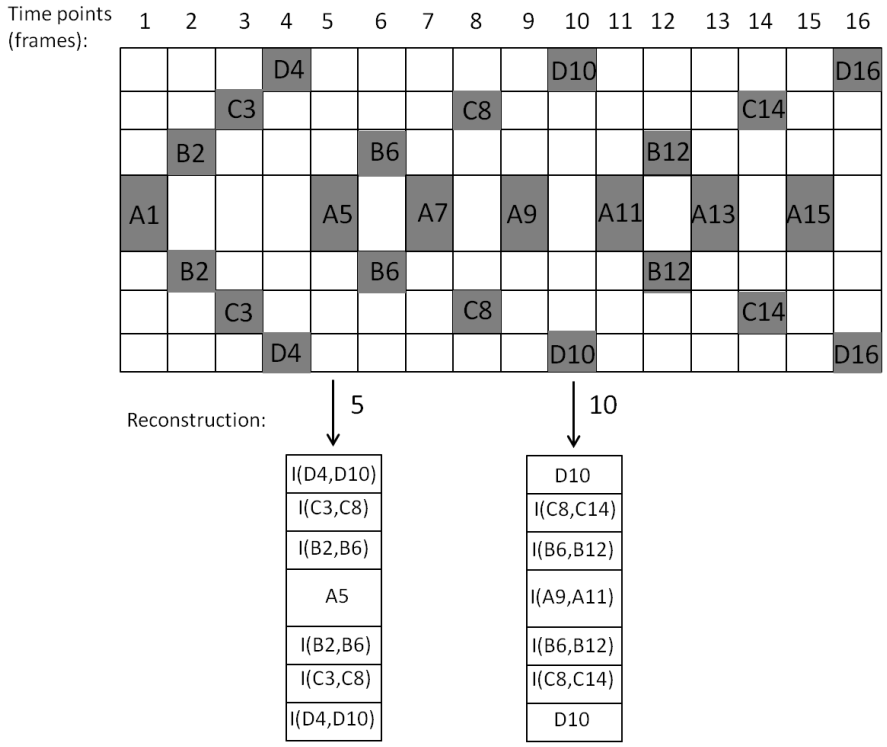

Figure 5.3, One example of how a view-sharing acquisition could be designed like. The order of collecting k-space blocks is depicted in the schematic figure. Reconstructing each frame is possible by combining k-space blocks from the neighboring time points. For each time point (frame) the missing k-space blocks can be estimated by linearly interpolating (in time) between the closest neighboring blocks which were acquired. I() denotes an interpolation operator.

5.2.3 Enhanced view sharing (view-sharing+) for parameter mapping

For the purpose of parameter mapping the signal evolution along the time points is deterministic in designing the acquisition scheme. In the case of MSE T2 mapping for example, the signal evolution along the echo train is an exponential decay. This dynamic signal usually has a dominant low spatial frequency nature. Therefore we manage to preserve the low-spatial frequency information in k-space by making sure that the central blocks are acquired for each and every frame (echo). This feature is inherited from the concept of keyhole imaging. Figure 5.4 demonstrates the modified view sharing acquisition scheme. In order to prevent confusion, we

are calling this combined method of view sharing and keyhole imaging, the *"view-sharing+"* throughout this thesis.

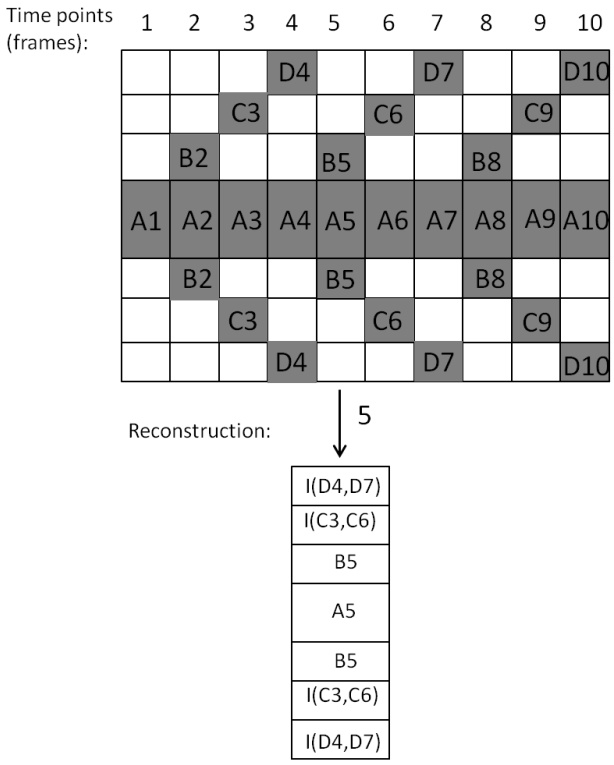

Figure 5.4, Modified view sharing acquisition scheme for collecting a multi spin echo T2 mapping imaging. The central k-space block is acquired for every time point (echo). The missing outer k-space blocks are shared by interpolating between the closest neighboring acquired blocks.

The combination process for each frame can be more simplified by not interpolating higher order k-space blocks either and sufficing to choose the nearest neighboring frame and fill the missing blocks accordingly. For example the same fifth time point in the acquisition scheme depicted in Figure 5.4, can be reconstructed with the following combination: (D4, D6, B5, A5, B5, C6, D4).

5.2.4 k-space inconsistencies

In applications where the view-sharing+ is feasible, the finer details of the image which are stored in the outer k-space are assumed to be essentially identical between the neighboring frames. On the other hand collecting the central k-space for every frame is a limiting factor for increasing the imaging frame rate (temporal resolution). Therefore, In order to decrease the scan time even further, we tend to make the central k-space block smaller. Considering the scheme shown in Figure 5.4 with the central k-space block (A) and the outer k-space divided into three blocks (B, C, D), the time saving factor (τ) can be calculated as follows.

$$\tau = \frac{2\alpha+1}{3} \quad (5\text{-}1)$$

where α is the ratio of the size of the central block (A) relative to the size of the k-space matrix thus, the smaller the central k-space block, the faster the scan. This is critical since by making the central k-space block smaller, the outer k-space blocks will cover some of the low-spatial frequency information which is not necessarily identical from one frame to the other. If we fail to resolve these k-space blocks via sharing, we are likely to experience Gibbs ringing-like and ghosting-like artifacts. This is easily apparent especially in cases where the images of neighboring frames have significantly different signal and contrast. For instance a MSE scan with relatively large echo spacing. We will demonstrate this phenomenon later in the Results section.

5.2.5 Joint acquisition

We propose using a CS like sampling approach in view-sharing+ acquisition with randomly sampled outer k-space rather than the common block design of k-space discussed earlier. The problem with the shared k-space inconsistencies and resultant artifacts can be eased with the idea of random undersampling. We can relate the same incoherency phenomenon of

aliasing artifacts in images with randomly undersampled k-spaces in CS, to the incoherent Gibbs ringing or ghosting like artifacts in the images from randomly view-shared k-spaces.

Consider a k-space with an in-plane matrix size of 256x256 assuming the same acquisition scheme in Figure 5.4, where each three neighboring frames share their outer k-space information. In this case we can extend the scheme to a 3D acquisition by undersampling the k-space in both phase and partition encoding directions. We create three complementing sampling schemes in ky-kz plane where they have the central 64x64 block fully sampled (accounting for almost 6% of the k-space) and the outer k-space (the 94% rest of k-space) is randomly but uniformly undersampled by a factor of three. The schemes are designed in a way that their outer k-space randomly collected samples do not overlap with each other. In other words, putting all the data from the three undersampled neighboring frames together will create a fully sampled k-space. A schematic of the k-space schemes and their combination can be seen in Figure 5.8. We refer to this sampling scheme as the "*joint acquisition".*

5.3 Results

In order to demonstrate the joint acquisition concept, we will apply the methods mentioned above to a MSE imaging experiment with the goal of decreasing the scan time while preserving the quality of the reconstructed image. The performance of the algorithm will be demonstrated by comparing the T2 maps created from the images with fully sampled k-space, view-sharing+ and the joint acquisition approach. All the simulations were done in MATLAB (The Mathworks Inc.).

5.3.1 Data collection

We scanned a healthy volunteer in a 3T Siemens Verio scanner using a 32 channel head RF coil, using the MSE sequence. The imaging parameters were as follows: matrix size=256x256, resolution=1x1x4 mm^3, FA=180°, TR=1000ms, TE=8.8-281.6ms with ΔTE=8.8ms (32 spin echoes) and a total imaging time of 256 seconds. We only collected a single 2D slice for the purpose of simulations; however our method can be readily applied to a 3D dataset. Figure 5.5 shows three examples of fully sampled magnitude images from three echoes, one at the beginning of the echo train, one at the middle and one at the end, showing the different contrast dynamics throughout the echo train.

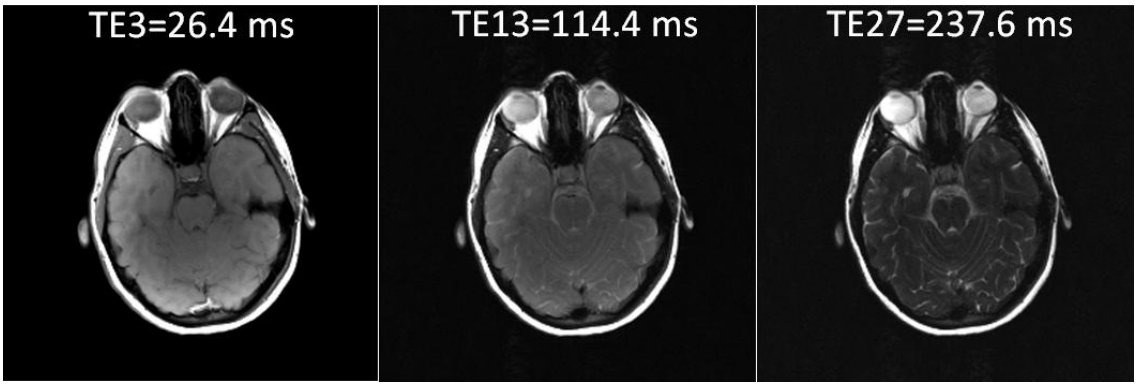

Figure 5.5, Three example echo magnitude fully sampled image. The third echo in the 32 echo train (TE3=26.4 ms), the 13th (TE13=114.4 ms) and the 27th (TE27=237.6). The T2 signal evolution can be seen along the echo train.

The T2-weighted signal evolution of all the 32 echoes can be plotted for a homogenous area in the image along the echo train (Figure 5.6). The T2-weighted exponential decay can be seen in the signal evolution. The first echo is an outsider in the exponential decay curve which is due to the fact that it takes some time for the echo train to reach steady state. Therefore we do not use this echo in our simulations to avoid T2 estimation errors.

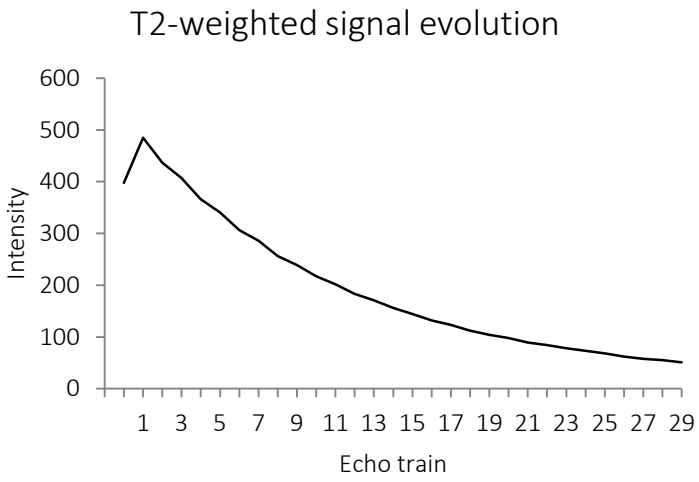

Figure 5.6, The T2-weighted signal evolution along the echo train showing the exponential T2 decay for the signal of a homogenous area on the image.

5.3.2 Sampling schemes

We performed the simulations with two sampling strategies: view-sharing+ and joint acquisition. Three separate sampling schemes were created with a 256x256 matrix size, where a central k-space block is always fully sampled for both strategies and the outer k-space is divided into three complementing parts accordingly. The imaging scheme is the same as it was shown in Figure 5.4. The composite k-space for each echo (frame) is created by combining the outer k-space information from the neighboring echoes while preserving all the acquired blocks.

The view-sharing+ sampling scheme has the central 64 phase encoding lines fully sampled and the outer k-space is divided into three blocks each covering 32 lines on either side of the k-space. The time saving factor according to the equation (5-2) is 0.5 which means by employing this scheme we can shorten the scan time by a factor of two.

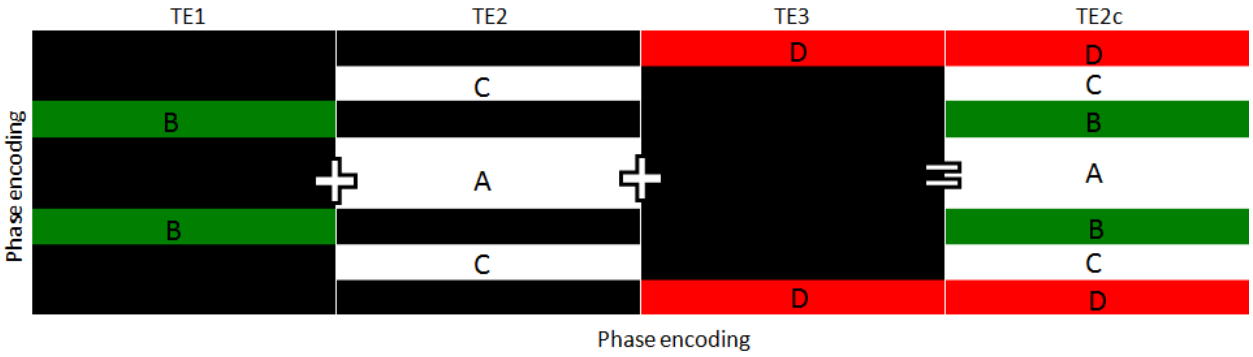

Figure 5.7, The view-sharing+ k-space schemes for a 256x256 in-plane matrix size for three consecutive echoes with the central 64 phase encoding lines (A) fully sampled and the outer k-space divided into three segments (B, C and D) which each cover 32 phase encoding lines on each side of k-space. The resulting composite k-space (TE2c) with the shared outer k-space blocks from its neighboring echoes (TE1 and TE3) and the central k-space from the TE2 itself.

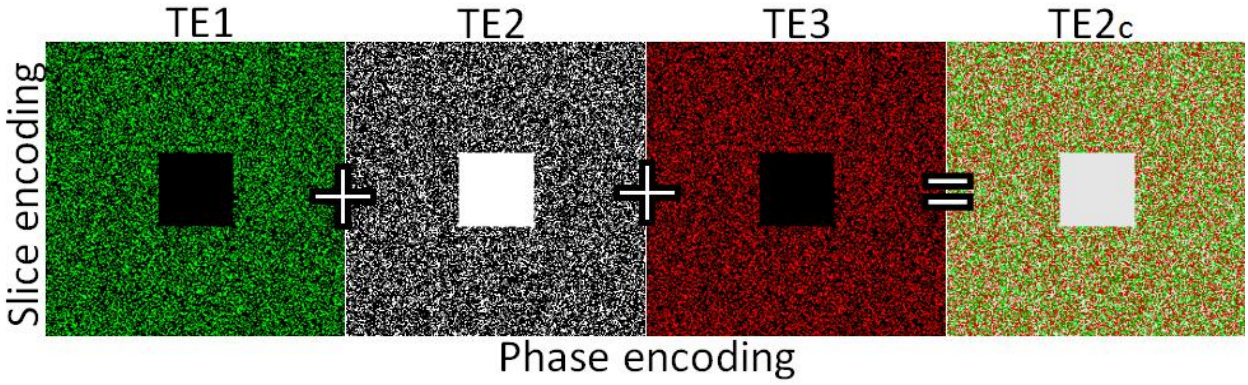

Figure 5.8, The joint acquisition k-space schemes for a 256x256 ky-kz plane matrix size for three consecutive echoes with the central 64x64 block fully sampled and the outer k-space undersampled randomly and uniformly by a factor of three. The resulting composite (joint) k-space (TE2c) with the shared outer k-space samples from its neighboring echoes (TE1 and TE3) and the central k-space from the TE2 itself. The outer k-space samples do not overlap and instead complement each other.

On the other hand for the joint acquisition scheme we collect the central 64x64 k-space block fully sampled (6% of the total k-space) and the remaining outer k-space is sampled randomly only by a factor of three. Note that in the joint acquisition scheme, the k-space is undersampled in the ky-kz plane for a 3D acquisition. The time saving factor for the joint acquisition scheme is:

$$\tau = \frac{1}{16} + \frac{1}{3}\left(1 - \frac{1}{16}\right) = 0.375 \quad (5\text{-}4)$$

which means by employing the joint acquisition scheme we can shorten the scan time roughly by a factor of 2.66.

One can note that the time saving factor is not equal between the view-sharing+ approach and the joint acquisition approach. Our simulations showed that choosing such small central k-space in the view-sharing+ approach for reducing the scan time even further, could induce excessive artifacts and not lead to an acceptable reconstructed image. Therefore the joint acquisition approach has the advantage of shorter scan time in 3D imaging already.

5.3.3 Reconstruction

In order to simulate the reconstruction, we demonstrate two scenarios: (a) only reconstructing three echoes from the beginning, middle and the end of the echo train, (b) Reconstructing all the echoes (echo train length =32) by sharing the k-space between each three neighboring echoes. The reason for demonstrating the first scenario is to accentuate the artifacts due to k-space inconsistencies between images with relatively further echo times apart from each other in a MSE imaging experiment. This way we can compare the two sampling schemes (view-sharing+ and joint acquisition) easier.

5.3.3.1 (a) Reconstruction of three echoes

We chose three echoes with relatively large TE intervals: TE1=132 ms, TE2=176 ms and TE3=264 ms. We applied the undersampling schemes defined above and showed in Figure 5.7 and Figure 5.8, to the fully sampled k-space of these three echoes. In order to reduce the k-space inconsistencies due to overall signal difference between the echoes, we scaled the k-space

samples before merging them into each other. The scaling factor can be defined by calculating the average signal intensity of a homogenous area from the zero filled reconstructed images. The k-space for each echo is then normalized by this scale factor. The same images were reconstructed using the joint acquisition sampling schemes introduced in Figure 5.8 including the same scaling correction for the signal difference between frames.

The resulting images for the view-sharing+ and joint acquisition sampling schemes are demonstrated in Figure 5.9. At the first glance the view-sharing+ reconstruction results might seem pretty accurate except for some errors in estimating the edges such as in the CSF border. However a closer look at the images (Figure 5.10) reveals the Gibbs ringing and ghosting like artifacts we discussed. Luckily we did not have any major vessels crossing this slice. In that case we would experience the same artifacts around the vessels[3]. There are methods for removing these artifacts by applying a custom designed edge preserving filter throughout the image. Amartur and Haacke showed [3, 58] this technique for truncated k-space and its corresponding Gibbs ringing artifacts. A more accurate approach would essentially find the resulting PSF of such inconsistency in the k-space and resolve it by applying a filter in the k-space.

The images from the joint acquisition sampling scheme on the other hand, do not suffer from the Gibbs ringing and ghosting like artifacts. This is the advantage of random undersampling compared with the blocked design of k-space in view-sharing+ scheme. However we can still observe the false recovery of the edges (Figure 5.10). It is not surprising to have some error in the recovery of the edges. Nevertheless the edge information is stored in the high spatial frequency Fourier samples which locate in the outer k-space. Ultimately the composite

[3] We have simulated this on a multi FA acquisition, the results are omitted from the thesis

high spatial frequency information shared from the other echoes will not be completely accurate estimates of the missing k-space information. Especially in this scenario where the images have extremely different echo times.

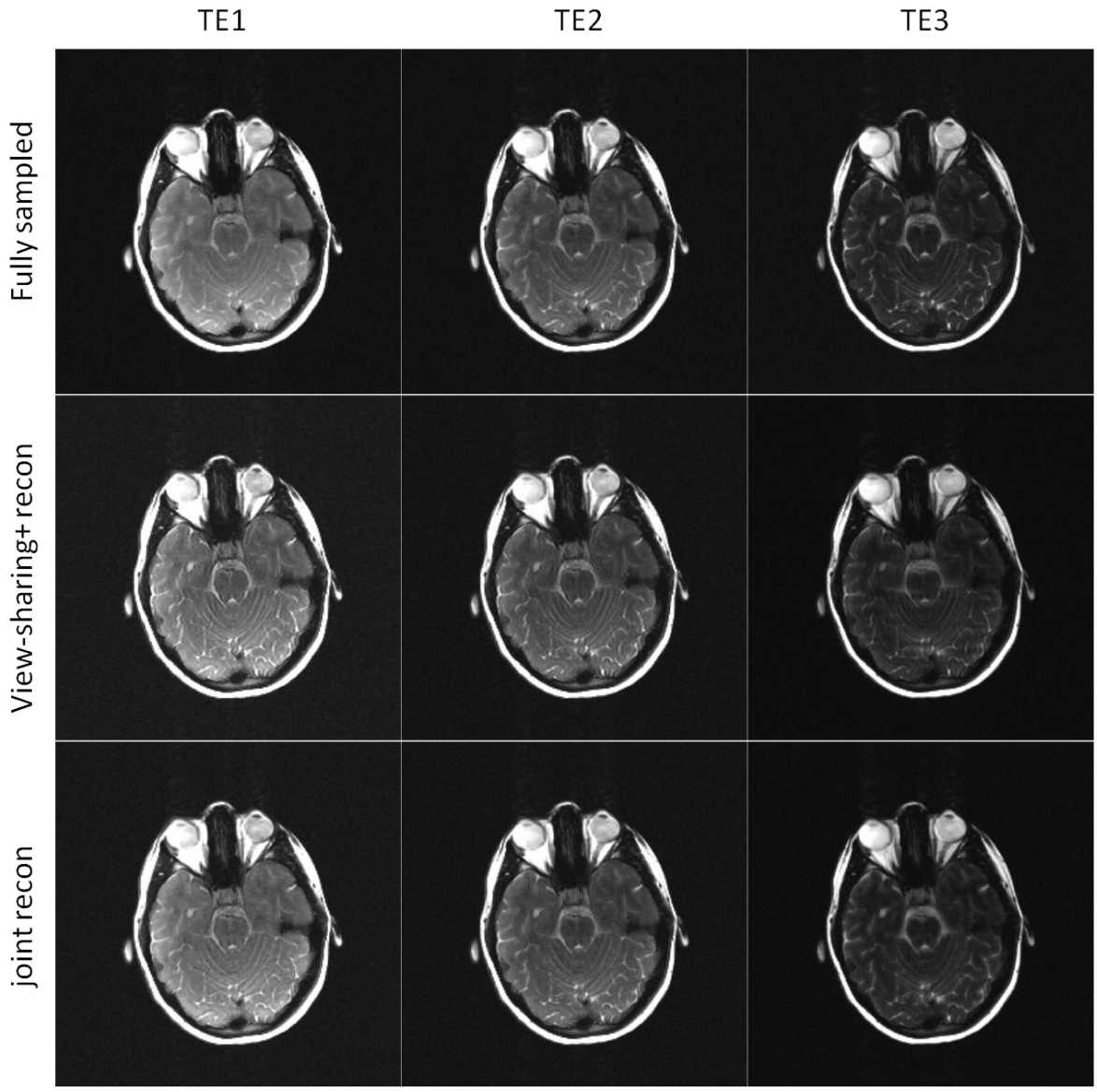

Figure 5.9, The fully sampled images of three echoes (TE1=132 ms, TE2=176 ms and TE3=264 ms) compared with view-sharing+ and joint acquisition reconstructions. At first glance they might appear similarly accurate; however there are faulty estimations in sharp edges of the images such as the CSF borders. There are also Gibbs ringing and ghosting like artifacts in the view-sharing+ results.

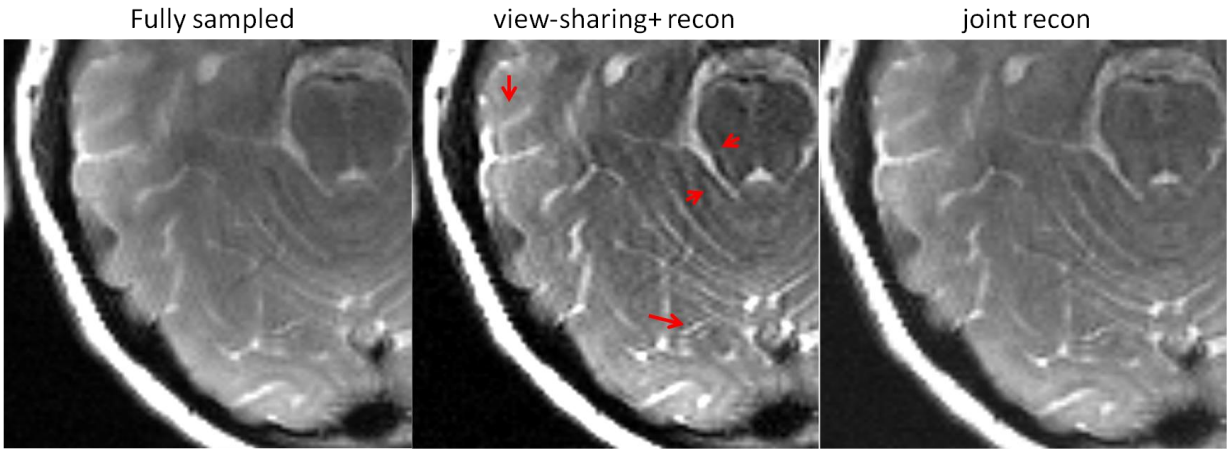

Figure 5.10, Comparison of the zoomed image of the fully sampled, view-sharing+ and joint acquisition reconstruction of TE1=132 ms. The red arrows show the Gibbs ringing and ghosting like artifacts in the view sharing reconstruction close to the sharp transitions of signal in the object. On the other hand, joint acquisition reconstruction is free of such artifacts.

5.3.3.1 (b) Reconstruction of all the echoes

In this scenario we apply the sampling schemes introduced earlier to the full echo train of the MSE imaging experiment by sharing the k-space between each three neighboring echoes. Contrary to the previous scenario, here we have a very small echo spacing ($\Delta TE = 8.8\, ms$) and thus the neighboring echoes are very close to each other in terms of their contrast and overall signal. This is an advantage for the joint reconstruction method since the k-space inconsistencies will be minimized between neighboring echoes. The resulting images for both view-sharing+ and joint acquisition schemes and their comparison with the fully sampled images are shown in Figure 5.11.

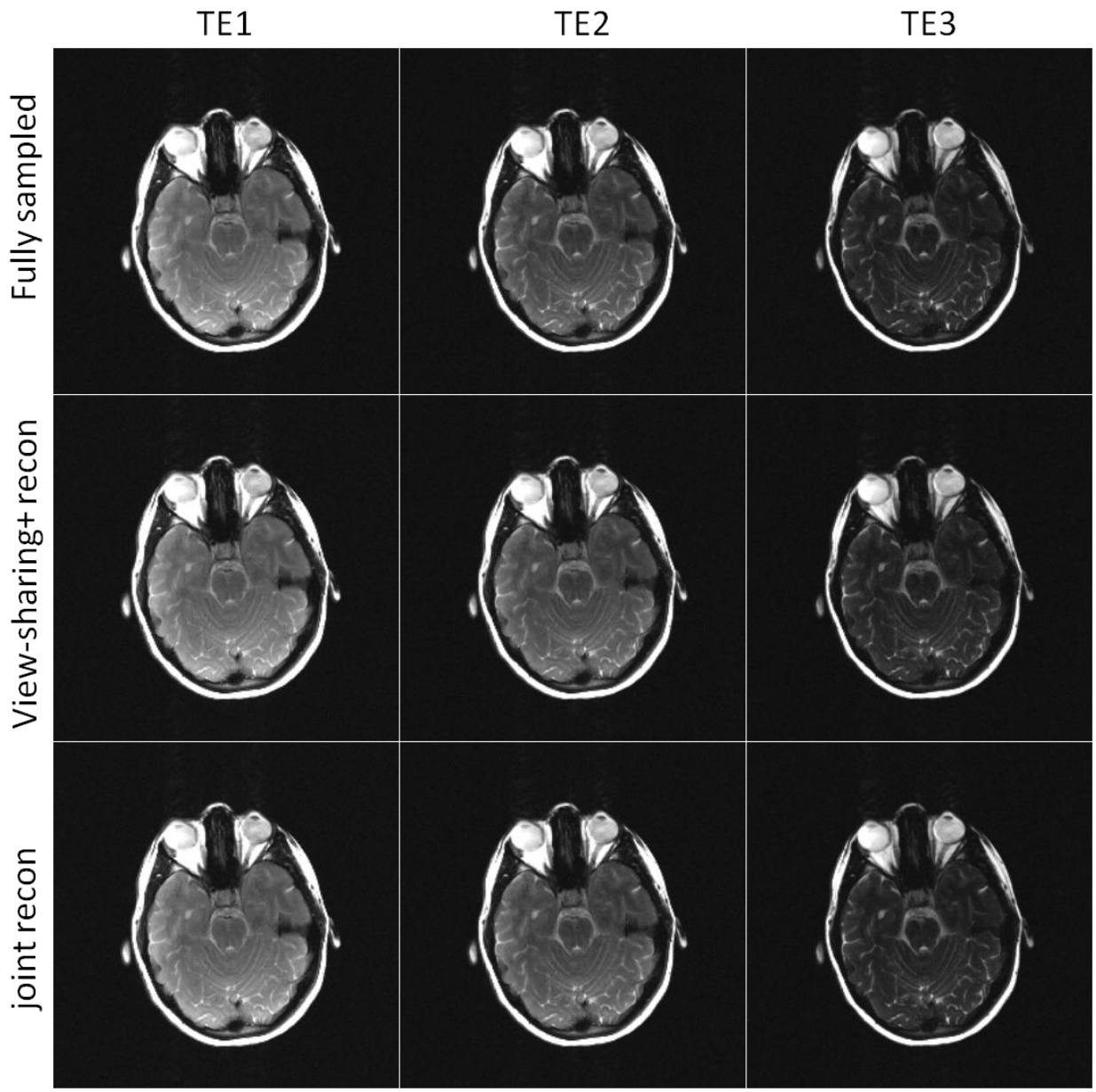

Figure 5.11, Three example echoes (TE1=132 ms, TE2=176 ms and TE3=264 ms) of the full echo train in fully sampled images compared with the view-sharing+ and joint acquisition methods. The sampling schemes were applied to the whole echo train. Surprisingly the view-sharing+ scheme performed as well as the joint acquisition scheme. Both provided almost accurate recovery of the images. This is due to small echo spacing between neighboring echoes and consequently minor signal changes between them and less k-space inconsistencies.

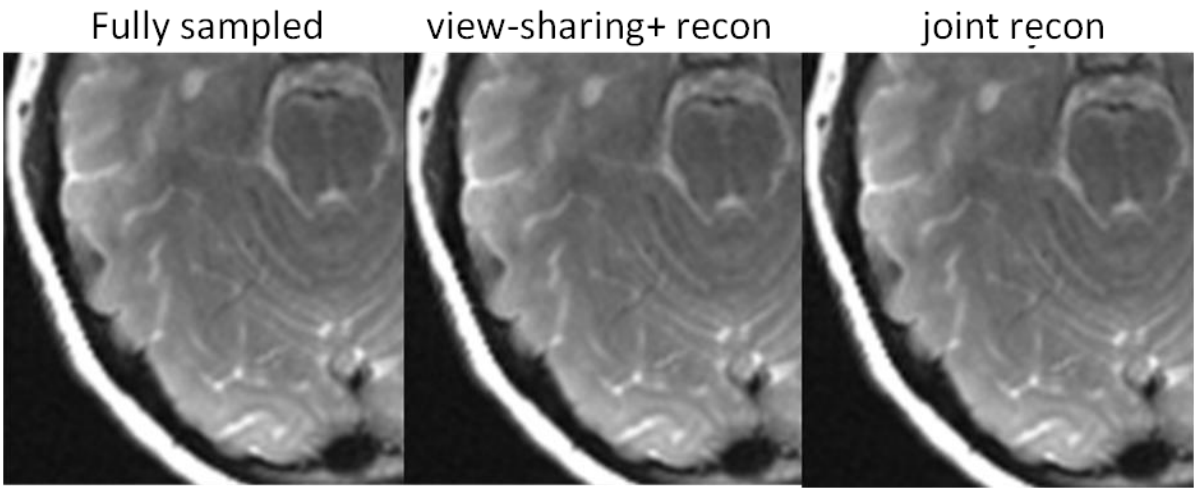

5.12, Comparison of the zoomed image of the fully sampled, view-sharing+ and joint acquisition reconstruction when applied to the full echo train. This image is from TE=132 ms. The reconstructions are far superior compared with the first scenario. There is no apparent Gibbs ringing or ghosting like artifacts.

5.3.4 T2 maps

The reconstructed images from the second scenario were used to create the pixel by pixel T2 maps via fitting the signal evolution along the echo train to an exponential decay model. The T2 maps generated from the fully sampled images are shown and compared with the one created from the view-sharing+ approach and the joint acquisition approach. Surprisingly all the maps look essentially identical. This indicates that both the view-sharing+ and joint acquisitions performed quite well when applied on the full echo train.

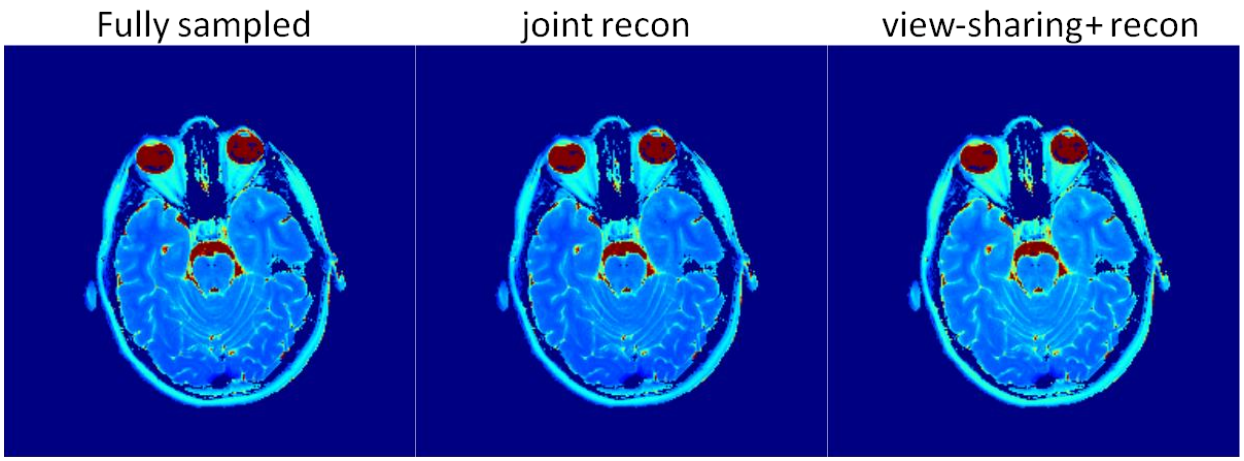

Figure 5.13, comparison of the T2 maps generated from fully sampled, joint acquisition, and the view-sharing+ schemes. The maps are essentially identical. Their differences are not visually observable.

The percentage difference error for the T2 maps were generated as follows:

$$\%E_{T2\_random-joint} = \frac{T2_{full} - T2_{random-joint}}{T2_{full}} \times 100 \quad (5\text{-}6)$$

$$\%E_{T2\_segmented-joint} = \frac{T2_{full} - T2_{segmented-joint}}{T2_{full}} \times 100 \quad (5\text{-}7)$$

The error maps along with their corresponding error distribution are shown in Figure 5.14. The error distribution has a quite narrow histogram with a 5-95 percentile of less than 5% absolute error in both cases. The joint acquisition scheme tends to have high errors only at the sharp edges of high signal transitions in the object (such as CSF and the eyes) while the dyamic view sharing scheme has high errors spread across the object in the T2 map.

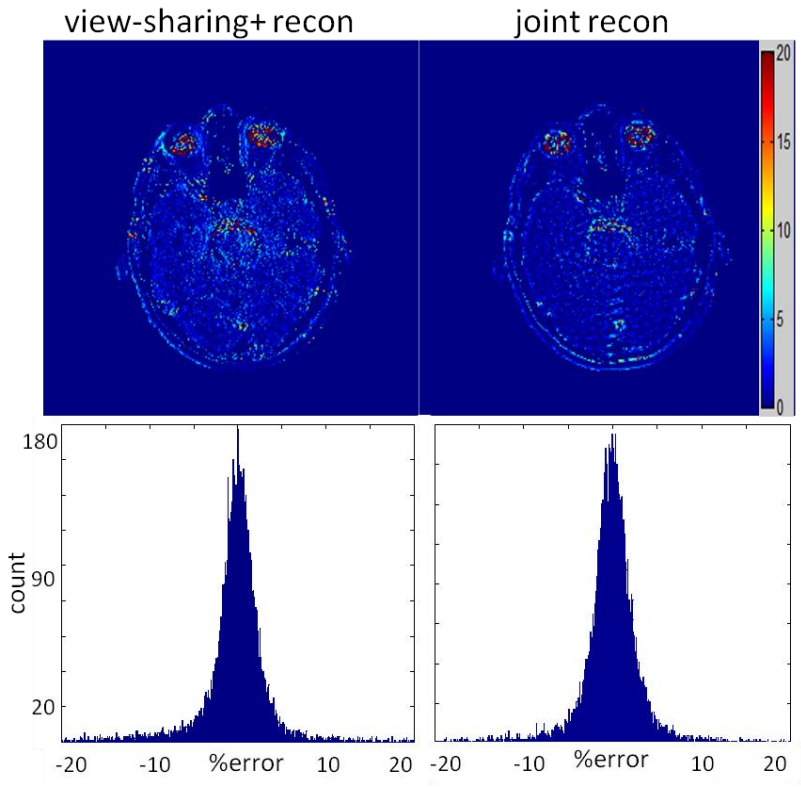

Figure 5.14, percentage error maps between T2 maps generated from the fully sampled images and view-sharing+ and joint acquisition schemes. The error distribution for each scheme is also shown. The joint acquisition and view-sharing+ both generally performed quite well with considerably low error distributions. The view-sharing+ reconstruction tends to have errors all over the image while the joint acquisition scheme has high error only at the sharp edges of the image.

5.4 Discussion

5.4.1 Performance

Both of the acquisition schemes (view-sharing+ and joint acquisition) performed quite well in reconstructing the full train of spin echoes with the only difference that the joint acquisition is faster and is applied in 3D. The reason as it was mentioned before is the short echo spacing between the neighboring echoes in the joint reconstruction. Therefore the contrast and/or signal difference between the shared k-space information is minimal and consequently

the k-space inconsistencies are marginal. Here we show three of the neighboring echoes along with their corresponding k-spaces to show why these methods performed well.

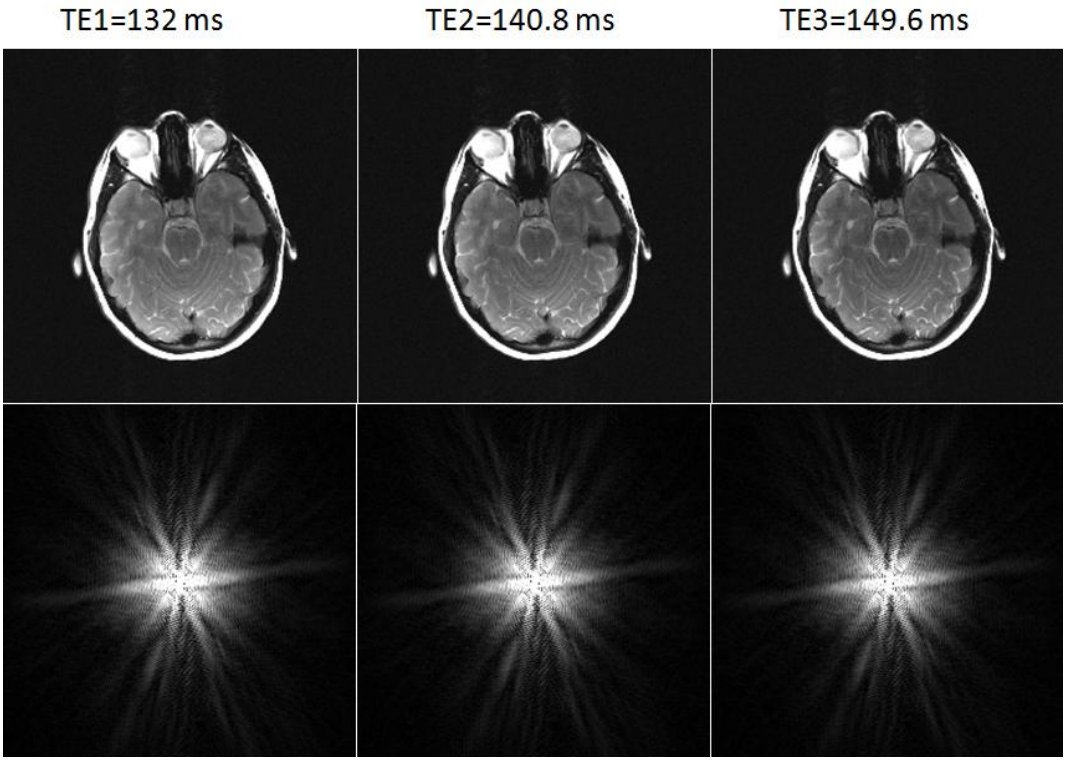

Figure 5.15, comparison of the magnitude and their corresponding k-space of three neighboring echoes in the multi-echo spin echo train with TE1=132 ms, TE2=140.8 ms and TE3=149.6ms (deltaTE=8.8 ms). The signal and contrast difference between these echoes are very marginal. Therefore joint reconstruction performs well.

5.4.2 Comparison with low resolution imaging

Reducing the number of encoding lines in any way will lead to a faster scan time. A simple solution would be to reduce the spatial resolution of the image by reducing the k-space matrix size or in other words truncating the k-space signal. Here we compare the T2 maps generated from the joint acquisition with the one created from its equivalent low-resolution approach. The scan time is kept the same between two methods by fixing the total number of encodings in both approaches the same.

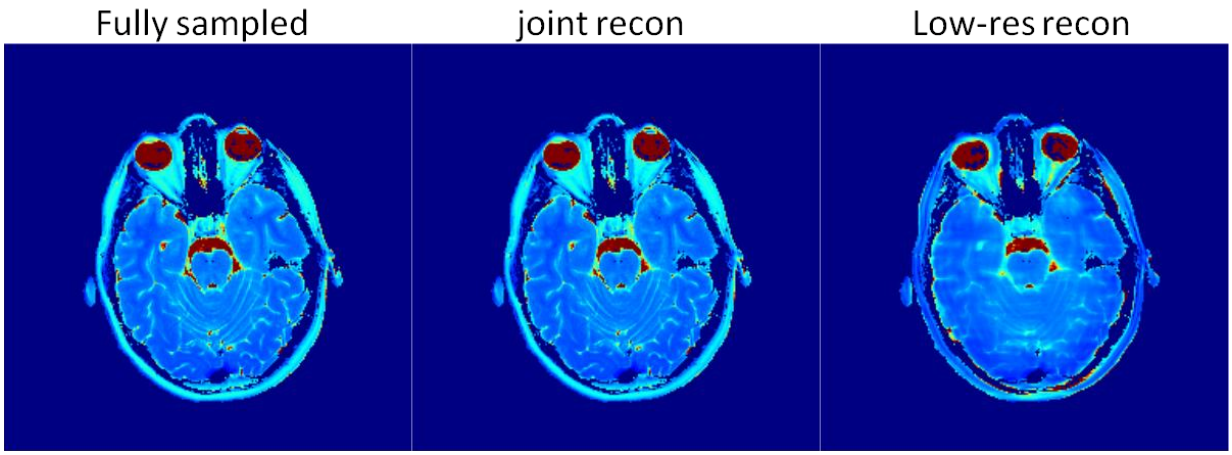

Figure 5.16, comparison of the T2 maps generated from fully sampled, joint acquisition, and the low resolution acquisition schemes. The maps from the low resolution scheme suffer from blurring and excessive Gibbs ringing artifacts.

The blurring and Gibbs ringing artifacts due to k-space truncation in the low-resolution acquisition scheme manifested themselves in the resulting T2 maps with an excessive partial volume effect which makes them practically unusable. The results from the low-resolution scheme could be improved using the k-space extrapolation algorithms [1, 2, 4, 5]. All these methods however need *a priori* information about the object of interest.

5.5 Conclusion

In this chapter, we showed here that a combination of keyhole imaging and view-sharing acquisition can be employed in collecting a multi-echo spin echo dynamic imaging with the purpose of pixel by pixel T2 mapping and with the goal of faster acquisition. We showed that there are advantages in randomly collecting the outer k-space information instead of employing the blocked approach. We also showed that the presence of discontinuities between the neighboring data points, the more severe the inconsistencies in the composite k-spaces and consequently the more artifacts in the reconstructed images.

The implementation of the joint acquisition in a given sequence is generally easy and straightforward. The joint acquisition scheme can be applied to other dynamic imaging experiments. This includes multi flip angle acquisition for T1 mapping, time-resolved contrast enhanced magnetic resonance imaging (CE-MRA) for resolving the contrast agent evolution in-vivo. However the applications are limited to imaging experiments where the complex phase is similar between different frames. This is due to induced inconsistencies in the complex k-space signal, which are not resolvable. Our simulations showed failure when we applied the joint acquisition scheme to multi-echo gradient echo imaging for T2* mapping because of major differences in the phase. We are still trying to find a solution for resolving this limitation.

SUMMARY AND FUTURE DIRECTIONS

The main theme of this thesis was focused on developing techniques for faster acquisition of MR Images. We started this project seeking ways to accelerate some of our high resolution imaging techniques such as MR angiography and MR venography using susceptibility weighted imaging. At the same time we could use the same technique for increasing imaging spatial resolution to capture even smaller vascular structures in a reasonable time and with sufficient SNR.

Compressed Sensing as a relatively new technique seemed very exciting to pursue our goals. Therefore I decided to review the current literature and try to develop the theory of CS sampling and reconstruction leading to its application in MRI. Our simulations showed advantages of CS reconstruction and the limitations associated with it which should be considered if implemented into a conventional MRI sequence.

Along the way the novel idea of “joint acquisition and reconstruction” came along where we combined our experience with CS random sampling and some dynamic imaging techniques for faster multi data point imaging such as multi echo imaging. We showed that the advantages provided by random undersampling schemes can improve the reconstructed images from any general view-sharing imaging acquisition. We also showed that certain precautions must be met when designing view-sharing acquisition schemes in order to make sure the reconstructed images will provide clinically reliable images.

I just started exploring the concepts of fast imaging and constrained reconstruction. Future directions of this project may be listed as follows:

- Improving the CS reconstruction using better regularization algorithms
- Implementing CS and joint acquisition sampling schemes to our current state of the art sequences where they fit
- Implementing the MATLAB CS and joint reconstruction scripts into a standalone programming environment (such as C++)
- Examining the joint acquisition technique for other dynamic imaging experiments
- Studying the possibilities of combining CS with some classical data extrapolation techniques
- Combining the CS reconstruction with the joint reconstruction to further reduce the number of samples and consequently the scan time

REFERENCES

1. E.M. Haacke, Z.-P.L., and S.H. Izen, *Constrained Reconstruction: A Superresolution Optimal Signal-to Noise Alternative to the Fourier Transform in Magnetic Resonance Imaging.* Medical Physics, 1989. **16**: p. 388-397.
2. Z.-P. Liang, E.M.H., and C.W. Thomas, *High Resolution Inversion of Finite Fourier Transform Data Through a Localized Polynomial Approximation.* Inverse Problems, 1989. **5**: p. 831-838.
3. Sundar Amartur, Z.-P.L., Fernando Boada, E. Mark Haacke, *Phase-constrained Data Extrapolation Method for Reduction of Truncation Artifacts.* JMRI, 1991. **1**: p. 721-724.
4. F. Boada, E.M.H., W. Tobocman, K. Santosh, and Z.P. Liang, *Superresolution Imaging Applied to Ultrasonic Scattering.* Inverse Problems, 1989. **5**: p. L21-L26.
5. E.M. Haacke, Z.-P.L., and S.H. Izen, *Superresolution Reconstruction through Object Modeling and Parameter Estimation.* IEEE-ASSP, 1989. **37**: p. 592-595.
6. Z.-P. Liang, F.E.B., R. Todd Constable, E. M. Haacke, P.C. Lauterbur, and M.R. Smith, *Constrained reconstruction methods in MR imaging.* Review of Magnetic Resonance in Medicine, 1992. **4**: p. 67-185.
7. E. Mark Haacke, R.W.B., Michael R. Thompson , Ramesh Venkatesan, *Magnetic Resonance Imaging: Physical Principles and Sequence Design*. 1999.
8. Bernstein, M.A., K.F. King, and X.J. Zhou, *Handbook of MRI pulse sequence*. 2004: Elsevier.
9. Lauterbur, P.C., *Image formation by induced local interactions. Examples employing magnetic resonance.* Nature, 1973. **243**(190).
10. P Mansfield, P.K.G., A N Garroway, D C Stalker *Multi-pulse line narrowing experiments*, in *First Specialised Colloque Ampere*1973: Poland.
11. Zhi-Pei Liang and P.C. Lauterbur, *Principles of magnetic resonance imaging: A signal processing perspective*. 2000, New York: IEEE.

12. R. M. Henkelman and M.J. Bronskill, *Artifacts in magnetic resonance imaging.* Rev. Mag. Reson. Med., 1987. **3**: p. 1-126.

13. P. Margosian, F.S., and D. E. Purdy, *Faster MR imaging: Imaging with half the data.* Health Care Instrumentat, 1986. **1**: p. 195-197.

14. Est, J.J.C.a.A.V., *Reducing MR imaging time by one-sided reconstruction*, in *Topical Conf. Fast MRI Techniques*1987: Cleveland, Ohio.

15. M. R. Smith, W.S., and S. T. Nichols, *1986*, in *5th Ann. Meet. Soc. Magn. Reson. Med.*High quality MR imaging with decreased acquisition time using autoregressive moving average modeling: Montreal, Quebec. p. 81-82.

16. M. R. Smith, S.T.N., R. M. Henkelman, and M. L. Wood, *Application of auto-regressive moving average parametric modeling in magnetic resonance image reconstruction.* IEEE Trans. Med. imaging, 1986. **MI-5**: p. 132-139.

17. Z.-P. Liang, E.M.H., and C. W. Thomas, *High resolution spectral estimation through a localized polynomial approximation.* Inverse Problems, 1989. **5**: p. 831-847.

18. Lauterbur, Z.-P.L.a.P.C., *A generalized series approach to MR spectroscopic imaging.* IEEE Trans. Med. Imaging, 1991. **MI-l0**: p. 132-137.

19. Pruessmann KP, W.M., Scheidegger MB, Boesiger P, *SENSE: sensitivity encoding for fast MRI.* Magn Reson Med, 1999. **42**: p. 952–962.

20. Griswold MA, J.P., Heidemann RM, et al, *Generalized autocalibrating partially parallel acquisitions (GRAPPA).* Magn Reson Med, 2002. **47**: p. 1202–1210.

21. Sodickson DK, M.W., *Simultaneous acquisition of spatial harmonics (SMASH): fast imaging with radiofrequency coil arrays.* Magn Reson Med, 1997. **38**: p. 591-603.

22. Candès, E.J. *Compressive sampling*. in *Proceedings of the International Congress of Mathematicians* 2006. Madrid, Spain.

23. E. Candès, J. Romberg, and T. Tao, *Robust uncertainty principles: Exact signal reconstruction from highly incomplete frequency information.* EEE Trans. Inform. Theory, 2006. **52**(2): p. 489–509.

24. E. Candès and T. Tao, *Near optimal signal recovery from random projections: Universal encoding strategies?* IEEE Trans. Inform. Theory,, 2006. **52**(12): p. 5406–5425.

25. Donoho, D.L., *Compressed sensing.* Technical Report, Stanford University, 2004.

26. *Lustig's assignment*.

27. *http://en.wikipedia.org/wiki/Regularization_(mathematics)*.

28. *http://en.wikipedia.org/wiki/Tikhonov_regularization*.

29. David L. Donoho and Y. Tsaig, *Fast Solution of l1 norm Minimization Problems When the Solution May be Sparse*, 2006.

30. M´ario A. T. Figueiredo, R.D.N., Stephen J. Wright, *Gradient Projection for Sparse Reconstruction: Application to Compressed Sensing and Other Inverse Problems.* IEEE JOURNAL OF SELECTED TOPICS IN SIGNAL PROCESSING, 2007. **1**(4): p. 586-597.

31. Tsaig, D.L.D.a.Y., *Fast Solution of l1-Norm Minimization Problems When the Solution May Be Sparse.* IEEE TRANSACTIONS ON INFORMATION THEORY, 2008. **54**(11): p. 4789-4812.

32. INGRID DAUBECHIES, MICHEL DEFRISE, and C.D. MOL, *An Iterative Thresholding Algorithm for Linear Inverse Problems with a Sparsity Constraint.* Communications on Pure and Applied Mathematics, 2004. **LVII**: p. 1413–1457.

33. Dmitry M. Malioutov, M.C.e., and Alan S. Willsky, *HOMOTOPY CONTINUATION FOR SPARSE SIGNAL REPRESENTATION.* ICASSP, 2005. **733**.

34. Michael Lustig, David Donoho, and J.M. Pauly, *Sparse MRI: The Application of Compressed Sensing for Rapid MR Imaging.* Magnetic Resonance in Medicine, 2007. **58**: p. 1182–1195.

35. Starck J, E.M., Donoho D., *Image decomposition via the combination of sparse representations and a variational approach.* IEEE Trans Image Process, 2005. **14**: p. 1570–1582.

36. Taubman DS, M., *JPEG 2000: Image compression fundamentals, standards and practice.* Kluwer International Series in Engineering and Computer Science, 2002.

37. Daubechies, I., *Orthonormal Bases of Compactly Supported Wavelets.* Communications on Pure and Applied Mathematics, 1988. **41**(7): p. 909-996.

38. Brani Vidakovic and P. Mueller, *WAVELETS FOR KIDS: A Tutorial Introduction*, 1991, Duke University.

39. Lee A. Barford, R.S.F., David R. Smith, *An Introduction to Wavelets*, 1992, Hewlet Packard.

40. Mallat, S., Hwang, W. L., *Singularity Detection and Processing with Wavelets.* IEEE Transactions on Injormation Theory, 1992. **38**(2): p. 617643.

41. http://statweb.stanford.edu/~wavelab/Wavelab_850/index_wavelab850.html.

42. Jeffrey D. Blanchard, J.T., *GPU accelerated greedy algorithms for compressed sensing.* Mathematical Programming Computation, 2013. **5**(3): p. 267-304.

43. Thomas E. Yankeelov and J.C. Gore, *Dynamic Contrast Enhanced Magnetic Resonance Imaging in Oncology: Theory, Data Acquisition, Analysis, and Examples.* Curr Med Imaging, 2009. **3**(2): p. 91–107.

44. Jing Yuan, S.K.K.C., David Ka Wai Yeung, Anil T Ahuja, Ann D King, *Quantitative evaluation of dual-flip-angle T1 mapping on DCE-MRI kinetic parameter estimation in head and neck.* Quant Imaging Med Surg, 2012. **2**(4): p. 245–253.

45. Julia V. Velikina, A.L.A., Alexey Samsonov, *Accelerating MR Parameter Mapping Using Sparsity-Promoting Regularization in Parametric Dimension.* Magnetic Resonance in Medicine, 2013. **70**: p. 1263–1273.

46. Mariya Doneva, P.B., Holger Eggers, Christian Stehning, Julien Sénégas , Alfred Mertins, *Compressed Sensing Reconstruction for Magnetic Resonance Parameter Mapping.* Magnetic Resonance in Medicine, 2010. **64**: p. 1114-1120.

47. Frank R. Korosec, R.F., Thomas M. Grist, Charles A. Mistretta, *Time-Resolved Contrast-Enhanced 3D MR Angiography.* MRM, 1996. **36**: p. 345-351.

48. J. Du, T.J.C., H.J. Wagner, K. Vigen, S.B. Fain, W.F. Block, F.R. Korosec,T.M. Grist, C.A. Mistretta, *Time-Resolved, Undersampled Projection Reconstruction Imaging for High-Resolution CE-MRA of the Distal Runoff Vessels.* Magnetic Resonance in Medicine, 2002. **48**: p. 516-522.

49. Dariusch R. Hadizadeh, J.G., Gabriele Beck, Liesbeth Geerts, Guido M. Kukuk, and H.U. Azize Boström, Hans H. Schild, Winfried A. Willinek, *View-sharing in keyhole imaging: Partially compressed central k-space acquisition in time-resolved MRA at 3.0 T.* European Journal of Radiology, 2011. **80**: p. 400-406.

50. Wu, J.L.D.J.S.L.D.H., *Application of Keyhole Imaging to Interventional MRI: A Simulation Study to Predict Sequence Requirements.* ISMRM, 1996. **6**: p. 918-924.

51. Winfried A. Willinek, M., et al., *Randomly Segmented Central k-Space Ordering in High-Spatial-Resolution Contrast-enhanced MR Angiography of the Supraaortic Arteries: Initial Experience.* Radiology, 2002. **225**: p. 583–588.

52. Joop J. van Vaals, e.a., *'"Keyhole" Method for Accelerating Imaging of Contrast Agent Uptake.* JMRI, 1993. **3**: p. 671-675.

53. Claudia Oesterle, P., Ralf Strohschein, Michael Ko¨ hler, MD, Markus Schnell, MD, Ju¨rgen Hennig, PhD, *Benefits and Pitfalls of Keyhole Imaging, Especially in First-Pass Perfusion Studies.* JOURNAL OF MAGNETIC RESONANCE IMAGING, 2000. **11**: p. 312-323.

54. Winfried A. Willinek, M., Dariusch R. Hadizadeh, MD, Marcus von Falkenhausen, MD, Horst Urbach, MD, R. Hoogeveen, MD, PhD, Hans H. Schild, MD, Ju¨rgen Gieseke, PhD1, *4D Time-*

Resolved MR Angiography With Keyhole (4D-TRAK): More Than 60 Times Accelerated MRA Using a Combination of CENTRA, Keyhole, and SENSE at 3.0T. JOURNAL OF MAGNETIC RESONANCE IMAGING, 2008. **27**: p. 1455-1460.

55. M. Saranathan, D.R., A. S. Brau, B. A. Hargreaves, S. Vasanawala. *Ultra high spatio-temporal resolution liver imaging using a new view ordering scheme and a 2-point Dixon acquisition*. in *ISMRM*. 2011.

56. Van Vaals J, B.M., Dixon W, et al., *Keyhole method for accelerating imaging of contrast agent uptake.* J Magn Reson Imaging, 1993. **3**: p. 671–675.

57. Jones R, H.O., Muller T, Rinck P, Oksendahl A., *K-space substitution: a novel dynamic imaging technique.* Magn Reson Med, 1993. **29**: p. 830–834.

58. Sundar Amartur, E.M.H., *Modified Iterative Model Based on Data Extrapolation Method to Reduce Gibbs Ringing.* JMRI, 1991. **1**: p. 307-317.

ABSTRACT

COMPRESSED SENSING AND JOINT ACQUISITION TECHNIQUES IN MRI

By

ROUHOLLAH (EHSAN) HAMTAEI

December 2013

Advisor: Prof. E. Mark Haacke

Major: Biomedical Engineering

Degree: Master of Science

The relatively long scan times in Magnetic Resonance Imaging (MRI) limits some clinical applications and the ability to collect more information in a reasonable period of time. Practically, 3D imaging requires longer acquisitions which can lead to a reduction in image quality due to motion artifacts, patient discomfort, increased costs to the healthcare system and loss of profit to the imaging center. The emphasis in reducing scan time has been to a large degree through using limited k-space data acquisition and special reconstruction techniques. Among these approaches are data extrapolation methods such as "*constrained reconstruction"* techniques, data interpolation methods such as *parallel imaging*, and more recently another technique known as "Compressed Sensing" (CS). In order to recover the image components from far fewer measurements, CS exploits the compressible nature of MR images by imposing randomness in k-space undersampling schemes. In this work, we explore some intuitive examples of CS reconstruction leading to a primitive algorithm for CS MR imaging. Then, we

demonstrate the application of this algorithm to MR angiography (MRA) with the goal of reducing the scan time. Our results showed reconstructions with comparable results to the fully sampled MRA images, providing up to three times faster image acquisition via CS. The CS performance in recovery of the vessels in MRA, showed slightly shrinkage of both the width of and amplitude of the vessels in 20% undersampling scheme. The spatial location of the vessels however remained intact during CS reconstruction.

Another direction we pursue is the introduction of "*joint acquisition*" for accelerated multi data point MR imaging such as multi echo or dynamic imaging. *Keyhole imaging* and *view sharing* are two techniques for accelerating dynamic acquisitions, where some k-space data is shared between neighboring acquisitions. In this work, we combine the concept of CS random sampling with keyhole imaging and view sharing techniques, in order to improve the performance of each method by itself and reduce the scan time. Finally, we demonstrate the application of this new method in multi-echo spin echo (MSE) T2 mapping and compare the results with conventional methods. Our proposed technique can potentially provide up to 2.7 times faster image acquisition. The percentage difference error maps created from T2 maps generated from images with joint acquisition and fully sampled images, have a histogram with a 5-95 percentile of less than 5% error. This technique can potentially be applied to other dynamic imaging acquisitions such as multi flip angle T1 mapping or time resolved contrast enhanced MRA.